Electronic Theses and Dissertations, 2004-2019

2008

Meshless Hemodynamics Modeling And Evolutionary Shape Optimization Of Bypass Grafts Anastomoses

Zaher El Zahab
University of Central Florida

University of
Central Florida

STARS
Showcase of Text, Archives, Research & Scholarship

MESHLESS HEMODYNAMICS MODELING AND EVOLUTIONARY SHAPE
OPTIMIZATION OF BYPASS GRAFTS ANASTOMOSES

by

ZAHER EL ZAHAB
B.S. University of Balamand, Lebanon, 2001
M.S. University of Central Florida, USA, 2003

A dissertation submitted in partial fulfillment of the requirements
for the degree of Doctor of Philosophy
in the Department of Mechanical, Materials and Aerospace Engineering
in the College of Engineering and Computer Science
at the University of Central Florida
Orlando, Florida

Spring Term
2008

Major Professor: Alain J Kassab

ABSTRACT

Objectives: The main objective of the current dissertation is to establish a formal shape optimization procedure for a given bypass grafts end-to-side distal anastomosis (ETSDA). The motivation behind this dissertation is that most of the previous ETSDA shape optimization research activities cited in the literature relied on direct optimization approaches that do not guaranty accurate optimization results. Three different ETSDA models are considered herein: The conventional, the Miller cuff, and the hood models.

Materials and Methods: The ETSDA shape optimization is driven by three computational objects: a localized collocation meshless method (LCMM) solver, an automated geometry pre-processor, and a genetic-algorithm-based optimizer. The usage of the LCMM solver is very convenient to set an autonomous optimization mechanism for the ETSDA models. The task of the automated pre-processor is to randomly distribute solution points in the ETSDA geometries. The task of the optimized is the adjust the ETSDA geometries based on mitigation of the abnormal hemodynamics parameters.

Results: The results reported in this dissertation entail the stabilization and validation of the LCMM solver in addition to the shape optimization of the considered ETSDA models. The LCMM stabilization results consists validating a custom-designed upwinding scheme on different one-dimensional and two-dimensional test cases. The LCMM validation is done for incompressible steady and unsteady flow applications in the ETSDA models. The ETSDA shape optimization include single-objective optimization results in steady flow situations and bi-objective optimization results in pulsatile flow situations.

Conclusions: The LCMM solver provides verifiably accurate resolution of hemodynamics and is demonstrated to be third order accurate in a comparison to a benchmark analytical solution of the Navier-Stokes. The genetic-algorithm-based shape optimization approach proved to be very effective for the conventional and Miller cuff ETSDA models. The shape optimization results for those two models definitely suggest that the graft caliber should be maximized whereas the anastomotic angle and the cuff height (in the Miller cuff model) should be chosen following a compromise between the wall shear stress spatial and temporal gradients. The shape optimization of the hood ETSDA model did not prove to be advantageous, however it could be meaningful with the inclusion of the suture line cut length as an optimization parameter.

To my beloved parents, Mahmoud and Dunia,

and to my precious wife Lori-Anne...

ACKNOWLEDGMENTS

It is a very special moment when I look back through the last six and a half years that I have spent as a graduate student at the University of Central Florida and remember each individual whom I was blessed to be with. Despite all the emotional stress that comes along with pursuing a graduate school career, I should admit that this educational experience has definitely made me a better person and changed a lot in the way I look at life.

First and foremost I dedicate my gratitude to my parents, Mahmoud and Dunia, who have helped me every step of the way; I could have not achieved my education without their generous support as I first landed in the United States. I have been really blessed with parents who never turned me down when I needed something and I am indebted to them for life. Just as equal, I want to highly recognize my beautiful and affectionate wife Lori-Anne who chose to share with me the emotional burden of being a Ph.D. student. I have been fortunate to have her as a great companion to do fun things with and as a stress relief during the hard times of research. I owe her all the missed weekends and holidays for the rest of our life.

I would like to acknowledge Dr. Alain Kassab and Dr. Eduardo Divo who granted me the opportunity of pursuing my Ph.D. degree in the Computational Mechanics Laboratory. It is under their guidance where I learned not to fear or surrender to any technical problem no matter how hard it is. I have earned a high confidence to face problems and solve them eventhough they might be time-consuming. I am looking forward to employ this confidence as I apply myself in my professional career. Special thanks go out to Dr. Gerald Smith and Dr. Mark Friedell for giving me the medical exposure relevant to my dissertation topic. The service of Dr. Olusegun Ilegbusi and Dr. David Nicholson on my committee is greatly appreciated. I want to also recognize Dr. Eric Petersen for his supervision over my Master's program. I also would like to mention few individuals such as Kevin Erhart, Sal Gerace, Eric Mitteff, Steven Dick, Jennifer Crain, and Patrick Mach for their positive input on my research activities.

TABLE OF CONTENTS

LIST OF FIGURES

Figure 5.27: Floor time-average TWSSG resulting from the hemodynamics in the optimal shapes of the conventional, Miller cuff, and hood ETSDA models.

LIST OF TABLES

LIST OF NOMENCLATURE

ϕ: Arbitrary field variable

α_j: Expansion coefficients

χ_j: Expansion functions

nep: Exponent parameter

sp: Shape parameter

r_j: Euclidean distance

P_j: Polynomial

β_j: Polynomial coefficients

ψ: Limiter function

Co: Courant number

a: Wave speed

m: Meter

sec: Second

$\vec{V}$: Velocity vector

(u, v, w): Velocity vector components

$\delta\vec{V}$: Velocity correction

ρ: Density

μ: Dynamics viscosity

p: Pressure

$\overset{\Rightarrow}{\tau}$: Viscous stress tensor

$(\boldsymbol{x}, \boldsymbol{y}, \boldsymbol{z})$: Spatial coordinates

$\vec{n}$: Outward drawn normal vector

t: Time

V_n: Normal velocity

ξ: Helmholtz potential

Re: Reynolds number

spc: Average point spacing

WSS: Wall shear stress

$\vec{tr}$: Traction vector

$\dot{\gamma}$: Shear rate

μ_∞: The infinite shear viscosity

μ_0: The zero shear viscosity

λ: The time constant

npl: The power law index

GEN: Generation

F: Individual fitness

prb: Probability

f: Objective function

w: Weighting coefficients

$NIDV$: Individuals number in a population

$Rank$: Individual rank

$SWSSG$: Spatial wall shear stress gradient

$TWSSG$: Temporal wall shear stress gradient

T_{pulse}: Blood pulsatile cycle

$\vec{t_g}$: Tangential unit vector

N_{BF}: Number of boundary points on the floor optimization section

β: Anastomotic angle

D_{graft}: Graft caliber

H_{cuff}: Miller cuff height

$\mathcal{L}$: Linear differential operator

∂: Partial derivative operator

∇: Gradient

$\nabla \cdot$: Divergence

∇^2: Laplacian

CHAPTER 1: INTRODUCTION

1.1 State of the Art Problem

Peripheral vascular disease (PVD) is a common circulatory problem that accounts for about 8-12 million individuals in the United States [1]. PVD mainly pertains to the hardening, stenosis and blockage of arteries located outside of the heart. Recently, endovascular procedures such as stenting and balloon angioplasty have been extensively implemented to circumvent the PVD problems. Nonetheless, when the PVD is extending over a long section of the artery endovascular procedures become inadequate and bypass procedures are consequently indispensable to avoid further complications. The bypass surgery serves to detour blood flow around the diseased artery section and ensure perfusion to the ischemic areas. Lower limbs are frequent sites for PVD occurrence and severe complications could lead to their amputation. Figure (1.1) shows a peripheral bypass procedure in which a bypass graft connects the femoral and popliteal artery.
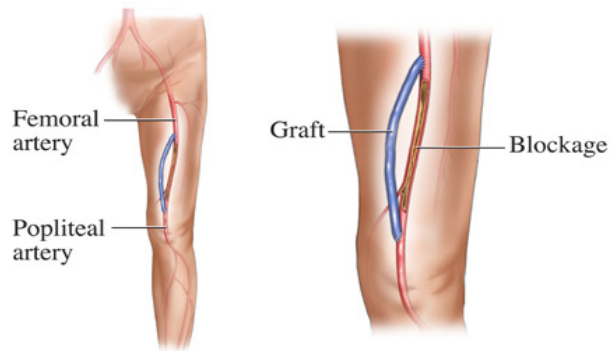
Figure 1.1: A peripheral bypass grafting between the femoral and the popliteal arteries (known as the femoropopliteal bypass grafting).

At the lower limbs sites, bypass surgeries are preferably carried out by vein grafting, which proved to exhibit excellent patency rates and limb salvage rates [2]. Patency is a medical

term referring to the state of being open, expanded, or unblocked. If vein grafting is unavailable or unsuitable, a synthetic graft is then utilized. Synthetic grafts are typically manufactured of Dacron material or polytetrafluoroethylene (PTFE) materials. Unfortunately, synthetic grafts are known to exhibit unsatisfactory long-term performances [3,4], due to a variety of reasons to be discussed below.

Intimal Hyperplasia (IH) has been identified to be a major cause of post-operative graft failure. Hyperplasia is a medical term referring to the abnormal proliferation of cells within a tissue or an organ, while, Intimal Hyperplasia is the thickening of the tunica intima, the inner-most layer of the various tissues composing the arterial wall, as a complication of a surgical intervention. Several biological and physical factors are thought to lead to the development of IH, such as surgical injury [5], graft-artery compliance mismatch [6,7], and abnormal hemodynamics patterns [8] that causes interaction of the blood particles with the arterial wall [9,10]. IH is often found at the end-to-side distal anastomosis (ETSDA) of the graft [11] and it occurs particularly at the graft heel and toe, plus on the floor of the host artery [6,12] as demonstrated in Figure (1.2).
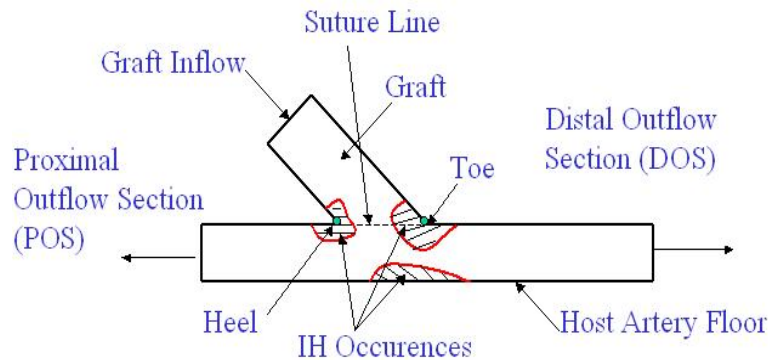
Figure 1.2: The IH localization sites at the ETSDA.

Among the hemodynamics parameters thought to have a contribution to the development of IH are high wall shear stress (WSS) [13,14], the combination of low WSS and high oscillatory

2

shear index (OSI) [15], and the combination of the high spatial wall shear stress gradients (SWSSG) and the high temporal wall shear stress gradients (TWSSG) [16]. Several attempts to optimize the shape of the ETSDA with the aim to reduce abnormal hemodynamics parameters are reported in [17,18,19]. Notably, very few of the ETSDA shape optimization attempts based on lowering the abnormal hemodynamics incorporated a formal optimization approach [20,21]; In most cases, the ESTDA shape optimizations relied on direct or trial-and-error approaches that do not necessarily yield an optimal shape. Genetic algorithms (GAs) are known to identify a global optimum within a prescribed design space. Therefore, an optimization research entailing the genetic algorithms would make a significant contribution to the on-going endeavors of optimizing the ETSDA shape.

1.2 Statement of Purpose

The principal goal of this dissertation is to find an optimal design of the ETSDA with the objective of minimizing if not eliminating the abnormal hemodynamics parameters associated with IH development. The formal optimization will be executed by coupling three computational objects: a flexible computational fluid dynamics (CFD) solver that readily accommodates changing geometry, an automated CFD pre-processor, and a shape optimization genetic algorithm (SOGA). As the geometry varies continuously in the shape optimization process, it is necessary to utilize a CFD solver that does not require the tedious and manual task of mesh generation for each candidate geometry, a process that would render automated shape optimization impossible. As such, the Localized Collocation Meshless Method (LCMM) [23,24,25] is utilized as the CFD method of choice due to the fact that this technique solves the governing equations of fluid mechanics on a non-ordered set of points that are readily arranged in complex geometries such as the bypass graft geometries of concern in this dissertation and subsequently re-arranged for evolving geometries generated by the SOGA. The outcome of the

current research project will be an establishment of a formal optimization methodology for peripheral bypass procedures whose aim is to improve the grafts post-surgical performances by reducing abnormal hemodynamics associated with IH. Results of this study will provide guidance in possible means to increase graft patency rates and consequently potentially reduce the level of patients limb amputation and morbidity. Moreover, the methodology demonstrated herein can be applied to various other vascular-related problems, for instance the modeling of hemodynamics in vicinity of implanted stents and their effects in subsequent arterial restenosis.

1.3 The Dissertation Organization

The developments and results of the tasks undertaken in this dissertation are reported in six chapters. Following the introductory first chapter, the second chapter presents a comprehensive literature review of bypass grafting long term performance, background of IH and its growth at the ETSDA, relevance of hemodynamics to the IH growth and design attempts to mitigate the abnormal hemodynamics in the ETSDA. The third chapter provides a review on the localized meshless methods applications in fluid dynamics, a detailed discussion of the LCMM numerical aspect and formulation, and the composition of a meshless-based upwinding/limiter technique to control numerical oscillations. The fourth chapter entails the specific application of the LCMM to laminar incompressible flow problems with analytical and numerical validations. Numerical validations involve several cases of the blood flow in the ETSDA under steady/pulsatile conditions. Chapter four also discusses the blood non-Newtonian rheology and provides a further validation example for the pulsatile blood flow with a non-Newtonian viscosity. In chapter five, there is a wide review of the genetic algorithms and their applicability to single- and multi-objective shape optimization scenarios; then an explanation of the build-up of the information passage loop (IPL) to optimize the ETSDA shape is provided. The two-dimensional shape optimization results of the conventional, Miller cuff, and hood

ETSDA models are presented and discussed. Finally, the procedures and findings of the dissertation are summarized in chapter six.

CHAPTER 2: LITERATURE REVIEW

This chapter provides a general review of publications related to bypass-graft-based IH considering four different perspectives: (1) a review of the issues related to the post-surgical performances of both autologous and synthetic peripheral grafts in terms of patency rates and limb salvages, as the patency rate indicates the level of post-operative openness of the vascular conduit, (2) a review of IH background and its occurrence at the grafts ETSDA site, (3) review of the hemodynamics factors believed to contribute to the growth of IH, and (4) review of previous attempts to improve the ETSDA shape.

2.1 Bypass Grafts Post-Surgical Performances

Taylor LM et al. [2] report on a survey of 564 limbs in 434 patients who were treated for infrainguinal arterial ischemia and 564 limbs in 387 of the patients underwent reverse vein bypass grafting. The primary and secondary post-operative patency rates for all the grafts at 5 years were 75% and 81 % respectively. Primary patency is defined as uninterrupted patency of the original graft without the need for intervention of any kind. Secondary patency is patency of the original graft as maintained by intervening measures such as angioplasty or patch grafting. The results of this vein grafting method for the lower extremities revascularization reflect excellent patencies when compared to synthetic grafting patencies in the long term.

Veith et al. [3] compared the autologous saphenous vein (ASV) grafts and PTFE synthetic grafts performances in 845 infrainguinal bypass operations. They found similar post-operative patency rates between the ASV and the PTFE grafts at 2 years (81% ± 4% for ASV versus 76% ± 4% for PTFE), whereas a significant difference was noted at 4 years (68% ± 8% ASV versus 47% ± 9% for PTFE). However, the post-operative limb salvage rate results did not substantially differ for the two types of grafting at 4 years (57% ± 10% for ASV and 61% ± 10% for PTFE).

Their results failed to support the use of PTFE grafting for femoropopliteal, especially for the popliteal sections below the knee. Even so, they noted that when ASV grafting is unfeasible, PTFE grafting becomes a better option than a major limb amputation.

Rafferty et al. [4] also carried out a comparison between the ASV and PTFE bypass grafting in the lower extremeties of 932 patients. They noticed that although both materials present similar success above the knee, the 3-year patency rate results of ASV bypasses to the popliteal sections below the knee (69 to 80 %) were superior to the results of the PTFE grafts (32% to 50%). Furthermore, they reported that PTFE grafts required re-operations at three times the rate of vein grafts to maintain limb salvage.

As an effort to enhance the performance of the PTFE grafts expanded PTFE (e-PTFE) grafts were innovated. The expansion is done by applying a vein cuff or patch to slightly modify the nature of the bypass graft ETSDA. The addition of those vein sections is thought to diminish the compliance mismatch between the PTFE graft material and the biological material of the host artery. Taylor RS et al. [22] incorporated a vein patch in a series of 256 bypass graft ETSD anastomoses and the post-operative patencies at 5 years were 71% for the popliteal sections and 54 % for the infrapopliteal sections. Raptis et al. [26] examined the performance of 559 PTFE grafts when a vein cuff is inserted at their ETSD anastomoses. The post-operative patency rates were found to be 62% at 3 years for the below-knee popliteal sections; In addition, the post-operative limb-salvage at 3 years 89% for threatened limbs. When scrutinized with the conventional PTFE grafts patency results provided by Veith and Rafferty, the so-called "Taylor patch" (Figure (2.1a)) and "Miller cuff" (Figure (2.1b)) ETSDA PTFE grafts patency results exhibit important improvements. It is clear from the above references that vein grafting is always the best option for peripheral bypass surgeries, nonetheless the PTFE grafting imposes itself as an option when the vein grafting is not possible. An important feature about the PTFE synthetic grafting, whether it is conventional or expanded, lies in the ETSDA multiple design degrees of

freedom. Since PTFE grafts are manufactured, those design variables can be set to yield an optimal post-operative performance of the graft.

(a)   (b)
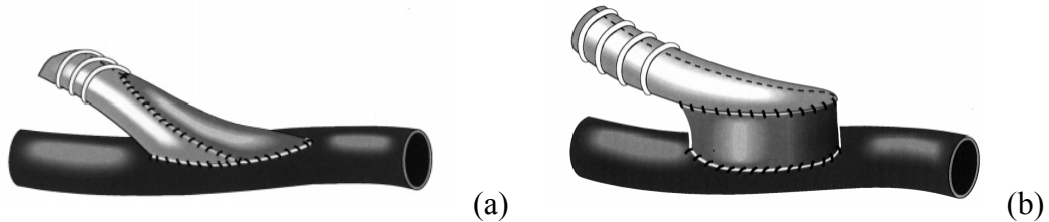
Figure 2.1: The Taylor Patch (a) and the Miller Cuff (b) ETSDAs [49].

2.2 Background of the ETSDA IH

IH is recognized as an important restenosis (recurrence of an abnormal narrowing in a blood vessel) mechanism that occurs in the wake of a bypass surgery [27]. Logerfo et al. [11] indicated that IH particularly tends to localize at the ETSDA of a bypass graft and eventually leads to the graft failure. Sottiurai et al. [12] examined the IH localization at the ETSDA of 42 canine PTFE iliofemoral grafts. Their study demonstrated that IH manifests itself exclusively at the heel and the toe of the graft and at the floor of the host artery as revealed in Figure (2.2). Similar findings of the IH anastomotic growth sites were reported by Bassiouny et al. [6].
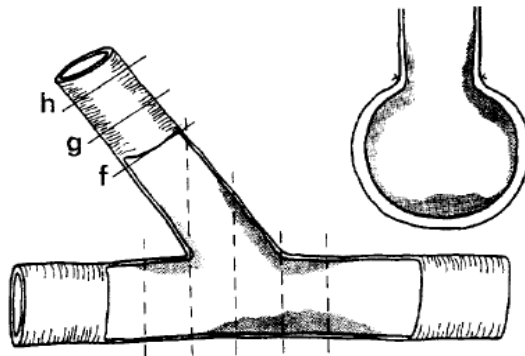
Figure 2.2: Sagital and cross-sectional drawings of an ETSD anastomosis depicting the occurrence of IH at the heel and toe of graft and floor of the host artery [12].

Lemson et al. [27] reviewed the three wave model that depicts the development of IH in the arterial wall as shown in Figure (2.3). The first wave consists of the smooth muscle cells (SMCs) proliferation in the tunica media due to under-production of inhibiting factors caused by the endothelium damage. The endothelium damage is also accompanied by a degradation of the extarcellular matrix (ECM) that embeds the SMCs and prevents their migration. The second wave marks the SMCs migration from the tunica media to the tunica intima. The third wave of intimal expansion probably occurs as a result of SMCs accumulation through proliferation, continued migration or both. This accumulation of SMCs leads to the deposition of ECM in the intimal area. The volume percentage of SMCs in the intimal area is about 20% and that of the ECM ranges between 60% and 80%.
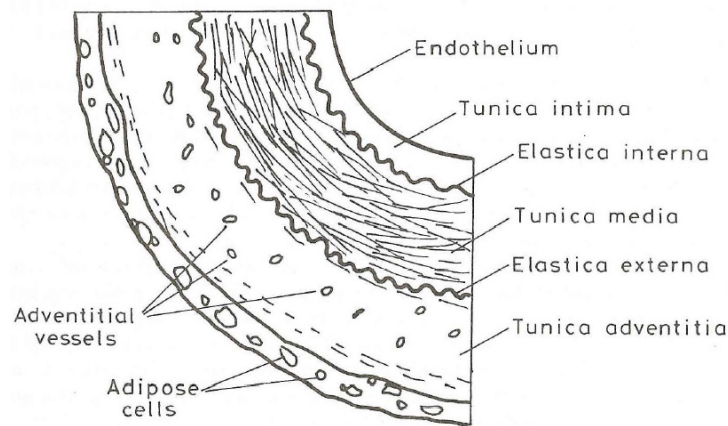
Figure 2.3: The various layers composing the arterial wall.

The literature contains a variety of mechanisms reported to lead to intimal hyperplastic growth. Those mechanisms are: (1) surgical injury, (2) the graft-artery compliance mismatch, and (3) the abnormal hemodynamics patterns.

As for the arterial injury due to the surgical procedure, Kraiss [5] laid out the three-degree injury model leading to the pathogenesis of IH; The first type is an non-denuding

endothelial injury where there is some morphological changes on the endothelium and the platelet adherence is minimal. The second injury type involves a denudation of the endothelium, but the elastica interna remains intact and the tunica media incurs a little if any damages. The third injury type is a transmural injury that results in medial or even advential damages.

Regarding the compliance mismatch between the graft and the host artery, Bassiouny et al. [6] investigated the localization of anastomotic IH following an 8-week implantation of saphenous vein and PTFE bypass grafts in 13 mongrel dogs. They detected a greater occurrence of the suture line IH on the PTFE anastomoses than on the vein anastomoses. They also found that the IH levels on the host artery floor were the same for both graft types. Trubel et al. [7] investigated 32 PTFE femoropopliteal bypass graft models (Conventional model, Linton patch, Taylor Patch, and Miller Cuff) that had been implanted in 16 sheep for 6 months. They observed that IH occurrence is the greatest along the transition between the PTFE grafts and the host artery, then between the PTFE grafts and the venous patches, and the lowest IH levels were found on the artery floor. Synthesizing the observations made in [6] and [7] with the grafts long-term performances discussed earlier [2-4,22,26] strongly suggest that the compliance mismatch between the graft and the native artery has a principal role in the IH amplification as far as the suture line is concerned.

With respect to the abnormal hemodynamics patterns, those patterns arise from the unphysiological configuration of the bypass graft ETSDA, Kleinstreuer et al. [8] presented a comprehensive review of IH hemodynamics biogenesis. They discussed various abnormal hemodynamics patterns such as recirculation zones, flow separation and re-attachment, significant secondary velocities, stagnation point regions, etc. They identified the wall parameters that reflect the abnormal hemodynamics patterns, such as the wall shear stress (WSS), the WSS spatial and temporal gradients, the normal pressure gradient and the wall particle density. Unphysiological values of the hemodynamics wall parameters lead to a sequence of biological events such as endothelial dysfunction, injury of the endothelium,

enhanced wall permeability, aggregation/deposition of platelets, and SMCs proliferation. Figure (2.4) illustrates the hemodynamics factors suggested to promote anastomotic IH. Kleinstreur's review revealed that the IH levels have been associated with high WSS, low WSS, high spatial wall shear stress gradient (SWSSG), high temporal wall shear stress gradient (TWSSG), and high oscillatory shear index (OSI). Most importantly, the review of Kleinstreuer did not present a unified theory confirming any of the hemodynamics parameters as being an exclusive cause of IH development. More experimental data are yet needed before strong correlations can be established between IH and specific hemodynamics parameters. As the current literature review will show in the following section, there are several school of thoughts on which hemodynamics parameter(s) are the main or exclusive contributor(s) to the IH growth.
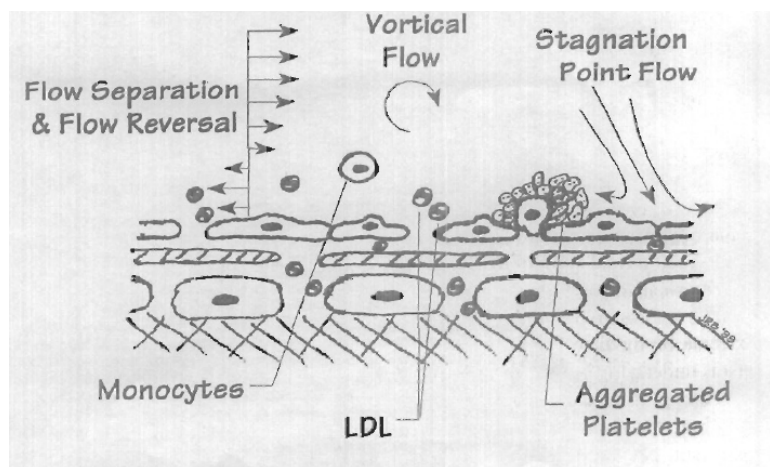
Figure 2.4: Representation of the abnormal hemodynamics in the anastomosis vicinity [8].

2.3 Hemodynamics Relevance to the IH Growth

An initial observation of the hemodynamics role in the growth of IH can be corresponded to the work of Fry et al. [13]. They quantified the acute changes in endothelial histology that are associated with an induced increase in blood velocity. Their results proved that high levels of the

WSS induce a deterioration of the endothelial surface consisting of swelling, cell deformation, cell disintegration, and finally dissolution and erosion of cell substance. Imaparto et al. [14] presented similar findings regarding the high WSS engagement in insulting the endothelium and hence originating the IH phenomena. Nevertheless, the work of Fry [13] and Imparato [14] apparently did not account for the arterial wall distensibility effects on the regulation of the WSS. Zarins et al. [28] performed an experiment on monkeys and demonstrated that when blood flow increases ten times, the arterial wall distensibility will restore the mean WSS to a physiological value of 1.5 dyne/cm^2. Furthermore, Kohler et al. [29] implanted PTFE bypass grafts in baboons and found that the increase of blood flow, hence the increase in the WSS inhibits IH. Since IH still occur under *in vivo* conditions where high WSS values are not highly expected due to the wall distensibility or simply because the high WSS might be an IH inhibitor, researchers started examining the relationship between IH growth and other hemodynamics parameters. The hemodynamics parameters that have been subsequently reported in the literature to correlate with IH are the low and oscillatory WSS as well as the mean spatial and temporal WSS gradients.

Ku et al. [30] measured the fluid velocities by laser doppler velocimetry under pulsatile flow conditions in a scale model of the human carotid bifurcations harvested from cadavers. They found that the intimal thickening is minimal at areas where the WSS was measured to be the highest. On the other hand, they measured low and oscillatory WSS values at area where the intimal plaque builds up the most. Following their bypass grafts canine implant experiment [6], Bassiouny et al. explanted those grafts and used them to produce *in-vitro* ETSDA casts where pulsatile flow visualization studies were performed. They noted a development of complex secondary flow patterns in the vicinity of the suture line, which they suggested may have an influence on the suture line thickening. On the host artery floor, they observed that the location of the stagnation oscillated in direction and shear throughout the pulsatile cycle, moving distally during the acceleration phase and proximally during the deceleration phase. They concluded that

the intimal thickening takes place on the host artery floor due to the flow reattachement at that site and due to the low and oscillating WSS. The theory presented in [6] was later supported by the results of animal [15] and flow visualization studies [31] on the ETSDA IH development.

In an effort to correlate hemodynamics parameters to IH levels, Keynton et al. [15] implanted PTFE synthetic grafts as carotid artery bypasses in 6 adult mongrel dogs for 12 weeks with ETSDA graft-to-artery diameter ratios of 1.0 and 1.5. Following the implantation, they used a specially designed 20 MHz triple crystal ultrasonic wall shear rate (WSR) transducer to measure the wall shear rate (WSR) and extract its spatial and temporal gradients in addition to extracting the OSI in the same implanted anastomotic models. After explanting the grafts, the IH levels were measured and corresponded to the spatial distribution of the mean WSR, absolute mean WSR and the OSI downstream of the graft toe and at the floor of the host artery. No strong correlations was found between the IH levels with the mean and peak WSR values, unlike with the OSI that presented a relatively strong correlation. Li et al. [31] utilized a particle tacking flow visualization technique to obtain detailed hemodynamics parameters along the hood and the artery floor of an *in-vitro* model of the ETSDA of an arterial bypass graft. After analyzing their results, they suggested that anastomotic regions exposed to a combination of low and oscillatory WSS may be most prone to the formation of IH. Hofer et al. [32] and Leuprecht et al. [33] carried out fluid dynamics pulsatile numerical simulations to characterize the flowfield in different ETSDA models. They pointed out a low and oscillatory shear at sections of the arterial floor through the cardiac cycle and suggested that might correlate with the initiation of the floor IH.

Sottiurai [9] claimed that compliance mismatch is not the root cause of IH growth. He questioned the occurrence of IH on vein bypass grafts where compliance mismatch does not apply since vein grafts maintain a full endothelial lining that matched the arterial endothelial lining. He pointed out that the low and oscillating flow at the graft heel and toe is capable of altering the endothelium morphology in such a way where blood elements can enter the

13

subendothelial space to exert their proliferative influence on the SMCs. Mondy et al. [34] performed an experimental study of a rat carotid artery and found that the reduced shear stresses lead to an endothelial secretion of platelet derived growth factors (PDGF), which potentially stimulates the proliferation and migration of SMCs. In support of Mondy's observation [34], Liu [10] discussed how the activated platelets can release growth factors such the as the platelet derived growth factors (PDGF).

Ojha [16] used a photochromic tracer technique to visualize the pulsatile flow and determine the instantaneous value of the WSS within a 45° ETSDA model. His measurements led him to suggest, likewise to Sottiuruai [9] and Mondy [34], that the low WSS tends to promote intimal thickening at the toe and heel regions due to an enhances mass transfer of blood-borne materials to the arterial walls by increasing their residence time. Interestingly, Ojha dismissed the idea that the low WSS correlates with the host artery floor IH and presented the concept of high spatial and temporal variations of the WSS gradients to be behind the IH progression at that site. Loth el al. [35] determined the distribution of the IH thickness at the ETSDA of seven canine iliofemoral PTFE grafts after 12 weeks of implantation. Afterwards, they explanted the grafts and used their anastomoses to construct upscaled transparent models. They measured the WSS at various axial locations using laser doppler anemometry under pulsatile flow conditions similar to the ones found *in-vivo*. They established an inverse correlation between the WSS and the IH levels around the suture line, however they showed this inverse correlation did not hold on the floor of the host artery. Obviously, the findings of Loth [35] largely agree with the discussion extended by Ojha [16] with respect to the potential effect of the low WSS on the IH development at the graft toe and heel and the lack of correlation between the WSS and the IH initiation at the host artery floor.

In the course of his discussion, Ojha [16] explained that the high spatial gradient of the WSS causes the non-uniformity of the force distribution on the host artery floor that can create local deformation of the endothelial cells and possibly the sub-endothelial tissue. Ojha's high

SWSSG theory receives a substantial credibility from the work of DePaola et al. [36] and Tardy et al. [37]; In those two publications, the responses of the vascular endothelium to a disturbed flow region that includes both separation and reattachement caused by a the existence an obstruction was experimentally examined. The measurements indicated that near the reattachment region, the WSS is small but its gradient is high causing endothelial cells to suffer depletion and move away from that region. Also, near the reattachement region, the endothelial cells divide at a rate that is high compared with that of cells subjected to a uniform shear. Figure (2.5) reveals the damage incurred by the endothelium near the reattachement zone when compared to its original healthy morphology. Then, Figure (2.6) shows the axial position correspondence between the high SWSSG values and the reduced normalized endothelial cells density. Hsu et al. [38] demonstrated that high values of the SWSSG delay the motion of the endothelial cells to re-generate a denuded section of the endothelium. Leask et al. [41] built in-vitro model castings from harvested human cadaver coronary artery bypass grafts and upon performing flow visualization on the ETSDA using photochromic molecular image velocimetry they suggested that the high SWSSGs are likely factors of IH growth on the sharp curvatures of the anastomotic geometry. Steinman et al. [42] used a finite element based code for flow simulation in an ETSDA; after analyzing the WSS distribution, they indicated that the onset of IH formation could be the elevated SWSSG.

On the other hand, high values of the TWSSG reflects a significant temporal change in magnitude and direction of the shearing load on the endothelium. Those high temporal changes occur due to the stagnation point motion on the host artery floor and the flow reversal near the graft toe and heel. White et al. [40] provided a solid evidence that the TWSSG high values is principally behind the endothelial cells proliferation; this proliferation signals an endothelial dysfunction. Prior to the observation of White [40], Ojha [16] had brought up the effect of the unusual WSS temporal variation as far as cyclic stretching and relaxing the endothelium, which may trigger the initial response in the development of anastomotic IH. In a subsequent

publication, Ojha [44] used the same experimental setup as in [16] to show that the intimal thickening at the floor of the host artery may be a regulating biological response that diminishes the stagnation point motion and reduces the WSS temporal gradients. The numerical work of Steinman et al. [42] reinforces the hypothesis of the responsibility of the high TWSSG in provoking IH since it was noticed that the IH susceptible sites witnessed highly variable WSS behavior over the cardiac cycle. Sumpio et al. [43] showed that *in-vitro* cyclic stretching of the ECs results in their division and proliferation, which might set a pathogenesis of IH.
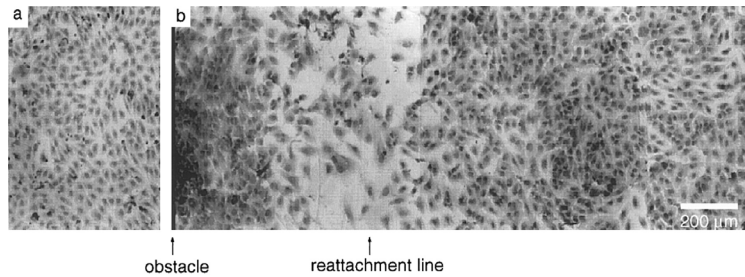
Figure 2.5: The endothelial damage cause by the high SWSSG [37].
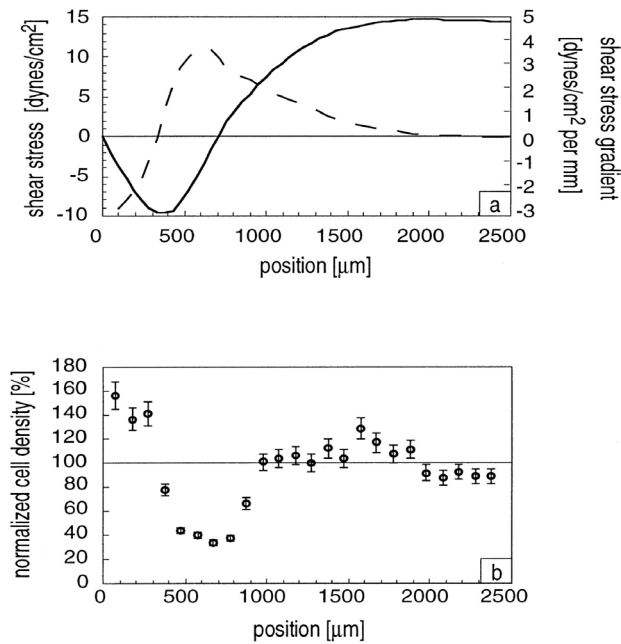
Figure 2.6: Spatial correspondence between the endothelial depletion and the high SWSSG [37].

16

the proliferation of the endothelium. A comprehensive review of the CFD simulation of the pulsatile blood flow in the bypass graft ETSDA can be found in the work of Lei et al. [45]. It is noted that all these studies utilized Finite Volume Method (FVM) or Finite Element Method (FEM) computational fluid dynamics codes both of which require tedious meshing that requires user interaction. The authors characterized the anastomotic velocity field and the host artery floor stagnation point motion, and then benchmarked those numerical results to available experimental results. Afterwards, they determined the distribution of the normalized WSS, mean SWSSG, mean TWSSG and OSI at the anastomotic surface area. An interesting observation from Lei's results lies in the focal nature of the SWSSG and TWSSG contours; Both variables present relatively high values near the toe, around the heel and at the sidewalls at the suture line.

2.4 ETSDA Shape Optimization Review

The optimization of the ETSDA configuration from a hemodynamics basis depends important design variables such as the anastomotic angle, the graft caliber and the anastomosis hood curvature. Other variables might come into play when incorporating the Miller Cuff or the Taylor Patch anastomosis models. The anastomosis design variables have to be subject to a limited range of values that depend of the judgment and experience of the performing surgeon in achieving the anastomosis.

Ojha et al. [46] experimentally investigated the effect of the anastomotic angle change on the WSS for an ETSDA under pulsatile flow conditions. Direct models with angles of 20°, 30°, 45° and 60° were examined. They found the presence of low WSS at the heel and the floor opposite from the heel. However, they noticed that increasing the angle led to an increased WSS on the host artery floor across from the toe and to a greater separation at the toe itself. They observed that the 20° angle anastomosis yielded the highest WSS at the toe region, which, assuming that the low WSS theory is correct, might reduce the growth of IH at the toe. Fei et al.

17

[47] numerically simulated the steady flow in the ETSDA of iliofemoral artery bypass grafts at anastomotic angles that varied among 20°, 30°, 40°, 45°, 50°, 60° and 70°. Their numerical results, as far as changing the angle, showed a high matching with the experimental results of Ojha [46]. Comparing their results with an analytical model that determine a critical biological shear stress, they suggested that the graft should be placed with a minimal anastomotic angle and that they should be exposed to high flows as opposed to low flows. Wijeshinghe et al. [48] applied a frame-by-frame video analysis to visualize the flowfield in direct and Miller Cuff ETSDA with different angles of 15°, 30°, 45° and 60°. They observed that increasing the anastomotic angle leads to an increased zone of flow separation and low WSS at the grafts heel and the host artery floor across from the heel. Unlike [46] and [47], they did not discuss significant hemodynamics advantages from changing the angle, rather they attributed the improved patency of the Miller ETSDA model to an increased ability to accommodate the IH expanding volume. O'Brien et al. [19] carried a CFD simulation to optimize various ETSDA geometries and found that decreasing the anastomotic angle always tends to decrease the abnormal hemodynamics. In [19], the abnormal hemodynamics was depicted by the peak-to-peak differences from the WSS and SWSSG on the floor of the host artery; The less those differences are the healthier the anastomosis condition becomes.

Lei et al. [17,50] conducted a numerical investigation to optimize the shape of the ETSDA based on reducing the elevated values of the SWSSG. They showed that increasing the graft caliber leads to a dramatic reduction of the SWSSG at the floor of the host artery in addition to other obvious SWSSG reductions at the graft heel and toe. In their anastomotic CFD analysis, O'Brien et al. [19] detected that increasing the graft caliber also entails tremendous reductions of abnormal hemodynamics.

Several publications addressed the hemodynamics-based benefits that result from vein cuffed or patched ETSDA due to their particular configurations that differ from the configuration of the conventional ETSDA. Noori et al. [49] performed flow visualization studies to investigate

the pulsatile flow patterns for Reynolds numbers between 100 and 500 in various femoral ETSDA models: the conventional model, the Miller cuff model, and the Taylor patch model. They reported similar flow behavior among the conventional and the Taylor Patch models; On the other hand, they showed that the Miller Cuff model yields the lowest cyclic shift of the stagnation point at the floor artery, which hints that the Miller Cuff model results in the lowest TWSSG at that anastomotic site as indeed is the observation of Ojha in [44]. They also pointed out the persistent washout of the anastomotic cavity in the Miller cuff model, which in turn boosts the levels of the WSS and hence reduces the IH caused by the low WSS. Fisher et al. [18] attempted to optimize the dimensions of the cuff height and diameter in the Miller Cuff ETSDA model using a flow visualization study that incorporates laser illumination of tracer particles. They found that cuff dimensions of 13 mm in length and that are the highest (8-11 mm) result in cohesive vortices and stable flow patterns that sustain a high WSS in the anastomosis cavity, thus inhibiting IH according to Kohler in [29].

Lei et al. [50] numerically proved that the usage of the Taylor Patch ETSDA model leads to huge reduction of the mean SWSSG at the anastomotic sites that are most prone to the formation of IH. Cole et al. [51] conducted a numerical simulation and checked that using the Talyor Patch ETSDA model contributes to the mitigation of the WSS ranges on the arterial floor, which takes the WSS closer to its physiological values. Walsh et al. [52] numerically investigated the flow changes associated with the Miller cuff and Taylor patch ETSDA models that may be the reason behind the improved patency of those models. They noticed that the peak SWSSG values for the cuffed and patched geometries are three times lower than those for the conventional geometry. In addition to studying the hemodynamics advantages of changing the anastomotic angle and the graft caliber, O'Brien simulated the flowfield in various Miller Cuff and Taylor Patch ETSDA models in an attempt to optimize their dimensions. They found that as the Miller cuff is higher, less abnormal hemodynamics is found; This observation aligns with the

one extended by Fisher in [18]. Besides, they noted that increasing the volume of the Taylor patch anastomosis model will always lead to improved hemodynamics of the arterial floor.

The studies reported in [17,18,19,46,47,50] did not discuss any formal optimization procedures but rather compared by trial-and-error a relatively small number set of geometric design variations. These efforts are classified as direct optimization methods that do not yield an accurate optimal shape of the ETSDA. A formal shape optimization method will rely on an automated design approach that yields optimization results to a high degree of accuracy as opposed to a direct optimization one. The only formal shape optimization approach for the ETSDA existing in the literature is that of Rozza [20,21] who employed the gradient-based method. The formal optimization problem in [20,21] was conducted based on minimizing the vorticity magnitude of the anastomotic flow. Nonetheless, as the gradient-based methods locally search for an optimal solution they might lead to a pre-mature convergence, i.e. converge to a local optimal solution that is not necessarily a global optimal solution as the optimization space might have several local maxima/minima.

In the current dissertation, the genetic algorithm (GA) is proposed as an optimization tool to enhance the shape of three different ETSDA models. The GA is an evolutionary approach that relies on a global search for the optimal solution within a prescribed search range. The GA search can be operated following both a single-objective and a multi-objective mode. The shape optimization of the ETSDA depends on three computational components: (1) the 'shape optimization genetic algorithm' (SOGA), (2) the LCMM solver [23,75], and (3) the automated pre-processor. The mission of the LCMM is used to evaluate the disturbed hemodynamics parameters, then the mission of the SOGA is to modify the ETSDA geometry based on the minimization of those parameters; the automated pre-processor serves to re-deploy computational points in the ETSDA geometry without an intervention from the user. The usage of the GA is more advantageous than the gradient-based methods. Due to the evolutionary aspect

of the GA it becomes very hard to converge to a local optimal solution as the GA search mechanism constantly scans the global search range to uncover the global optimal solution.

CHAPTER 3: THE LCMM FRAMEWORK

The current chapter provides the details of the LCMM as a specific class of meshless methods. The term "Meshless" is often confused by many as it might pertain to methods that need no elements in the computational domain, which is indeed incorrect. Meshless methods do not require a meshing procedure, but they rely on the non-ordered distribution of solution points in the computational domain. The LCMM numerical principles presented in this chapter will set a generic platform for modeling flow transport problems. The next chapter will carry the application of the LCMM principles to modeling incompressible Navier-Stokes equations in the laminar regime.

The first section of this chapter provides a review on meshless methods mainly as applied to fluid dynamics. The second section details the discretization approaches adopted in the LCMM and the automated pre-processor. The third section deals with the treatment of irregular boundary conditions, in particular the Neumann boundary condition. The fourth section entails the development of an upwind scheme that is suitable for the LCMM. The upwind scheme is augmented with a limiter to damp the numerical oscillations arising from the non-linearity of the advection terms as well as from the irregularity of the point distribution.

3.1 Review of Meshless Methods

Meshless methods are novel numerical techniques intended to significantly reduce if not eliminate the onerous mesh generation requirements of traditional numerical methods such as the Finite Volume Method (FVM) and the Finite Element Method (FEM). In industrial CFD applications, mesh generation is the most cumbersome task that comes at a high human and financial cost and is estimated to comprise over 50% of the cost of a computational simulation. This shortcoming has motivated researchers in the numerical method community to find

alternative methods for which the pre-processing of an intricate 2D and 3D geometries becomes a less burdensome task. Such research has led to recent interest and development of the so-called meshless methods that have successfully been used to resolve complex physics on a set of non-ordered points. Although not yet commercialized, meshless methods have demonstarted their validity throughout a wide spectrum of engineering applications including but not limited to solid mechanics [54,55], fluid dynamics [60,63], and heat transfer [56,23].

Meshless methods for flow transport problems rely on either localized or global formulations. In a given localized meshless formulation, the solution at any given point in the domain is influenced by the solutions at a local set of neighboring points. On the other hand, in a global meshless formulation each solution point is influenced by the solution at all the other points in the computational domain [56,57,58]. Although reported to converge spectrally, global meshless method formulation leads to a fully populated algebraic system that is often poorly conditioned. This raises serious numerical and storage issues in the case of large-scale 3D problems.

In this dissertation, we will focus on the review of the developments of localized meshless formulations for incompressible and compressible flows. A localized meshless formulation should lead to multiple "derivative vectors" at every point of the domain, each pertaining to a derivative of a certain order. As such, the nth derivative at a given point is evaluated by multiplying the nth derivative vector by another vector consisting of the field variable values at the point and at its neighbors. The localized meshless methods actually differ in how the derivative vectors are determined. In any localized meshless method, the field variable is estimated by a certain shape function. Some localized formulations use the Taylor series as a shape function, others use polynomials or radial basis functions (RBFs). A shape function depends, first on the Eucledian distances between the solution point and its neighboring points, and second on a set of expansion coefficients. An algebraic expression is derived for each expansion coefficient via some matrix inversion process. Depending on the localized

formulation, the matrix inversion process can be done directly by collocation or via a moving least square (MLS) technique. Expressing the expansion coefficients is a necessary step before determining the entries of any derivative vector.

3.1.1 Localized Formulations with Taylor Series

The localized meshless method using a Taylor-series-based formulation originates to the early publication of Chung [59] on the generalized finite difference (GFD) method. In this publication, the GFD method was applied to incompressible flows following the vorticity stream function scheme. The expansion coefficients in the GFD method of Chung were recovered without MLS treatment. As an illustration, Chung used his GFD approach to solve an incompressible flow problem involving natural convection in a mildly irregular parallelogrammatic geometry.

Sridar et al. [60] extended a localized meshless method that relies on a Taylor series to solve for compressible flows in the subsonic, transonic, and supersonic regimes. In their method, they had to incorporate the MLS technique when expressing the expansion coefficients. They presented Mach and pressure contour results over irregular geometries such as cylinders, airfoils, and ramps. Also, it is worth noting that their point distribution in the computational domain was highly non-ordered.

Recently, Chew et al. [61] introduced another attractive localized meshless method involving Taylor series expansions and MLS treatment to simulate incompressible flows over arbitrary geometries with moving boundaries. The solution points in this particular method are classified as fixed and free. The fixed points are distributed in a Cartesian manner and situated in the core of the geometry domain away from the boundaries; a simple finite differencing is applied there with no need for the meshless solution. The free points are situated by the boundaries and the localized meshless formulation is applied at those points. In fact, the free

points are expected to be in a constant non-ordered distribution as the boundary will be moving randomly and a meshless formulation is needed. The authors in [61], validated their method with the analytical solution of the vortex decaying benchmark problem and they succeeded in demonstrating that their method is second-order accurate both in space and time.

Similarly to the approach in [61], Luo et al. [62] presented a hybrid approach where a Cartesian mesh is built over arbitrarily shaped geometries. Needless to say that this sort of meshing will always lead to cut-off cells at the boundaries. To avoid the numerical issues that come along with cut-off cells, a meshless solution using Taylor series expansions and MLS treatment is applied over cell centers belong to the cut cells and their adjacent full cells. The solution over the rest of the full cells is determined using a finite volume approach. The examples in [62] include validated results for compressible flows in a 1D shock tube, over a 2D ramp, over a 2D submerged cylinder, and over a 3D submerged box.

3.1.2 Localized Formulations with Polynomials

Among the localized meshless formulation using polynomials there is the work of Onate et al. [63] who developed an explicit meshless technique called the "finite point method" (FPM). This technique relies on a weighted MLS treatment to obtain the "derivatives multiplication" vectors. Examples provided in [63] include driven cavity flow, flow over a backward facing step, flow over a submerged cylinder and flow over an airfoil; for all those examples the point distribution in the domain is random, reflecting the FPM capability of handling incompressible flows over irregularly distributed points. Zhang et al. [64] also incorporated a weighted MLS technique with a polynomial approximation to determine the spatial derivatives multiplication vectors. The approach of Zhang in [64] followed an implicit meshless formulation for the incompressible Navier-Stokes equations and results were validated via a driven cavity flow example.

25

The MLS treatment for the polynomial approximation was also used by Lin et al. [65] in their Meshless Local Petrov-Galerkin (MLPG) technique to simulate laminar incompressible flows. The MLPG technique inspires its formulation from the Petrov-Galerkin FEM and incorporates a stability perturbation parameter in the weak form of the continuity equation to satisfy the Brezzi-Babuska stability condition. The MLPG was tested for a body force flow and driven cavity flow problems. A similar work to [65] was carried out by Fries et al. in [66] where they addressed the Brezzi-Babuska stability condition for meshless methods based on the Petrov-Galerkin formulation.

The localized meshless formulation using polynomials and MLS treatment has also been used in modeling compressible flows. Kirshman et al. [67] proposed an innovative hybrid approach similar to that of Luo et al. [62] where the finite difference and meshless methods are combined. The point distribution in the domain is Cartesian except near the boundaries where the distribution lacks order. Then, the points are segregated depending on whether they have a complete finite difference topology or not. The meshless solution is applied over points mainly near the boundaries, where the finite difference topology is incomplete. Simultaneously, a finite difference scheme is applied over points where the finite difference topology is complete. The predicted Mach number and pressure contour compared favorably with benchmark solutions for transonic flows over a single-element airfoil. The authors in [67] were able to accelerate the solution process via multi-grid methods owing to the predominant Cartesian point distribution. Koh et al. [68] capitalized on the approach in [67], however the solution on points with a complete topology was conducted using a finite volume method instead of a finite difference one. The results in [68] include benchmarked solutions for compressible flows over both single-element and three-element airfoils.

3.1.3 Localized Formulations with Radial Basis Functions

As mentioned above, the RBFs are another type of shape functions used to establish localized meshless formulations. The RBFs can be collocated on a set of non-uniformly distributed points where the physics is governed by partial differential equations [69,70]. There are various classes of RBFs among which are the Polyharmonics, the Multiquadrics, and the Gaussians. The RBFs are more accurate than polynomials in terms of interpolating the values of a given field variable. The RBFs depend on shape parameters; those parameters are a source of sensitivity for the RBF and their values should be optimized.

Sarler et al. [74] adapted the RBF collocation method for the Darcy natural convection problem in porous media with successful benchmarking with a FVM solver; nevertheless, in this type of problems the momentum equation does not exhibit a non-linear behavior; non-linearity indeed constitutes a big challenge for the localized RBF collocation meshless method. No MLS treatment was reported in [74].

Divo and Kassab [23,75] developed a localized RBF collocation method the fully-coupled incompressible Navier-Stokes equations solved in strong form. This particular localized meshless method was called the Localized Collocation Meshless Method (LCMM). The RBF localized formulation in [23,75] seeks expressions for the expansion coefficients without any MLS treatment; this RBF localized formulation will be thoroughly discussed in the next section. The examples in [23,75] include successfully validated results of driven cavity flows, natural convection flows, flows over a square obstruction, and flows over a submerged cylinder. El Zahab et al. [24] used the LCMM to model the blood flow in three different ETSDA geometries that are irregular. A shortcoming of the LCMM as applied to those irregular geometries arise when the flow became convection-dominated, which has marked the need of stabilizing the LCMM; this stabilization procedure will be discussed later in this chapter.

Chen et al. [76] incorporated the RBF collocation method to solve the compressible flow Euler equations. The multi-quadric RBF was chosen as the shape function. Unlike the RBF approaches mentioned above, the expansion coefficients were recovered using the MLS technique and the equations were solved in weak form. The point distribution is Cartesian and adapts to the gradients of the flow solution. The method in [76] was able to properly capture shock waves in the transonic flow regime over a single-element airfoil. The authors claimed that the addition of the MLS treatment to the RBF collocation method serves in reducing the shape-parameter-based sensitivity.

3.2 The LCMM Spatial Discretizations

The attractiveness of the LCMM lies in its capability of performing spatial discretization over non-uniformly distributed computational points. Each computational point is connected to a set of neighboring points and this connectivity defines a local topology. The LCMM can handle the irregularly distributed points thanks to two of the localized meshless formulations: The radial basis function (RBF) collocation and the polynomial expansion with MLS treatment. In the current section we will first explain the creation of the local topology, second formulate the spatial discretization using both the RBF collocation and the MLS-based polynomial expansion, and third discuss the automated pre-processor that produces non-uniform point distributions near irregular boundaries.

3.2.1 The Local Topology Build-up

Every point on the domain boundary and interior of the discretized geometry is book-kept as a data center that recruits a set of neighboring influence points to make up a localized interpolation topology. It is over this topology of points that the field variable is estimated using

28

proper functions. For the LCMM, those functions consist of RBFs an polynomials. The total number of points in the topology including the data center and the neighboring influence points is denoted by NF. For a 2D geometry, the creation of the localized interpolation topology is accomplished by incrementally inflating a circle starting from the data center. In the case of a 3D geometry, a sphere is inflated instead.

The circle is inflated until it encompasses a prescribed number of influence points. The number of influence points depends on whether the data center is on the boundary or in the interior. For the data centers on the boundary, the inflated circle encompasses a minimum of 18 points in a 2D space and a minimum of 23 in a 3D space. The build-up of a typical topology for a boundary data center in 2D is shown in Figure (3.1a). It is important to mention that the topology around any given boundary data center should not include opposing boundaries or points around a re-entry corner as they have no physical influence on that boundary data center. For the data centers on the interior, the inflated circle should encompass a minimum of 13 points in a 2D space and a minimum of 32 in a 3D space. The build-up of a typical topology for a interior data center in 2D is shown in Figure (3.1b). The current topology structure is fixed, however this structure can be set to change based on the progress of the numerical solution. For example, the upwinding scheme adapted in the LCMM requires a modification of the topology size and structure; such a modification could actually take place as long as the numerical solution process is running in order to maintain stability for the solution.
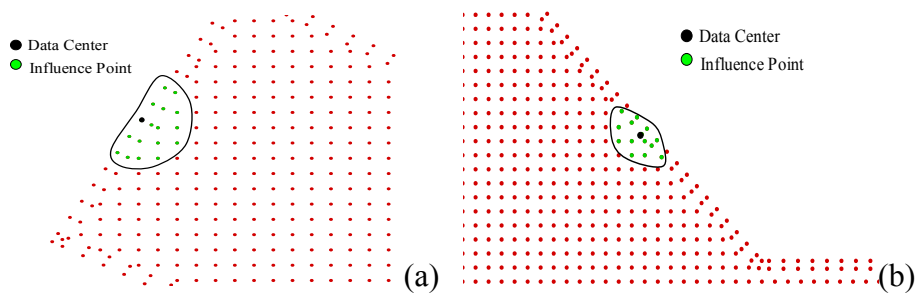
Figure 3.1: The topology build-up for a boundary data center (a) and an internal data center (b).

3.2.2 The Localized RBF Collocation

The value of a field variable, say ϕ, can be collocated at an arbitrary point i within the local topology by a RBF interpolation such as shown in Equation (3.1).

$$\phi_i = \sum_{j=1}^{NF} \alpha_j \chi_j(\boldsymbol{x_i}) \tag{3.1}$$

Here $\boldsymbol{x_i}$ represents the Cartesian coordinates of the collocation point i. The terms α_j represent the unknown expansion coefficients while the terms $\chi_j(\boldsymbol{x_i})$ are pre-defined expansion functions that depend on the Cartesian coordinates of the collocation point i and the Cartesian coordinates of the other points in the local topology. For the current Localized RBF collocation, the expansion function is chosen to be the Hardy Multiquadrics RBF [71], which is expressed in Equation (3.2).

$$\chi_j(\boldsymbol{x_i}) = \left[r_j^2(\boldsymbol{x_i}) + c^2 \right]^{n-\frac{3}{2}} \tag{3.2}$$

Where n is a positive exponent parameter, c is a shape parameter, and $r_j(\boldsymbol{x_i})$ is the Euclidean distance from $(\boldsymbol{x_i})$ to $(\boldsymbol{x_j})$, which represents the influence points Cartesian coordinates. Of all RBF's, Hardy Multiquadrics have been shown to offer superior interpolating properties.

Considering each of the local topology points as a collocation point, Equation (3.1) will be then collocated NF times leading to the following system of linear equations:

$$\begin{bmatrix} \chi_1(\boldsymbol{x_1}) & \cdots & \chi_{NF}(\boldsymbol{x_1}) \\ \chi_1(\boldsymbol{x_2}) & \cdots & \chi_{NF}(\boldsymbol{x_2}) \\ \vdots & \vdots & \vdots \\ \chi_1(\boldsymbol{x_{NF}}) & \cdots & \chi_{NF}(\boldsymbol{x_{NF}}) \end{bmatrix} \begin{pmatrix} \alpha_1 \\ \alpha_2 \\ \vdots \\ \alpha_{NF} \end{pmatrix} = \begin{pmatrix} \phi_1 \\ \phi_2 \\ \vdots \\ \phi_{NF} \end{pmatrix}$$

The above system can be written in a matrix-vector form as shown in Equation (3.3).

$$\{\phi\} = [\chi]\{\alpha\} \Rightarrow \{\alpha\} = [\chi]^{-1}\{\phi\} \tag{3.3}$$

where the matrix $[\chi]$ includes the value of each of the NF expansion functions $\chi_j(\boldsymbol{x})$ evaluated at all NF collocation points in the local topology.

To evaluate the field variable derivatives at the data center of the local topology, any linear differential operator $\mathcal{L}$ can be applied to equation (3.4) such as:

$$\mathcal{L}\phi_c = \sum_{j=1}^{NF} \alpha_j \, \mathcal{L}\chi_j(\boldsymbol{x_c}) \tag{3.4}$$

where $\boldsymbol{x_c}$ is the data center of the topology. Thus, in matrix-vector form:

$$\mathcal{L}\phi_c = \{\mathcal{L}\chi(\boldsymbol{x_c})\}^T \{\alpha\} = \{\mathcal{L}\chi(\boldsymbol{x_c})\}^T [\chi]^{-1} \{\phi\} = \{\mathcal{L}\}^T \{\phi\} \tag{3.5}$$

the vector $\{\mathcal{L}_c\}$ is composed by:

$$\{\mathcal{L}_c\} = \begin{pmatrix} \mathcal{L}\chi_1(\boldsymbol{x_c}) \\ \mathcal{L}\chi_2(\boldsymbol{x_c}) \\ \mathcal{L}\chi_3(\boldsymbol{x_c}) \\ \vdots \\ \mathcal{L}\chi_{NF}(\boldsymbol{x_c}) \end{pmatrix} \tag{3.6}$$

Therefore, the evaluation of any derivative at the data centers $\boldsymbol{x_c}$ is provided by a simple inner product of two vectors: $\{\mathcal{L}\}$ which can be pre-built and stored and $\{\phi\}$ which entries comprise of the updated field variable values at all the local topology points including the data center $\boldsymbol{x_c}$.

When dealing with the Hardy Multiquadrics RBF, one has to set the value of the exponent n to determine the specific multiquadric and has to set the value of the free parameter. In this dissertation, the exponent is set to $n = 1$, so that the inverse Multiquadrics RBF is taken as the expansion function of choice. Inverse multiquadrics have been studied in depth and have been shown in the literature to possess superior interpolating properties in 2D and 3D [69,70,71,72]. The shape parameter, c, controls the interpolation behavior of the RBF. For a local interpolation over a given data center, the RBF functions become flatter and the RBF interpolation becomes more accurate as the magnitude of c is increased [73]. Nevertheless, the increase of this magnitude should be to a certain limit beyond which the interpolation matrix $[\chi]$

becomes ill-conditioned. The ill-conditioning limit of the interpolation matrix $[\chi]$ is determined by its conditioning number that is set to remain between 10^{10} and 10^{12} for double precision calculations. The interpolation matrix conditioning number is found by dividing the largest singular value by the smallest singular value of the interpolant matrix of each data center and, to ensure an optimal value of c, an iterative search algorithm is incorporated to yield a conditioning number value between 10^{10} and 10^{12}.

Moreover, to ensure that constant and linear fields are exactly captured, the RBF local interpolation expressed in Equation (3.1) is enriched (completed) by the addition of a polynomial. As such, the field variable at an arbitrary point i within the local topology can be recast such as shown in Equation (3.7).

$$\phi_i = \sum_{j=1}^{NF} \alpha_j \chi_j(\boldsymbol{x_i}) + \sum_{j=1}^{NP^*} \alpha_{NF+j} P_j(x_i) \tag{3.7}$$

Incorporating completeness conditions in the collocation process leads to the augmented collocation matrix equation:

$$\begin{bmatrix} \chi_1(\boldsymbol{x_1}) & \dots & \chi_{NF}(\boldsymbol{x_1}) & P_1(\boldsymbol{x_1}) & \dots & P_{NP^*}(\boldsymbol{x_1}) \\ \vdots & & \vdots & \vdots & & \vdots \\ \chi_1(\boldsymbol{x}_{NF}) & \dots & \chi_{NF}(\boldsymbol{x}_{NF}) & P_1(\boldsymbol{x}_{NF}) & \dots & P_{NP^*}(\boldsymbol{x}_{NF}) \\ P_1(\boldsymbol{x_1}) & \dots & P_1(\boldsymbol{x}_{NF}) & 0 & \dots & 0 \\ \vdots & & \vdots & \vdots & & \vdots \\ P_{NP^*}(\boldsymbol{x_1}) & \dots & P_{NP^*}(\boldsymbol{x}_{NF}) & 0 & \dots & 0 \end{bmatrix} \begin{pmatrix} \alpha_1 \\ \vdots \\ \alpha_{NF} \\ \alpha_{NF+1} \\ \vdots \\ \alpha_{NF+NP^*} \end{pmatrix} = \begin{pmatrix} \phi_1 \\ \vdots \\ \phi_{NF} \\ 0 \\ \vdots \\ 0 \end{pmatrix}$$

The polynomial enrichment will subsequently take effect on the evaluation of the multiplication vector $\{\mathcal{L}\}$ that is expressed in Equation (3.6), and this is a straightforward extension.

3.2.3 The Polynomial MLS Approximation

The value of the field variable ϕ can be approximated at an arbitrary point i within the local topology by the MLS-based polynomial interpolation. This is another way for evaluating ϕ

in addition to the local RBF collocation, and this approach turns out to be effective in determining one-sided derivatives that appear in the convective terms of the fluid flow momentum conservation equations. The approximated value of ϕ can be set to be equal to the multiplication of a polynomial basis vector P and a polynomial coefficients vector β. Each entry in P is a monomial and the total number of those entries is denoted by NP. The value of ϕ at an arbitrary point i within the local topology is approximated as,

$$\widehat{\phi}(x) = \sum_{j=1}^{NP} P_j(x)\beta_j \tag{3.8}$$

The polynomial basis vector can have as many entries as desired. For example, in Equation (3.9), shows a polynomial basis vector in a 2D Cartesian coordinate system, taken up to the first six entries of the Pascal triangle.

$$P_j(x_i) = \begin{pmatrix} 1 \\ x \\ y \\ xy \\ x^2 \\ y^2 \end{pmatrix} \tag{3.9}$$

Increasing NP leads to a high-order approximation as well as to an increase in the computational cost. The number of points in the local topology NF should be at least equal to NP to avoid numerical instabilities.

A standard least squares fit is accomplished by first defining scalar measure, E, of the sum of the squares of the errors between the nodal value ϕ and the polynomial expansion approximation $\widehat{\phi}$ at each point of the local topology,

$$E = \sum_{i=1}^{NF} \left(\phi_i - \widehat{\phi}_i \right)^2 = \sum_{i=1}^{NF} \left(\phi_i - \sum_{j=1}^{NP} P_j(x_i)\beta_j \right)^2 \tag{3.10}$$

In order to determine each polynomial coefficient, say the mth polynomial coefficient, the derivative of E with respect to the mth polynomial coefficient should be set to zero such as shown in Equation (3.11) so that the magnitude of E is extermized,

$$\frac{\partial E}{\partial \beta_m} = \sum_{i=1}^{NF} - 2P_m(x_i)\left(\phi_i - \sum_{j=1}^{NP} P_j^T(x_i)\beta_j \right) = 0 \tag{3.11}$$

or

$$\sum_{i=1}^{NF} P_m(x_i)\left(\phi_i - \sum_{j=1}^{NP} P_j^T(x_i)\beta_j \right) = 0 \tag{3.12}$$

leading to the standard normal equations for least squares fit of a polynomial,

$$\sum_{i=1}^{NF} P_m(x_i)\phi_i = \sum_{j=1}^{NP} \beta_j \left[\sum_{i=1}^{NF} P_m(x_i)P_j^T(x_i) \right] \tag{3.13}$$

Recognizing Equation (3.13) for the NP polynomial coefficients, one can establish the following algebraic system:

$$[B]_{NP \times NF}\{\phi\}_{NF \times 1} = [A]_{NP \times NP}\{\beta\}_{NP \times 1} \tag{3.14}$$

$$\Rightarrow \{\beta\}_{NP \times 1} = [A]^{-1}_{NP \times NP}[B]_{NP \times NF}\{\phi\}_{NF \times 1} \tag{3.15}$$

The elements of A and B are given in Equations (3.16) and (3.22) respectively.

$$A_{mj} = \sum_{i=1}^{NF} P_m(x_i)P_j(x_i) \tag{3.16}$$

$$B_{mi} = P_m(x_i) \tag{3.17}$$

The application of a linear differential operator over the field variable $\phi(\boldsymbol{x})$ at the data center $\boldsymbol{x_c}$ is then given by:

$$\mathcal{L}\phi(\boldsymbol{x_c}) = \sum_{j=1}^{NP} \alpha_j \mathcal{L}P_j(\boldsymbol{x_c}) \tag{3.18}$$

or in matrix-vector form:

$$\mathcal{L}\phi_c = \{\mathcal{L}P_c\}_{1\times NP}^T \{\alpha\}_{NP\times 1} \tag{3.19}$$

Introducing the expansion coefficients α_j leads to:

$$\mathcal{L}\phi_c = \{\mathcal{L}P_c\}_{1\times NP}^T [A]_{NP\times NP}^{-1} [B]_{NP\times NF} \{\phi\}_{NF\times 1} \tag{3.20}$$

and therefore the evaluation of any derivative at the data center $\boldsymbol{x_c}$ can be reduced to a vector-vector multiplication of the form:

$$\mathcal{L}\phi_c = \{\mathcal{L}_{ls}\}_{1\times NF}^T \{\phi\}_{NF\times 1} \tag{3.21}$$

where the least-squares operator vector $\{\mathcal{L}_{ls}\}_{1\times NF}^T$ is explicitly built as:

$$\{\mathcal{L}_{ls}\}_{1\times NF}^T = \{\mathcal{L}P_c\}_{1\times NP}^T [C]_{NP\times NP}^{-1} [P]_{NP\times NF} \tag{3.22}$$

The MLS approximation of the convective derivative will be discussed later.

3.2.4 The LCMM Automated Pre-processor

The advantage of using the LCMM automated pre-processor is to perform an instantaneous point distribution in the physical domain of interest. When dealing with any geometry, classical numerical techniques such as the FVM and the FEM require a well-structured body fitted mesh in order to produce valid results. However, the process of building a body-fitted mesh has to be done interactively by the user in a careful manner to avoid any skewness in the mesh. The generation of a body-fitted mesh over the conventional ETSDA geometry is illustrated in Figure (3.2); notice how the mesh propagates smoothly and curvilinearly within the boundaries of the geometry as a result of the user's care. In the case of a complex three-dimensional geometry CFD analysis, dividing the domain into multi-blocks

becomes necessary, which further makes the mesh generation task daunting and time-inefficient. One solution to this issue is using a FVM/FEM unstructured mesh generator that can perform a simplified pre-processing. Even so, the solution processing over a FVM/FEM unstructured mesh suffers from numerical diffusion in the case of fluid flows where the inertia forces are dominant.

The automated pre-processor employed for the LCMM remotely distributes solution points in the physical domain in a relatively very short time; this will indeed spare all the human effort and time allocated to the generation of a body fitted mesh when using the FVM/FEM. There is actually no need to map the physical domain onto a computational one when using the LCMM as it is frequently done in the FVM/FEM. An example showing the point distribution executed by the automated preprocessor in the ETSDA vicinity is shown in Figure (3.3); no human effort was needed to design this point distribution. The interior points follow a Cartesian uniform distribution everywhere except near the boundary where they have no pre-defined connectivity with the boundary points as it is shown in Figure (3.4). The LCMM ability of treating the irregularity between the boundary points and their adjacent internal points justifies the "Meshless" notion.

The pre-dominant Cartesian distribution of the internal points significantly mitigates numerical dissipations in the solution, hence putting the usage of the current automated pre-processor at an advantage over the usage of a traditional FVM/FEM unstructured mesh generator. Besides, the Cartesian point distribution is very convenient for multi-points methods that serve for convergence acceleration. The automated pre-processor is also capable of performing a quadtree/octree points distribution, which is practical for near-wall points clustering applications. The quadtree-based automated LCMM pre-processor discussed in Mitteff et al. [77] can readily be adapted for automated data center control and distribution, moreover, the authors discuss an automated data segmentation for parallel computing applications.

The LCMM automated pre-processor only requires the geometry information as an input. For a two-dimensional analysis, the geometry corners coordinates and the point distribution density on each boundary edge suffice as input information. Once the geometry information is specified, the boundary points will be distributed uniformly along the boundary. Opposite to its outward drawn normal vector direction, each boundary point will create one neighboring internal shadow point that serves to evaluate the boundary normal derivative, as will be discussed in the following section.

The irregularity or order independence between the boundary points and their adjacent internal points is very convenient to the present autonomous ETSDA shape optimization application. As stated in chapter 2, shape optimization should be undertaken by minimizing the adverse hemodynamics parameter(s) by continuously modifying the ETSDA geometry. This modification in the geometry is not meant to be controlled by the user, rather it should be controlled by an automatic procedure controlled by the GA: (1) modifying the geometry shape, and (2) perform an automatic point distribution by which the distribution of the boundary points and their adjacent internal points is not necessarily ordered. Attempting a similar procedure using a structured FVM/FEM mesh generator could note lead to such a seamless automated process. Each geometric change dictated by the GA optimizer requires a certain customization of the structured mesh generator; this customization has to be unique for the particular geometry to be modified, thereby ensuring that no cell skeweness occur during the re-meshing process after the geometry modification. So for each geometry to be optimized, there should be a different mesh generation strategy and user interaction would be required at each iteration. In contrast, there is no customization required for the LCMM automated pre-processor as it follows the same Cartesian point distribution strategy for any given geometry, and a quadtree approach is readily automated when refinement is required. Recognizing this advantage of the LCMM automated pre-processor over traditional FVM/FEM mesh generators in terms of human and time overhead,

the LCMM is considered a most suitable solver to be repeatedly invoked in an automated shape optimization procedure.
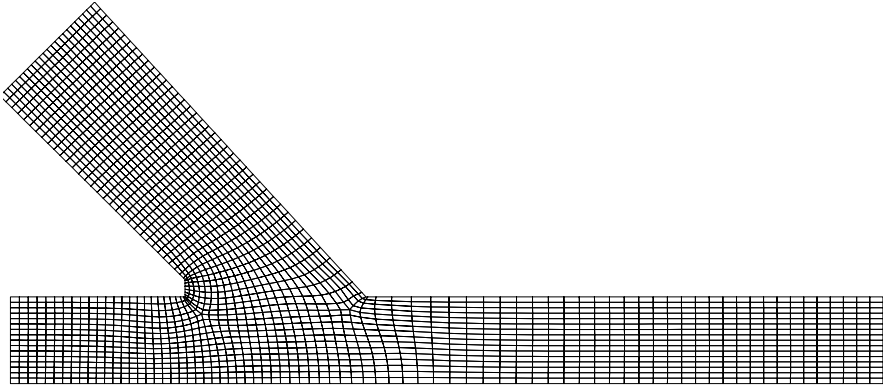
Figure 3.2: A body-fitted mesh generated over the conventional ETSDA geometry.
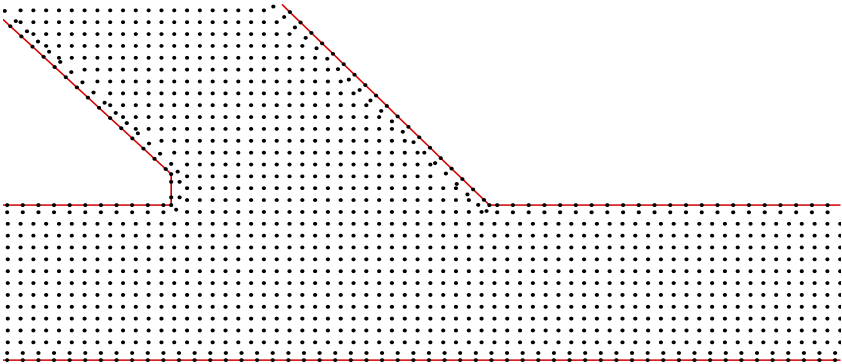
Figure 3.3: An automated point distribution over the conventional ETSDA geometry.
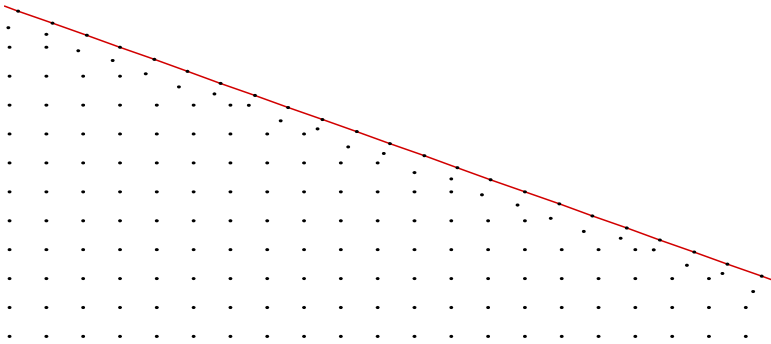
Figure 3.4: The order independence between the boundary and internal points.

3.3 Boundary Conditions Treatment

A common problem for node-based or point-based methods is the treatment of boundary conditions over arbitrary geometries with irregular boundaries where the point distribution becomes highly non-uniform. Several researchers have addressed the issue of irregular boundaries, especially for the treatment of the Neumann's boundary condition. The current section provides a review of some of the efforts to deal with boundary conditions, especially the Neumann boundary condition, on irregular boundaries. In addition, the formulation of the shadow-point-based Neumann boundary condition treatment adapted in the LCMM is presented in detail.

3.3.1 Review of Treatment for Irregular Boundaries

Tannehill at al. [78] addressed the issue of boundary condition treatment on highly irregular geometries; they discussed three discretization methods to evaluate derivatives for irregularly distributed boundary and internal points. The first method uses a fine Cartesian internal point distribution near the boundary and assumes the closest internal points to the boundary as actual boundary points. The shortcomings of this approach lie in the "zig-zag" appearance of the boundaries, plus the large number of computational points needed to mask this "zig-zag" appearance. The second method uses linear interpolations to evaluate the field variables at irregular points, however this approach neglects the application of the physical equations at those points potentially yielding inaccurate results. The third method requires a generalized finite-difference (GFD) approximation of the physical equations at the irregular points; this approach could work well when a Dirichlet (1st kind) boundary condition is applied, however this approach performs poorly when a Neumann (2nd kind) boundary condition is applied.

Chung [59] extended a GFD formulation for the Neumann boundary condition, which involves a local mapping of the Cartesian coordinate at the boundary points; however, his incompressible flow example only reveals a slight irregularity between the boundary points and their adjacent internal points. Koh et al. [68] adapted a MLS-based meshless technique along with local mapping to handle the Neumann boundary condition when applied to the solution of the Eulerian flow over an airfoil; the boundary and internal points distribution at the airfoil surface clearly is irregular. Onate et al. [63] added a stabilizing term to the Neumann boundary condition equation in their MLS-based method to mitigate the instabilities arising due to the disorder between the boundary points and their neighboring internal points.

In the current LCMM technique, the Neumann boundary condition is accommodated by the addition of the internal shadow point to the boundary point. A forward finite differencing in the normal direction to the surface is implemented to evaluate the normal derivative at the boundary, without performing any coordinate mapping. The shadow point adds more irregularity to the point distribution at the boundary presenting more challenge to the LCMM. It should be noted that additional shadow points may be added

3.3.2 Shadow Point Treatment for The Neumann Boundary Condition

The field variable ϕ at an arbitrary boundary data center i can be evaluated by applying the generalized boundary condition equation given in Equation (3.23).

$$\eta\left(\frac{\partial \phi}{\partial n}\right)_i + \gamma\phi_i = \zeta \tag{3.23}$$

For the arbitrary boundary data center i, a normal derivative vector $\{\partial n\}$ may be derived in order to evaluate the normal derivative thereat. Thus, Equation (3.25) may be written as:

$$\eta\{\partial n\}^T\{\phi\} + \gamma\phi_i = \zeta \tag{3.24}$$

However, unlike other derivatives, the normal derivative at a boundary data center is influenced by the field variable solution at only two points: the boundary data center (ϕ_i) and its corresponding shadow point ($\phi_{shadow.i}$). As such, the normal derivative vector will only have two entries (∂n_1 and ∂n_2) and the normal derivative can be calculated by a simple finite difference in space between the boundary data center and its corresponding shadow point. Following the shadow point approach, the normal derivative interpolation vector $\{\partial n\}$ can be computed as:

$$\{\partial n\} = \begin{pmatrix} 1/r_s \\ 0 \\ \vdots \\ 0 \\ -1/r_s \\ 0 \\ \vdots \\ 0 \end{pmatrix} \tag{3.25}$$

where r_s is the distance from the boundary data center to its corresponding internal shadow point. Notice that all of the elements of the interpolation vector except two vanish. Additionally, higher order differentiation can be accomplished by simply inserting multiple rows of internal shadow points in the normal direction of each boundary data center.

Subsequently, the generalized boundary equation can be manipulated to yield an explicit expression of the field variable ϕ_i at the boundary data center such as shown in Equation (3.26).

$$\phi_i = \frac{\zeta - \eta \partial n_2 \, \phi_{shadow.i}}{\eta \partial n_1 + \gamma} \tag{3.26}$$

The current approach for determining the normal derivative is straightforward. The disadvantage however consists of the extra point irregularity caused by the shadow point addition. This complexity is cured thanks to the capability of the localized meshless formulation to provide solutions over points that are irregularly distributed. This is a new approach to handling boundary conditions on arbitrary geometries.

41

3.4 The LCMM Upwinding Techniques

Care should be taken in evaluating the field variable first-order derivatives appearing in the convective terms of a given transport equation for convection-dominated transport problems. For the numerical solution of any transport equation, an upwinding technique combined with a limiter becomes necessary when the convection effects acting in the flow stream-wise direction outweigh the diffusion effects.

This section first presents a review on some of the upwinding/limiter techniques that have been adapted in some of the traditional methods as well as in localized meshless methods. Then, a high-order upwinding scheme algorithm, specifically devised for the LCMM, is discussed in details; this upwinding scheme is augmented with a limiter. Subsequently, 1D and 2D results are presented to illustrate the accuracy of the LCMM upwinding/limiter scheme.

3.4.1 Review of Upwinding and Limiters Techniques

Upwinding is a natural technique by which numerical instabilities arising from evaluating the convective derivatives by central difference. In an upwinding process, the evaluation of the convective term at a given point is mostly influenced by the field variable values at the flow upstream locations. Stabilization techniques for convection-dominated transport problems date back to the work of Gudonov [79] who, by establishing monotonicity criteria, proved that the first-order upwinding scheme is always stable. Nonetheless, the first order upwinding suffers from numerical diffusion, thus higher-order upwinding schemes are needed for accuracy purposes. The QUICK scheme of Leonard [80] is one of the upwinding schemes that provides a high-order of accuracy. Even so, using a high-order scheme solely yields stable but oscillatory solutions; these stable oscillations require further limiting techniques. The Flux Corrected Transport (FCT) technique of Borris and Book [81] is the first such limiter to be proposed, and,

here, a stable solution is sought by balancing first and higher order upwinding schemes. Other classes of limiting techniques are the 'Total Variation Diminishing' (TVD) and the 'Normalized Variable Diagram' (NVD) based schemes. The TVD and NVD schemes are typically employed in the FVM. The TVD and NVD schemes lead to the evaluation of the "face value", which the value of the transported field variable at a given face of the finite volume cell. Let us now consider the 1-D linear wave transport equation shown in Equation (3.31) where a field variable ϕ is purely convected with a constant convection speed a:

$$\frac{\partial \phi}{\partial t} + a\frac{\partial \phi}{\partial x} = 0 \qquad (3.27)$$

With the presence of a convection term and the absence of a diffusion term, Equation (3.31) makes a good robustness test for a given stabilization scheme of convection-dominated transport problems. A diffusion term inherently stabilizes to the solution, thus it should be eliminated to ensure that the convective term is properly treated by the stabilization scheme. Consider the 1D point distribution shown in Figure (3.5) where Equation (3.31) is the governing equation. The point i is at the center of a 1D finite volume cell and the face value is needed at the $i - 1/2$ and $i + 1/2$ faces so that the convective term could be determined. Those face values can be evaluated in a stable manner via a TVD/NVD scheme.
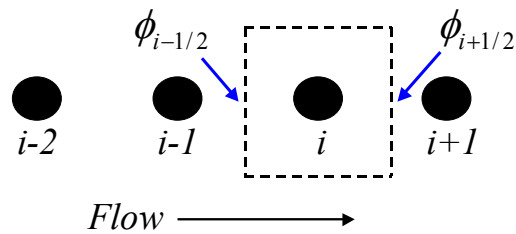

Figure 3.5. 1D point distribution.

Following a TVD scheme, the face value $\phi_{i-1/2}$ given the flow direction in Figure (3.5) is expressed as:

$$\phi_{i-1/2} = \phi_i + \frac{1}{2}\psi\big(r_{i-1/2}\big)[\phi_i - \phi_{i-1}] \tag{3.28}$$

In Equation (3.28), $\psi\big(r_{i-1/2}\big)$ is a limiter function that depends on the limiter ratio $r_{i-1/2}$; this limiter ratio in turn depends on the field variable values and is expressed in Equation (3.29).

$$r_{i-1/2} = \frac{\phi_i - \phi_{i-1}}{\phi_{i-1} - \phi_{i-2}} \tag{3.29}$$

A similar process is carried out to determine $\phi_{i+1/2}$ in terms of $\psi\big(r_{i+1/2}\big)$. For any scheme to be TVD, hence stable, the limiter function ψ has to lie within the TVD monotonicity region; this monotonicity region is marked by the blue-hatched regions shown in Figure (3.6). If the limiter function ψ does not belong to this region then a first order upwinding should be applied. There are several TVD schemes reported in the literature, among which the Minmod by Harten [82], Muscl by Van Leer [83], Osher [84], and Superbee by Roe [85]. The main criterion that differentiates those TVD schemes is the limiter function expression in terms of the limiter ratio. The behaviors of the Minmod, Muscl, Osher and Superbee TVD schemes are revealed on the Sewby ψ-r diagrams shown in Figure (3.6).

On the other hand, given the flow direction in Figure (3.5), the NVD scheme procedure to determine $\phi_{i-1/2}$ starts by normalizing ϕ_{i-1} as shown in Equation (3.30).

$$\widetilde{\phi}_{i-1} = \frac{\phi_{i-1} - \phi_{i-2}}{\phi_i - \phi_{i-2}} \tag{3.30}$$

Then, the face normalized field variable $\widetilde{\phi}_{i-1/2}$ is expressed in terms of $\widetilde{\phi}_{i-1}$. When expressed however, $\widetilde{\phi}_{i-1/2}$ has to satisfy the convection boundness criterion (CBC). More details can be found on the CBC in the work of Gaskell et al. [86]. The CBC has a diagrammatic representation as revealed in Figure (3.7a). The blue-hatched triangular region is where the normalized field variable $\widetilde{\phi}_{i-1/2}$ maintains a monotonic behavior between point $i - 2$ and i. If the value of $\widetilde{\phi}_{i-1}$ is not between 0 and 1 or the value of $\widetilde{\phi}_{i-1/2}$ falls outside of the CBC monotonic triangular region, then a first order upwinding should be applied. In [86], Gaskell introduced a high-order accurate algorithm called the SMART; The monotonic behavior of $\widetilde{\phi}_{i-1/2}$ based on the SMART algorithm

is illustrated in Figure (3.7a). Leonard [87] later developed a NVD-based universal limiter by which the CBC region was modified for the unsteady pure convection equation (Equation 3.31). In [87], the geometry of the CBC triangle was parameterized by the Courant number Co (See Figure 3.7b). Jasak et al. [88] presented a virtual-point-based NVD approach for upwinding on unstructured finite volume meshes.

The issue of numerical instability in convection-dominated transport problems is also addressed in localized meshless methods. In fact, the instability of the convection terms is enhanced by the non-uniformity of the point distribution often encountered in meshless methods. In their Taylor-series-based localized meshless method for compressible flows, Sridar et al. [60] incorporated a flux difference splitting scheme to estimate upwinding fluxes at virtual faces around meshless points. Luo et al. [62] used a HLLC Riemann scheme combined with a Van-Albada flux limiter in their compressible flows meshless method to estimate fluxes at virtual faces around meshless points. In both [60] and [62], a least square approach was used to approximate the flux derivatives at the meshless solution point. Onate et al. [63] employed a finite calculus procedure that stabilizes the incompressible flow solutions. The finite calculus technique is based on re-deriving a given conservation equation with the retention of high-order terms; this derivation leads to a stabilizing term that corrects the error introduced by the convection effects and the point distribution non-uniformity. Lin et al. [65] introduced upwinding effects to their incompressible flows MLPG method by shifting the test function local-subdomain opposite to the flow streamline direction. Ghandhini et al. [89] incorporated a RBF collocation upwinding approach for the 1D advection-diffusion equation. Gu et al. [90] developed an upwinding technique for RBF-collocation-based meshless solutions of the advection-diffusion equation. In the 2D upwinding examples in [90], the first-order derivative at the data center is only influenced by the solutions at the upstream points. The number of upstream points picked depends on the local Peclet number at the data center.
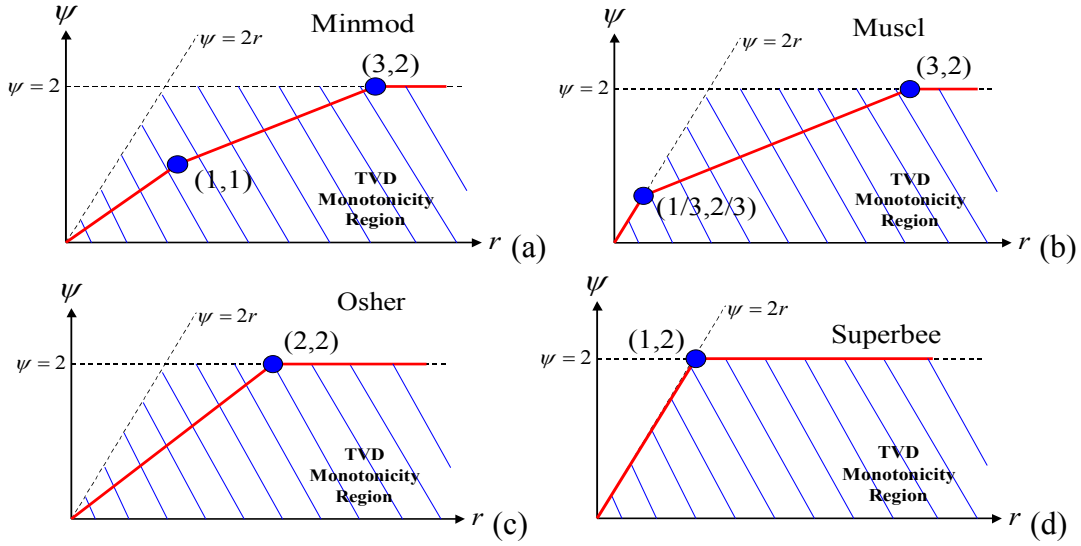
Figure 3.6: ψ behavior for the Minmod (a), Muscl (b), Osher(c), and Superbee (b) TVD schemes.
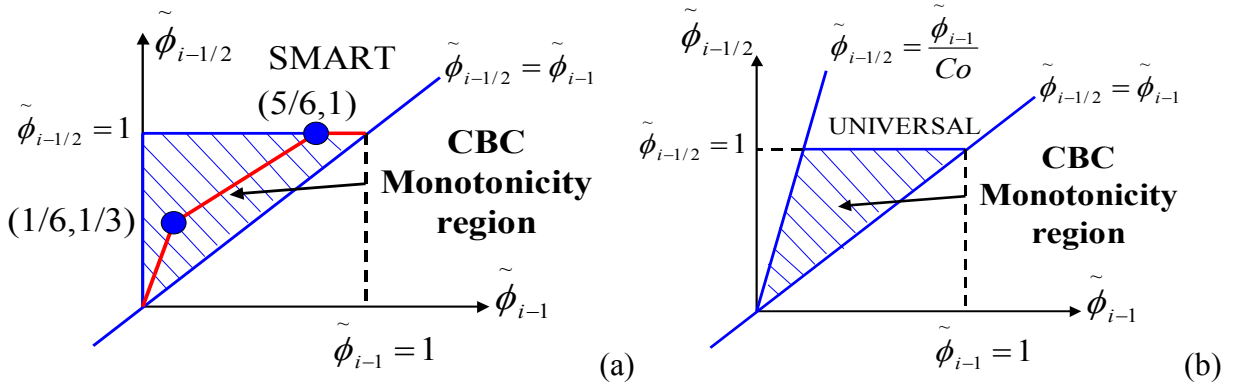
Figure 3.7: The standard (a) (with SMART limiter behavior) and universal (b) NVD diagrams.

3.4.2 The LCMM Upwinding and Limiter Scheme

So far, we have explained how the field variable derivatives are evaluated on a standard local topology. Recall that this standard topology is built by a circle/sphere inflation from the data center. Since the RBF collocation and polynomial MLS approximation are performed over a local topology of NF points, then each of the derivative vector and the influential field variable vector will have NF entries. When evaluating the convective term first-order derivative in any

transport equation based on the standard topology, the solution unfortunately generates severe numerical oscillations; those oscillations are unstable and eventually lead to a corruption of the solution. Thus, a stabilization technique for the convective terms should be introduced to the LCMM.

The stabilization of the LCMM requires the modification of the standard topology structure and size. We call the modified topology as the 'upwinding topology'. In the upwinding topology, the data center is no longer at the center of the topology and the number of points is reduced from NF to NU. Instead of inflating a circle/sphere, a sector/cone is drawn from the data center upstream-wise to recruit upstream influence points that are indispensable for the upwinding process. The closest upstream point to the data center can be singled out of the upstream points and is referred to as the 'close upstream point'; the rest of the upstream points will be then referred to as the 'far upstream points'. The drawn sector/cone has a fixed angle of 41.41° and a radius that is equal to double the distance between the data center and the close upstream point. Then, the data center recruits the closest downstream point as it adds more accuracy to the upwinding process. So after all, the upwinding topology will be comprised of the data center, the close upstream point, the far upstream points, and a single downstream point; the sum of all those points will be NU. A typical upwinding topology structure is shown in Figure (3.8) for a uniform point distribution (a) and a non-uniform point distribution (b).

For the LCMM-based upwinding process, the inverse Multiquadrics RBF is the only shape function used to determine the derivative vectors. The usage of a polynomial shape function is unfeasible as the upwinding topology might not have enough points for a high-order polynomial expansion. The RBF collocation over the upwinding topology is performed like-wise to the RBF collocation over the standard topology. The RBF is collocated NU times over the upwinding topology leading to the expression of NU expansion coefficients. Thereafter, the NU expansion coefficients expressions are incorporated in the RBF first-order derivative collocation to yield the upwinding derivative vector consisting of NU entries. The upwinding

47

derivative vector then multiplies a vector of NU influential field variables to evaluate the convective term first-order derivative. Following that, the value of the field variable is updated in an explicit manner. We refer to the upwinding by RBF collocation over NU points as "major upwinding".

For highly convective flows, the updated field variable value often exhibits an oscillatory behavior even with the application of a major upwinding. Thus, a limiter should be introduced to the current upwinding technique to suppress potential oscillations. Compared to the cell-based FVM, the LCMM is a point-based method where no cell face values are reconstructed. Hence, a direct application of the TVD or NVD limiter schemes is not possible. However, the TVD and NVD concepts of monotonicity could be used as basis to form a limiter for the LCMM. The following describes a limiter strategy for the LCMM. We first designate string(s) of points in the upwinding topology. Each string of points is called a 'monotonicity string' and comprises of the downstream point, the data center, the close upstream point, and one far upstream point. Thus, the number of monotonicity strings in an upwinding topology is equal to the number of far upstream points. Upon updating the field variable value, we detect if this value is a minimum or a maximum in at least one of the monotonicity strings. If neither a minimum nor a maximum is detected in all the monotonicity strings, then no limiting action is needed. If a minimum or a maximum is detected in at least one the monotonicity strings, then the major upwinding topology is further reduced to a minor one that only includes the data center and the close upstream point. A new RBF collocation is performed over this minor topology yielding a two-entries derivative vector. We refer to the upwinding with RBF collocation over the data center and the close upstream point as "minor upwinding". As we will show, the RBF collocation over a minor topology leads to stable results, however, these are highly dissipative. Following the minor upwinding, the field variable value is re-updated with an ensured stability. Figure (3.9) illustrates the LCMM upwinding/limiter technique algorithm flowchart involving major and minor upwindings where ϕ (phi) is the field variable.

3.4.3 One-Dimensional (1D) LCMM Upwinding Results

The current sub-section presents 1D validation results for the LCMM upwinding/limiter scheme which algorithm flowchart is shown in Figure (3.9). Studying the validity of any upwinding/limiter technique as applied to a linear wave equation is a necessary step before applying this technique to more complex transport equations. The present validation is based on studying the time decay of a signal that is being linearly convected by a convection speed a; as such, the equation that governs the transport of this signal is nothing but Equation (3.31). The 1D space is discretized by the means of meshless points that are equally spaced by a distance $\Delta x=0.01$ (m). The chosen signal consists of a unit-step profile and a unit-amplitude squared-sine profile extending over a width of 20 Δx. The signal is shown in Figure (3.10) at its initial condition. The robustness of the LCMM upwinding/limiter scheme is tested with two different Courant numbers (Co): $Co = 0.03$ and $Co = 0.1$. Recall that the Courant number is expressed as $Co = a\Delta t/\Delta x$.
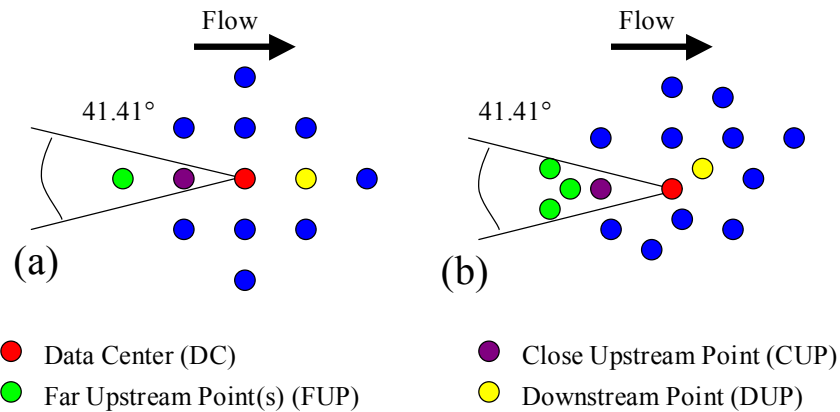
Figure 3.8: The upwinding topology for the uniform (a) and non-uniform (b) point distributions.

Figure (3.11) shows a comparison between the exact solution of the convected signal and the numerical solutions obtained by the major and minor RBF collocation upwinding techniques with $Co = 0.03$. The comparison is made at two different times: t_1=0.1 (sec) and t_2=0.4 (sec).
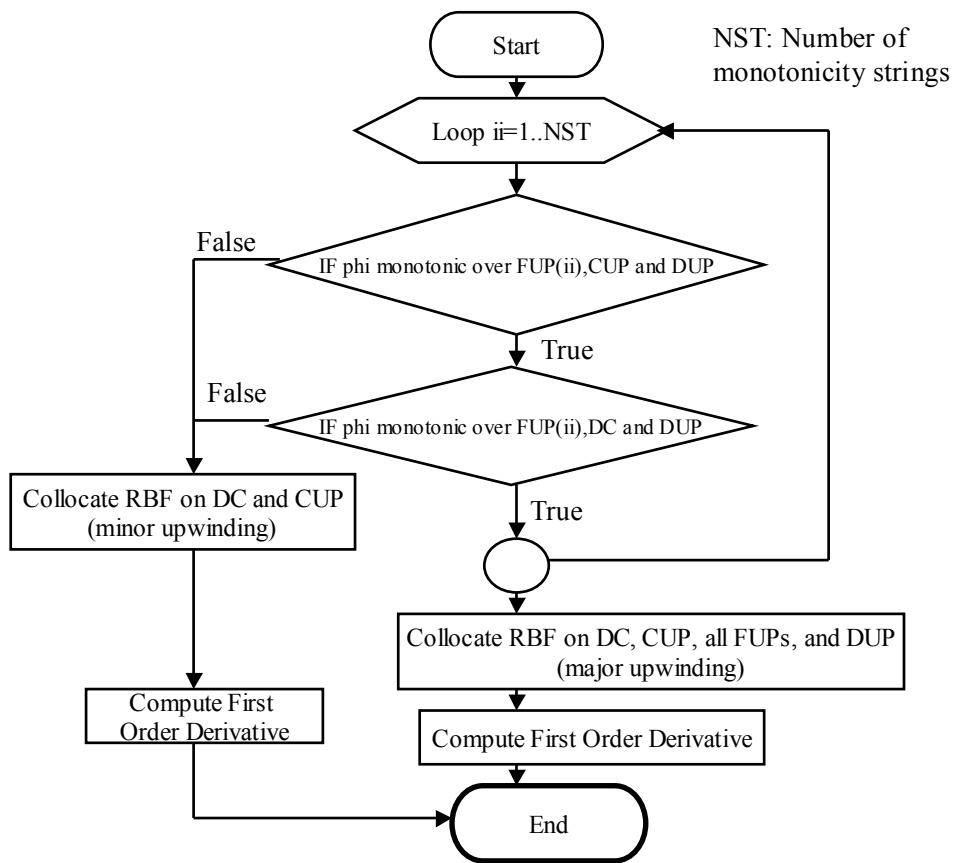
Figure 3.9. The LCMM upwinding/limiter technique algorithm flowchart.
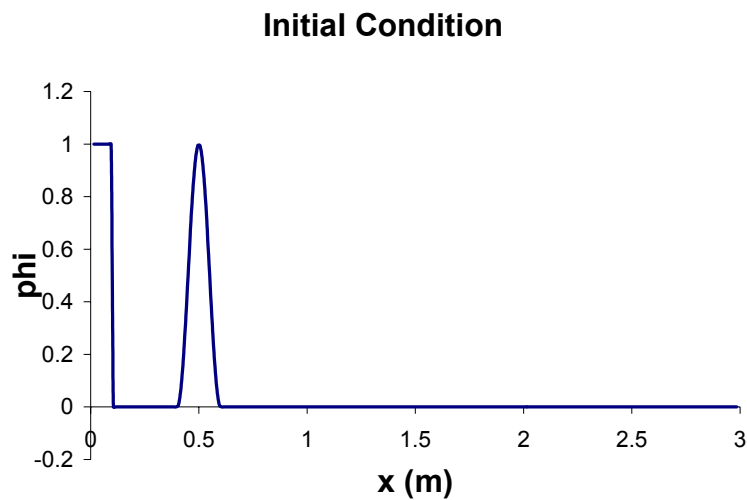
Figure 3.10: The initial condition of the linear wave profile.

Another comparison between the exact solution of the convected signal and the RBF collocation upwinding solutions for $Co = 0.1$ is shown in Figure (3.12) at times: t_1=0.025 (sec) and t_2=0.1 (sec). It is remarkable in Figure 3.11 and Figure (3.12) that the major upwinding is not exhibiting any oscillation thanks to the incorporation of the LCMM limiter strategy by which some dissipation is borrowed from the minor RBF collocation upwinding. The stable yet over-damped solution profile of the minor RBF collocation upwinding is prominent in Figure (3.11) and Figure (3.12), which justifies why the upwinding process should start with a major upwinding and then revert to the minor upwinding should the monotonicity criteria not be satisfied.

As pointed in the discussion of the limiter strategy, the minor upwinding should have an interventional role such that it provides dissipation to the solution just enough to suppress the oscillations. A comparison among the exact solution of the convected signal, the numerical solution obtained by the major RBF collocation upwinding technique, and the numerical solution obtained by the FVM Minmod TVD scheme is illustrated in Figure (3.13) with $Co = 0.03$, t_1=0.1 (sec), and t_2=0.4 (sec). Then, another similar comparison is shown in Figure (3.14) with $Co = 0.03$, t_1=0.025 (sec), and t_2=0.1 (sec). Further comparisons involving the exact solution with numerical solutions from the major RBF collocation upwinding technique and the FVM Muscl TVD scheme are shown in Figure (3.15) and Figure (3.16). According to the results from Figure (3.13) through Figure (3.16), the LCMM limiter-enhanced major upwinding technique seems to be superior to both the Minmod and the Muscl schemes. At both test Courant numbers, the step profile resolution is better preserved by the LCMM major upwinding. Besides, the LCMM major upwinding technique presents less diffusion as illustrated by the squared-sine wave amplitude decay. The superiority of the LCMM major upwinding grants us the confidence of applying this major RBF collocation upwinding technique to more complex transport equations.
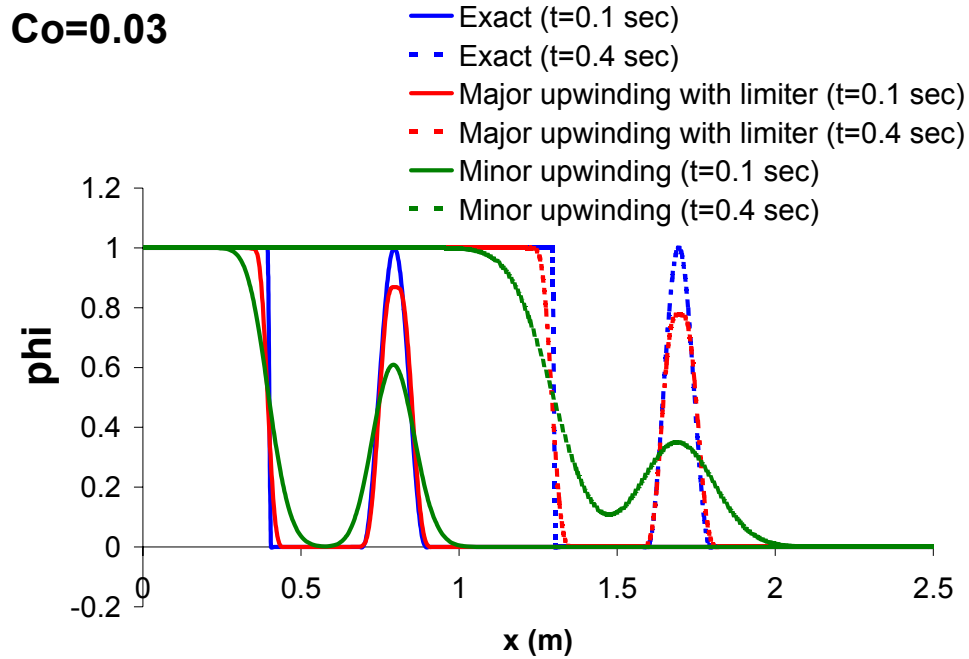
Figure 3.11: The performances of the minor and major RBF collocation upwinding techniques as benchmarked with the exact solution at Co=0.03.
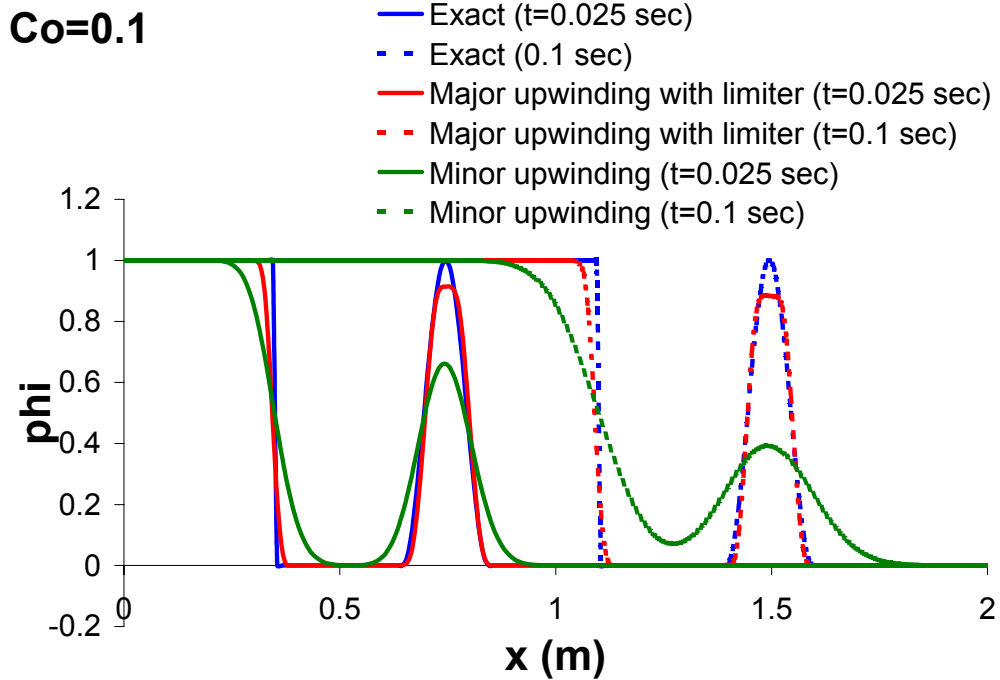
Figure 3.12: The performances of the minor and major RBF collocation upwinding techniques as benchmarked with the exact solution at Co=0.1.
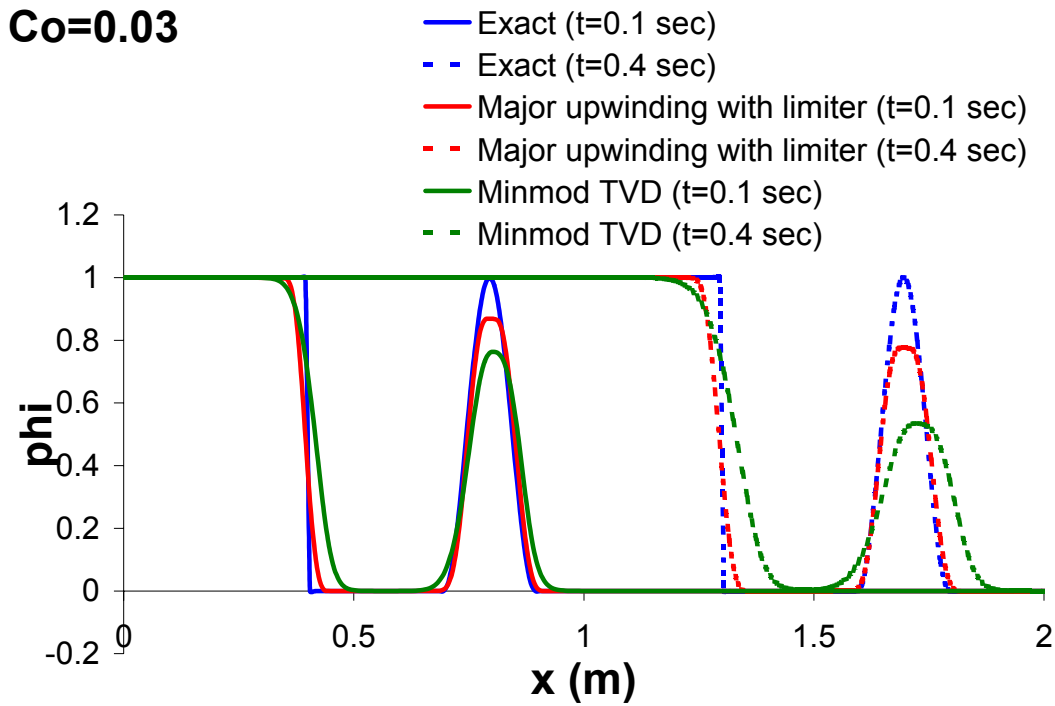
Figure 3.13: The performances of the major RBF collocation upwinding technique and the FVM Minmod TVD scheme as benchmarked with the exact solution at $Co=0.03$.

Figure 3.14: The performances of the major RBF collocation upwinding technique and the FVM Minmod TVD scheme as benchmarked with the exact solution at $Co=0.1$.

Co=0.03

Legend:
- Exact (t=0.1 sec)
- Exact (t=0.4 sec)
- Major upwinding with limiter (t=0.1 sec)
- Major upwinding with limiter (t=0.4 sec)
- Muscl TVD (t=0.1 sec)
- Muscl TVD (t=0.4 sec)

Figure 3.15: The performances of the major RBF collocation upwinding technique and the FVM Muscl TVD scheme as benchmarked with the exact solution at Co=0.03.

Co=0.1

Legend:
- Exact (t=0.025 sec)
- Exact (t=0.1 sec)
- Major upwinding with limiter (t=0.025 sec)
- Major upwinding with limiter (t=0.1 sec)
- Muscl TVD (t=0.025 sec)
- Muscl TVD (t=0.1 sec)
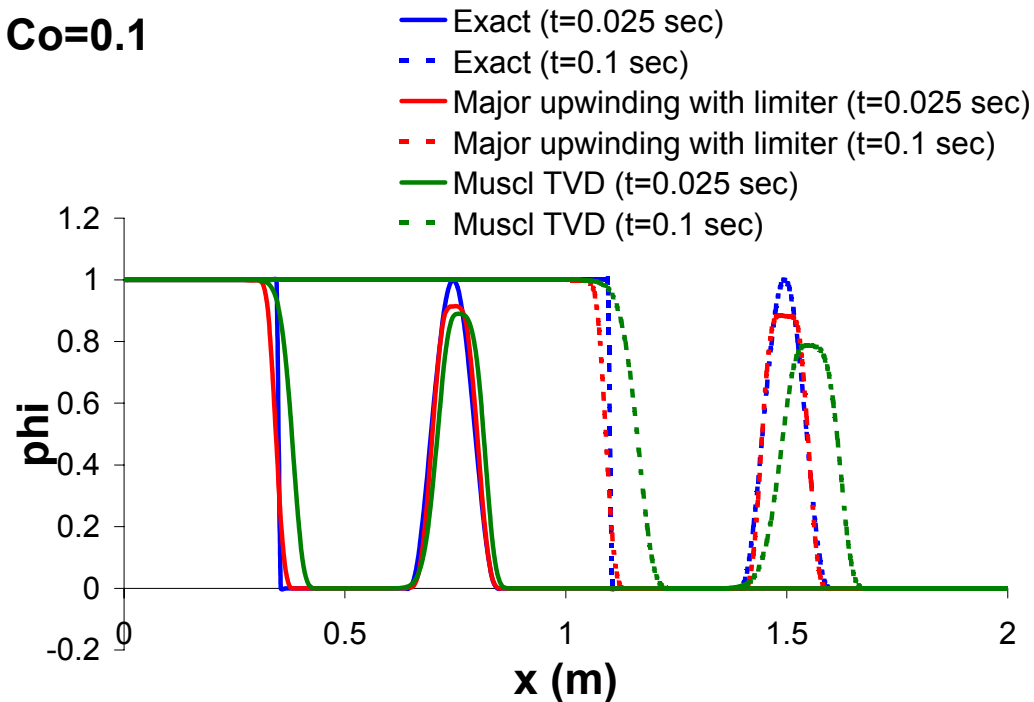
Figure 3.16: The performances of the major RBF collocation upwinding technique and the FVM Muscl TVD scheme as benchmarked with the exact solution at Co=0.1.
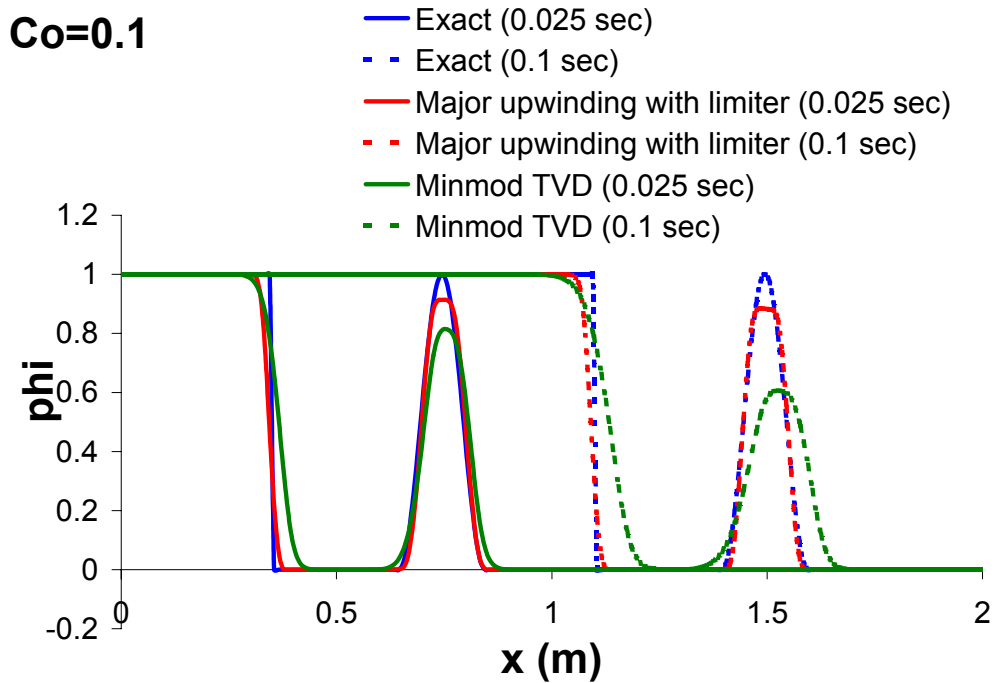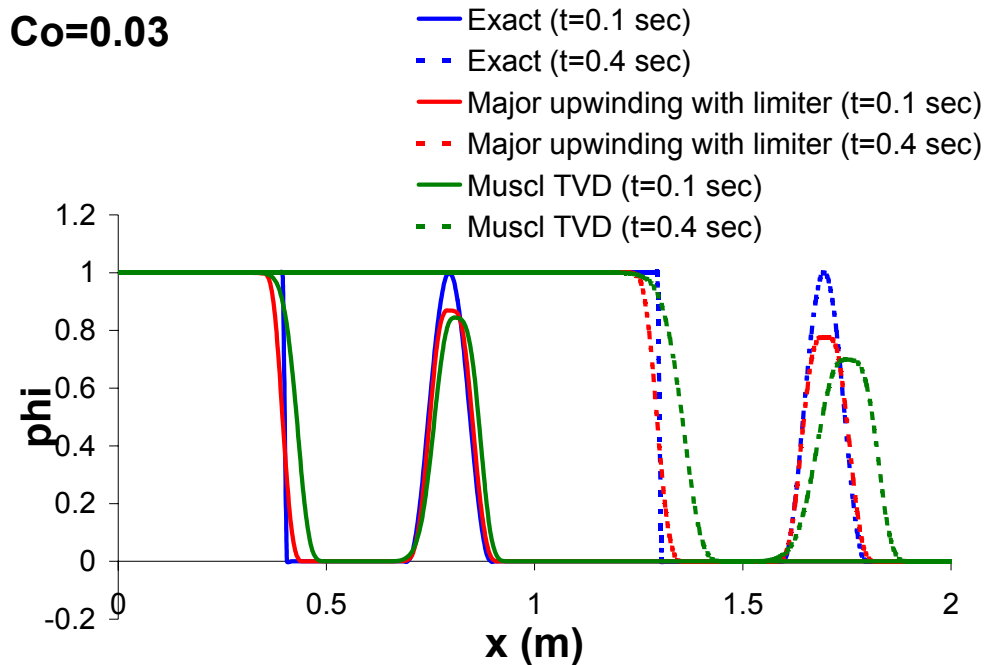
3.4.3 Two-Dimensional (2D) LCMM Upwinding Results

The next step in the validation of the LCMM upwinding technique is to examine the time decay of linear wave profiles propagating on 2D planes. The 2-D linear wave transport equation is

$$\frac{\partial \phi}{\partial t} + a\frac{\partial \phi}{\partial x} + a\frac{\partial \phi}{\partial y} = 0 \tag{3.31}$$

Figure (3.17) reveals the geometry of a 1 (m) x 1 (m) square solution domain where a box-shaped profile for a field variable ϕ is purely convected. The flow enters the square domain from the bottom and the left sides and exits through the top and the right sides. The field variable ϕ takes an inlet value of 1 on the boundary green lines and a value of 2 on the boundary red lines. The convection speed magnitude is 1 (m/sec) and its direction is at a 45° angle with respect to the horizontal x-axis. Figure (3.17) also shows the point distribution. The contour of ϕ for the box-shaped profile convection problem is shown in Figure (3.18). This contour is obtained by the major RBF collocation upwinding technique involving a limiter. Figure (3.18) shows the distribution of ϕ on a vertical line traced at a x=0.5 (m) for the exact solution, the minor RBF collocation upwinding technique, and the major RBF collocation upwinding technique with and without a limiter. Notice the oscillatory behavior of the major upwinding when the limiter is not employed as it is shown in Figure (3.19); those oscillations are suppressed with the limiter.
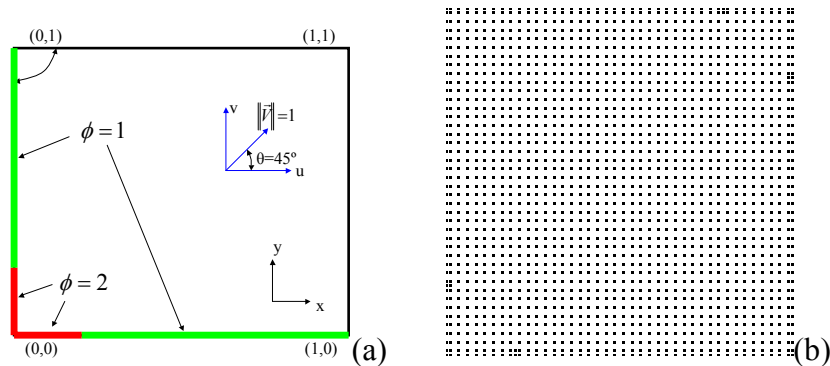
Figure 3.17: The geometry of box profile case (a) and point distribution in the square (b).
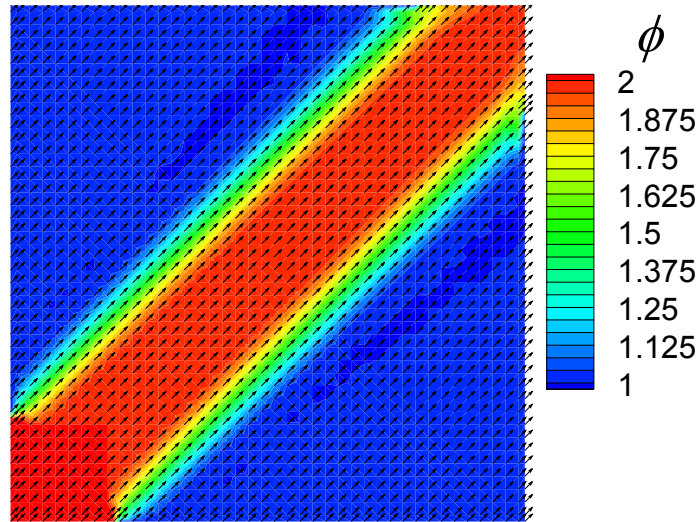
Figure 3.18: The field variable ϕ contour for the inlet box-shaped profile pure convection.
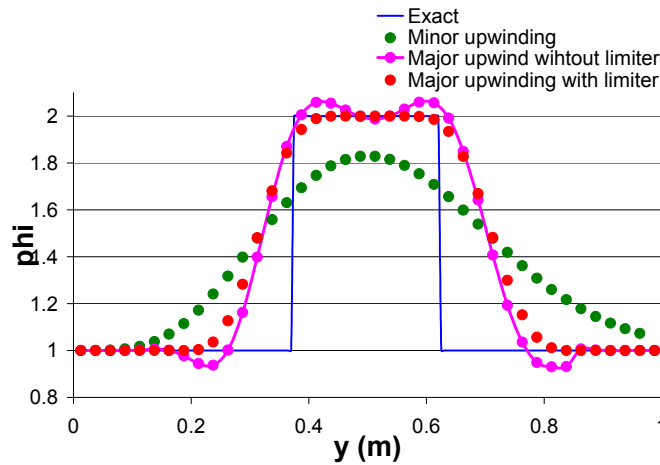
Figure 3.19: The field variable ϕ distribution at x=0.5 (m).

The second example for the 2D validation of the LCMM upwinding technique is a 1 (m) x 1 (m) square geometry that is shown in Figure (3.20). The pure convection of a step profile for a field variable ϕ occurs in the geometry shown Figure (3.20). The flow enters the square domain from the bottom and the left sides and exits through the top and the right sides. Notice that the inlet step profile is situated on the left side of the square. The field variable ϕ takes an inlet value of 1 on the boundary green lines and a value of 2 on the boundary red line. The pure convection is carried out by a flowfield at an angle of θ degrees with respect to the horizontal x-

axis. The magnitude of the velocity field is equal to unity. The point distribution for the geometry in Figure (3.20) is the same as the point distribution shown in (3.17b). The contour of ϕ for the step profile pure convection problem is shown in Figures (3.21), (3.23), and (3.25), for θ angles of 25°, 35°, and 45° respectively. These contour solutions are obtained by the major RBF collocation upwinding technique involving a limiter. Figures (3.22), (3.24), and (3.26) show the distribution of ϕ for the three angle cases (25°, 35° and 45°) on a vertical line traced at a x=0.5 (m) for the exact solution, the minor RBF collocation upwinding technique, and the major RBF collocation upwinding technique with and without a limiter.
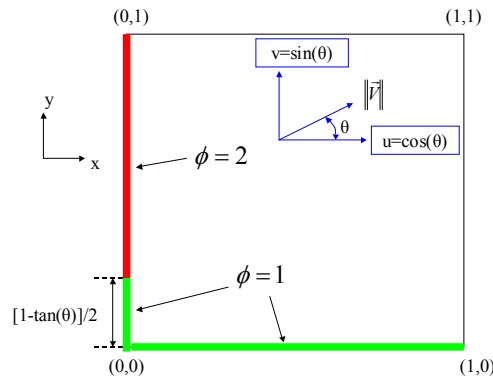
Figure 3.20: The geometry for the step profile inlet pure convection problem.
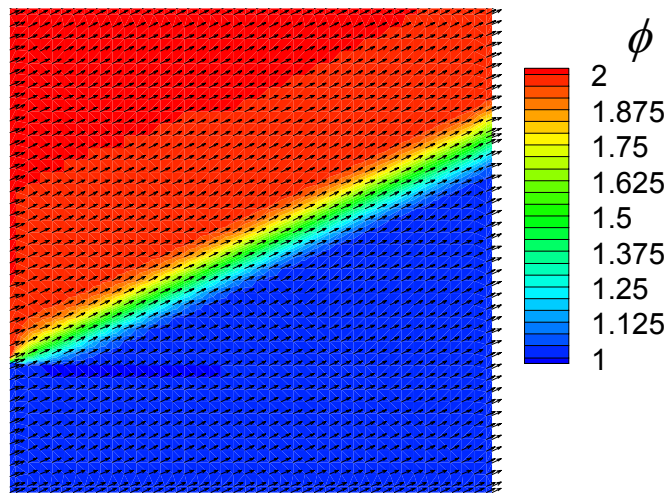
Figure 3.21: The field variable ϕ contour for the inlet step profile pure convection. with θ=25°.
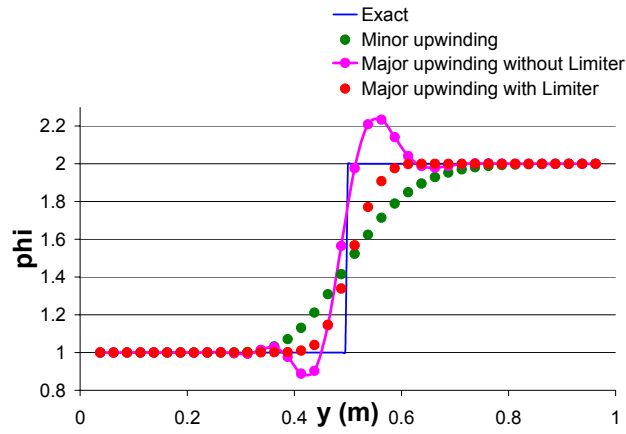
Figure 3.22: The field variable ϕ distribution at x=0.5 (m) for the θ=25° case.
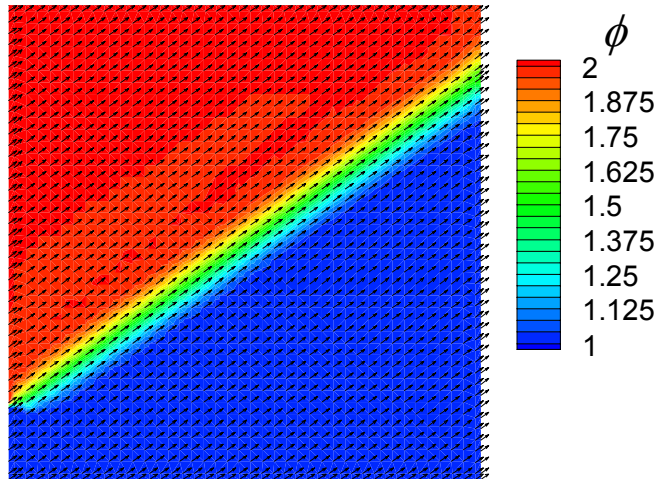
Figure 3.23: The field variable ϕ contour for the inlet step profile pure convection. with θ=35°.
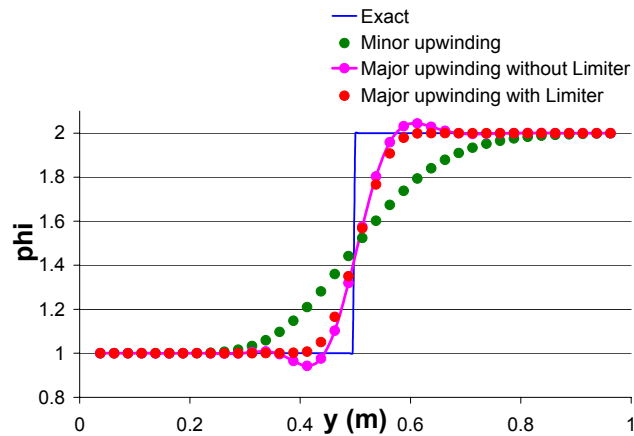
Figure 3.24: The field variable ϕ distribution at x=0.5 (m) for the θ=35° case.
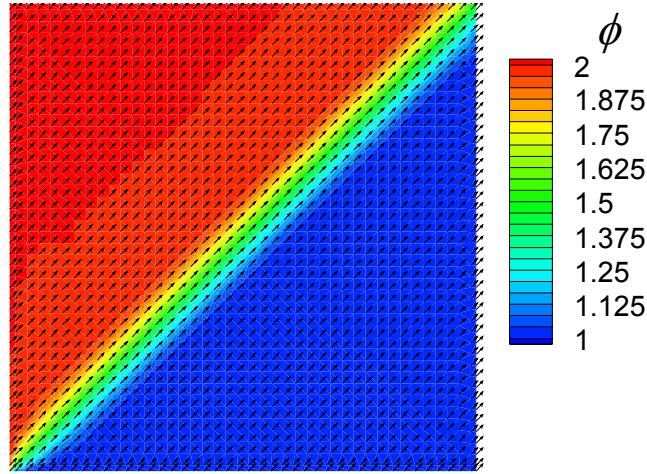
Figure 3.25: The field variable ϕ contour for the inlet step profile pure convection. with $\theta=45°$.
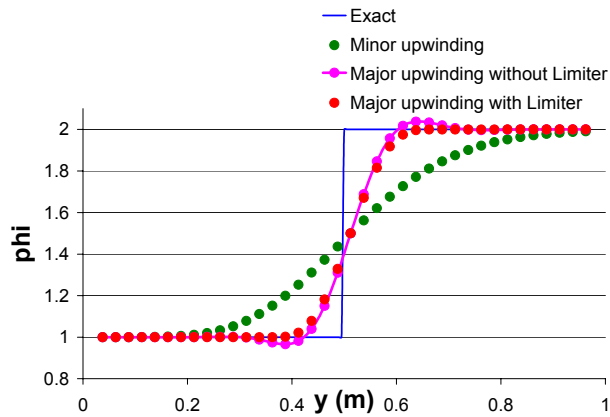
Figure 3.26: The field variable ϕ distribution at x=0.5 (m) for the $\theta=45°$ case.

The third example for the 2D validation of the LCMM upwinding technique is the pure convection of a inlet box-shaped profile of the field variable ϕ. Figure (3.27a) reveals the geometry of a 2 (m) x 1 (m) rectangular solution domain where the pure advection of ϕ occurs. The convection is carried out by a rotational (Smith-Hutton) flowfield which analytical solution is expressed in Equations (3.32) for the horizontal component and (3.33) for the horizontal component.

$$u = 2y[1 - (x-1)^2] \tag{3.32}$$

$$v = -2(x-1)[1 - y^2] \tag{3.33}$$

The flow enters the rectangular domain from the bottom left side and after performing a 180 rotation exits through the bottom right side. The field variable ϕ takes an inlet value of 0 on the boundary green lines and a value of 2 on the boundary red line. Figure (3.27b) shows the point distribution in the rectangular geometry. The contour of ϕ for this rotational convection problem is shown in Figure (3.28). This contour solution is obtained by the major RBF collocation upwinding technique involving a limiter. Figure (3.29) reveals the distribution of ϕ at the outlet of the current rectangular solution domain as computed through the exact solution, the minor RBF collocation upwinding technique, and the major RBF collocation upwinding technique with and without a limiter.
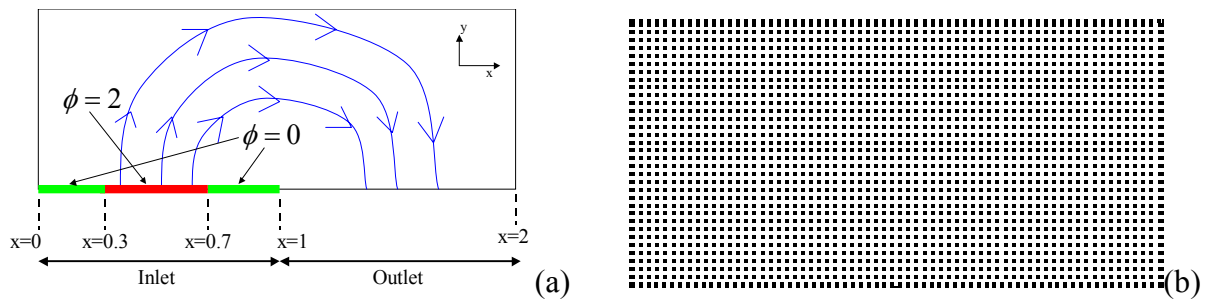

Figure 3.27: The geometry (a) and point distribution (b) for the rotational pure convection problem.
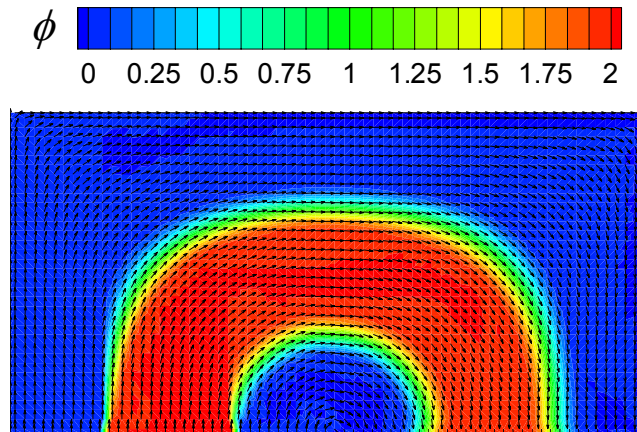
Figure 3.28: The field variable ϕ contour for the pure rotational convection problem.
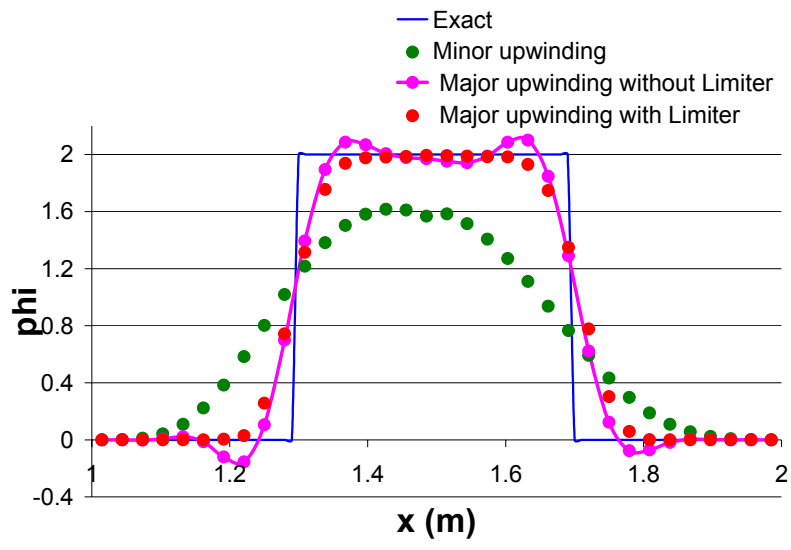
Figure 3.29: The field variable ϕ distribution at the outlet of the rectangular geometry involving the rotational flowfield.

CHAPTER 4: THE LCMM APPLICATION TO INCOMPRESSIBLE FLOWS

In this chapter, the LCMM features are incorporated in an explicit solution scheme to the incompressible laminar Navier-Stokes (N-S) equations. The solution scheme chosen for the N-S equations is the "velocity correction" scheme originally proposed by Harlow and Welch [91]. The method is closely related to the alternative pressure correction scheme of Patankar [92]. It is noted that the energy equation is ignored as no thermal analyses will be conducted. In fact, the current dissertation deals with modeling the blood flow, which is normally treated as isothermal. The velocity correction scheme N-S solution requires evaluating derivatives for various field variables. The LCMM localized formulations will be utilized to build vectors for those derivatives whether by the standard RBF collocation, the RBF collocation upwinding, or the MLS-based polynomial expansion.

The present chapter commences with a section detailing a complete formulation for the velocity correction scheme. Also in the first section, there is an explanation on how the standard RBF collocation, the RBF collocation upwinding, and MLS-based polynomial expansion localized formulations are appropriately assigned to the derivative terms in the velocity correction scheme. The second section entails an error analysis to estimate the accuracy of the LCMM in its application to the N-S equations. Also, the second section presents validation results for the LCMM involving steady and pulsatile laminar incompressible flow examples in both 2D and 3D geometries. The validation of the LCMM results will be conducted against numerical results obtained by the well-established FVM software "FLUENT 6.2" (Fluent Inc., Lebanon, NH). The validation is a mandatory step before generalizing the LCMM. In the third section of this chapter, the N-S equations will be re-formulated in a manner that accounts for non-Newtonian effects. The inclusion of a non-Newtonian model is necessary for the simulation

of the blood rheology. Validation results will be also presented for the LCMM with the non-Newtonian model employed.

4.1 The Navier-Stokes LCMM Solution

4.1.1 The Velocity Correction Scheme

An incompressible isothermal flow under laminar conditions is governed by the N-S equations comprising of both the continuity and linear momentum equations. The continuity equation for an incompressible flow is shown in Equation (4.1). Neglecting the fluid body forces, the linear momentum equation is written in a non-conservative form as in Equation (4.2).

$$\nabla \cdot \vec{V} = 0 \tag{4.1}$$

$$\rho \frac{\partial \vec{V}}{\partial t} + \rho \left(\vec{V} \cdot \nabla \right) \vec{V} = -\nabla p + \nabla \cdot \overrightarrow{\overrightarrow{\tau}} \tag{4.2}$$

Here, $\vec{V}$ is the flow velocity vector, ρ is the bulk density of the flow, p is the field pressure, μ is the fluid dynamic viscosity, and $\overrightarrow{\overrightarrow{\tau}}$ is the viscous stress tensor. If the fluid is Newtonian, $\nabla \overrightarrow{\overrightarrow{\tau}}$ can be proven to be equal to $\mu \nabla^2 \vec{V}$ by means of the zero divergence in Equation 4.1. Then, Equation (4.2) can be written as,

$$\rho \frac{\partial \vec{V}}{\partial t} + \rho \left(\vec{V} \cdot \nabla \right) \vec{V} = -\nabla p + \mu \nabla^2 \vec{V} \tag{4.3}$$

All field variables are functions of space $(\boldsymbol{x}, \boldsymbol{y}, \boldsymbol{z})$ and time (t). We now review the velocity correction scheme of Harlow and Welch [91]. Upon establishing a divergence-free initial velocity field, a new velocity field $\vec{V}^{(*)}$ may be estimated from the Navier-Stokes equations. This procedure starts by positioning the convective term $\rho \left(\vec{V} \cdot \nabla \right) \vec{V}$ on the right hand side (RHS) of Equation (4.3) along with the pressure gradient term ∇p and the diffusive term $\mu \nabla^2 \vec{V}$. Then all

the terms on the RHS are lagged to previous time k as expressed in Equation (4.4).

$$\rho\frac{\partial \vec{V}^{(*)}}{\partial t} = \mu\nabla^2\vec{V}^{(k)} - \nabla p^{(k)} - \rho\left(\vec{V}^{(k)} \cdot \nabla\right)\vec{V}^{(k)} \tag{4.4}$$

Equation (4.4) can be advanced in time using a third-order backward-difference time stepping method that is expressed in Equation (4.5). Here, the explicit contribution of the velocity derivatives is made semi-implicit. The purpose of the time stepping method is to reduce the error introduced by the explicit formulation of the N-S equations.

$$\vec{V}^{(k+1/3)} = \vec{V}^{(k)} + \frac{\Delta t}{3\rho}[-\nabla p]^{(k)} + \frac{\Delta t}{3\rho}\left[\mu\nabla^2\vec{V} - \rho\left(\vec{V}\cdot\nabla\right)\vec{V}\right]^{(k)} \tag{4.5}$$

$$\vec{V}^{(k+1/2)} = \vec{V}^{(k)} + \frac{\Delta t}{2\rho}[-\nabla p]^{(k)} + \frac{\Delta t}{2\rho}\left[\mu\nabla^2\vec{V} - \rho\left(\vec{V}\cdot\nabla\right)\vec{V}\right]^{(k+1/3)}$$

$$\vec{V}^{(*)} = \vec{V}^{(k)} + \frac{\Delta t}{\rho}[-\nabla p]^{(k)} + \frac{\Delta t}{\rho}\left[\mu\nabla^2\vec{V} - \rho\left(\vec{V}\cdot\nabla\right)\vec{V}\right]^{(k+1/2)}$$

The boundary values of the new velocity field $\vec{V}^{(*)}$ is typically zero at the walls (no-slip condition due to the fluid viscosity) and has a prescribed value at the inlets. For the outlets a non-reflective boundary condition is applied. The generalized form of the non-reflective boundary condition is given in Equation (4.6).

$$\frac{\partial \vec{V}^{(*)}}{\partial t} + V_n\frac{\partial \vec{V}^{(*)}}{\partial n} = 0 \tag{4.6}$$

In Equation (4.6), V_n is the normal velocity, and $\partial/\partial n$ denotes derivative with respect to the outward-drawn normal to a boundary, $\vec{n}$.

The solution of Equation (4.4) with the appropriate boundary conditions provides a velocity field that does not satisfy the continuity equation, that is, $\nabla \cdot \vec{V}^{(*)} \neq 0$. Thus, in order to satisfy continuity the velocity field $\vec{V}^{(*)}$ should be corrected with a velocity correction field $\delta\vec{V}^{(k+1)}$ as expressed in Equation (4.7).

$$\vec{V}^{(k+1)} = \vec{V}^{(*)} + \delta\vec{V}^{(k+1)} \tag{4.7}$$

Furthermore, if the velocity correction is required to be irrotational, $\nabla \times \delta \vec{V}^{(k+1)} = 0$, then a Helmholtz potential $\phi^{(k+1)}$ can be expressed as shown in Equation (4.8).

$$\nabla \phi^{(k+1)} = -\delta \vec{V}^{(k+1)} \tag{4.8}$$

Requiring the new velocity field to satisfy continuity, that is, $\nabla \cdot \vec{V}^{(k+1)} = 0$, leads to the Poisson equation given in Equation (4.9).

$$\nabla^2 \phi^{(k+1)} = \left(\nabla \cdot \vec{V}^{(*)} \right) \tag{4.9}$$

The Helmholtz potential Poisson problem in Equation (4.9) is solved subject to a homogeneous second-kind (Neumann) boundary condition at the inlets and walls expressed in Equation (4.13) and a homogeneous first-kind (Dirichlet) boundary condition at outlets expressed in Equation (4.14).

$$\frac{\partial \phi}{\partial n} = 0 \tag{4.10}$$

$$\phi = 0 \tag{4.11}$$

Once Equation (4.9) is solved subject to the appropriate boundary conditions, the velocity field is updated according to Equation (4.7) and it becomes divergence-free.

After correcting the velocity field, the pressure field may be retrieved by taking the divergence of the linear momentum equation given in Equation (4.3). This divergence leads to a pressure Poisson problem expressed in Equation (4.12).

$$\nabla^2 p^{(k+1)} = -\rho \nabla \cdot \left[\left(\vec{V}^{(k+1)} \cdot \nabla \right) \vec{V}^{(k+1)} \right] \tag{4.12}$$

The Pressure Poisson problem in Equation (4.12) is solved subject to a non-homogeneous second-kind (Neumann) boundary condition at the inlets and walls expressed in Equation (4.13) and a non-homogeneous first-kind (Dirichlet) boundary condition at outlets expressed in Equation (4.14).

$$\frac{\partial p}{\partial n} = \widehat{\varkappa} \tag{4.13}$$

$$p = \widehat{p} \tag{4.14}$$

The value of $\widehat{\varkappa}$ in Equation (4.13) is approximated at every boundary point by a simple finite differencing between the pressure values at this boundary point and the pressure value at the corresponding shadow point.

4.1.2 Assignment of the Derivative Vectors

The next step is to explain how the various derivatives, needed in the velocity correction scheme, are treated by LCMM localized formulation. Recall that the LCMM localized formulation may conduce to three classes of derivative vectors; the first class is obtained by the standard RBF collocation, the second one by the RBF collocation upwinding, and the third one by the MLS-based polynomial expansion.

Generally, the MLS-based polynomial expansion technique is used to build vectors for all the first-order derivatives in the velocity correction scheme except for the ones in the linear momentum convective terms that require an in-depth examination. As such, the derivative terms which vectors are built by the MLS-based polynomial expansion technique are ∇p in Equation (4.3), $\nabla \phi$ in Equation (4.8), $\nabla \cdot \overrightarrow{V}^{(*)}$ in Equation (4.9), and $\nabla \cdot \left[\left(\overrightarrow{V} \cdot \nabla \right) \overrightarrow{V} \right]$ in Equation (4.12). The standard RBF collocation may be also used to build vectors for the first-order derivatives, but with less stability.

The most sensitive term that has to be treated with care is the convective term $\rho \left(\overrightarrow{V} \cdot \nabla \right) \overrightarrow{V}$ shown in Equation (4.3). If this term is not treated properly, then it will result in unbounded oscillations. In a 3D environment, the convective term can be further expressed as $\rho \left(u \frac{\partial u}{\partial x} + v \frac{\partial u}{\partial y} + w \frac{\partial u}{\partial z} \right)$ for the x-linear momentum equation, as $\rho \left(u \frac{\partial v}{\partial x} + v \frac{\partial v}{\partial y} + w \frac{\partial v}{\partial z} \right)$ for the y-

linear momentum equation, and as $\rho\left(u\frac{\partial w}{\partial x} + v\frac{\partial w}{\partial y} + w\frac{\partial w}{\partial z}\right)$ for the z-linear momentum equation. Here u, v, and w are the x-component, the y-component, and the z-component of the velocity vector $\vec{V}$. The criticality of the convective term depends on the local Reynolds numbers Re_x, Re_y and Re_z which expressions are given in Equation (4.15), Equation (4.16) and Equation (4.17) respectively. Re_x, Re_y and Re_z are referred as the upwinding Reynolds numbers in the appropriate directions. δ is an average finite distance between the data center and all its neighboring influence points in the standard topology. Recall that the Reynolds number is the ratio of the flow convective or inertia forces to the viscous forces.

$$Re_x = \rho\|u\|\delta/\mu \tag{4.15}$$

$$Re_y = \rho\|v\|\delta/\mu \tag{4.16}$$

$$Re_z = \rho\|w\|\delta/\mu \tag{4.17}$$

If Re_x has a value less than 1, then the $u\frac{\partial u}{\partial x}$, $u\frac{\partial v}{\partial x}$ and $u\frac{\partial w}{\partial x}$ convective terms are not critical and the derivative vectors for $\frac{\partial u}{\partial x}$, $\frac{\partial v}{\partial x}$ and $\frac{\partial w}{\partial x}$ may be built following a MLS-based polynomial expansion technique. Conversely, If Re_x has a value greater or equal to 1, then the $u\frac{\partial u}{\partial x}$, $u\frac{\partial v}{\partial x}$ and $u\frac{\partial w}{\partial x}$ convective terms become critical and the derivative vectors for $\frac{\partial u}{\partial x}$, $\frac{\partial v}{\partial x}$ and $\frac{\partial w}{\partial x}$ must be built following a RBF collocation upwinding technique. Likewise to the first-order convective derivatives in the x-direction, the criticality of the first-order convective derivatives in the y-direction and the z-direction can be assessed based on the values of Re_y and Re_z, and the derivative vectors are then built accordingly.

Regarding the Laplacian derivatives in the velocity correction scheme, the standard RBF collocation is used to build their vectors. Hence, the derivative vectors for all of $\nabla^2\vec{V}$ in Equation (4.2), $\nabla^2\phi$ in Equation (4.9), and $\nabla^2 p$ in Equation (4.12) are built following the standard RBF collocation.

4.2 The LCMM Incompressible Flow Examples

Since the LCMM is a relatively newcomer to computational fluid dynamics modeling, error analyses and solution benchmarking need to be performed for this method. In this section, the decaying vortex analytical solution is used to study the spatial accuracy of the LCMM. Then, we benchmark the LCMM results with numerical results produced by the FVM solver FLUENT 6.2. These validations are done for incompressible laminar flows as modeled by the LCMM and the FVM in identical geometries and subject to the same boundary conditions. It is critical for the shape optimization approach of the current research to have the LCMM produces accurate results for any general case. Additionally, the LCMM capability is tested on highly irregular geometries.

4.2.1 Spatial Accuracy

The decaying vortex problem is used to test the spatial accuracy of the LCMM over a 2D domain bounded whereby $x \in [-0.5, 0.5]$ and $y \in [-0.5, 0.5]$. This test problem for incompressible flows have been used by many [61,93,94] as a standard for spatial error analysis. The velocity and pressure exact solutions of the decaying vortex problem are provided in terms of space (x, y) and time (t) as shown in Equation (4.18).

$$
\begin{aligned}
u_{exact} &= -cos(\pi x)sin(\pi y)e^{-2\pi^2 t/Re} \\
v_{exact} &= sin(\pi x)cos(\pi y)e^{-2\pi^2 t/Re} \\
p_{exact} &= -\frac{1}{4}[cos(2\pi x) + cos(2\pi y)]e^{-4\pi^2 t/Re}
\end{aligned}
\tag{4.18}
$$

Re is a reference Reynolds number that is equal to $\rho U L/\mu$, where U is the maximum velocity at $t = 0$ and L is the maximum vortex size. Given the current square domain, both U and L will be equal to 1. Then by choosing $\rho = 1$ and $\mu = 0.1$, Re will be equal to 10. In order to determine

the spatial accuracy, the square domain will be discretized by four different point distribution densities such as follows: $N_1 = 444$, $N_2 = 968$, $N_3 = 1740$, and $N_4 = 2664$. For all the point distribution density cases, a constant time step of 10^{-4} (sec) is used to render the current error analysis time-step-independent. As a benchmark, Figure (4.1) shows the velocity and pressure contours of the decaying vortex at $t = 0.2$ (sec). Then, Figure (4.2) reveals the velocity contours and vectors of the decaying vortex at $t = 0.2$ (sec) for the four point distribution density cases as determined by the LCMM. An excellent agreement between the analytical and LCMM x-velocity solutions is indeed demonstrated by the results in Figures (4.1a) and (4.2). Subsequently, Figure 4.3 unveils the pressure contours featuring the automated point distributions at $t = 0.2$ (sec) for all the point density cases, again as computed by the LCMM. At a glance, the pressure solution trends for all the cases in Figure (4.3) follow the analytical solution trend shown in (4.1b). In numbers, the pressure drops in the four cases are: 0.39 (Pa) for the $N_4 = 2664$ case, 0.38 (Pa) for the $N_3 = 1740$ case, 0.37 (Pa) for the $N_2 = 968$ case, and 0.34 (Pa) for the $N_1 = 444$ case. Compared to the analytical case pressure drop of 0.4 (Pa), the case with the most dense point distribution exhibits the best spatial accuracy. Nonetheless, the pressure drop is just a rough accuracy estimate; a more detailed analysis should be performed to exactly evaluate the order of spatial accuracy whether for the LCMM upwinding scheme or the velocity correction scheme. The spatial accuracy of the LCMM upwinding scheme can be determined by examining either the x-velocity or y-velocity errors. The spatial accuracy of the LCMM velocity correction scheme can be determined by examining the pressure. As such, a formal numerical error norm $\|e\|$ is defined as the average of the absolute errors between the exact and the LCMM solutions at each point in the domain, i.e.

$$\|e\| = \frac{\sum\limits_{k=1}^{N} |Solution_{k,exact} - Solution_{k,LCMM}|}{N}.$$

Besides, for a given point distribution density N over the square of area A, an average point spacing spc can be determined such as $spc = \sqrt{A/N}$. The spatial accuracy is determined

by linearly curve-fitting the Log_{10} of the error norm in terms of the Log_{10} of the average point spacing. Figure 4.4 shows a Log_{10} distribution of the x-velocity numerical error in terms of the average point spacing. As well, Figure (4.5) shows a Log_{10} distribution of the pressure numerical error. The distribution of the x-velocity error proves that the LCMM upwinding scheme is third-order accurate, whereas the pressure error distribution suggests that the velocity correction scheme is second-order accurate.

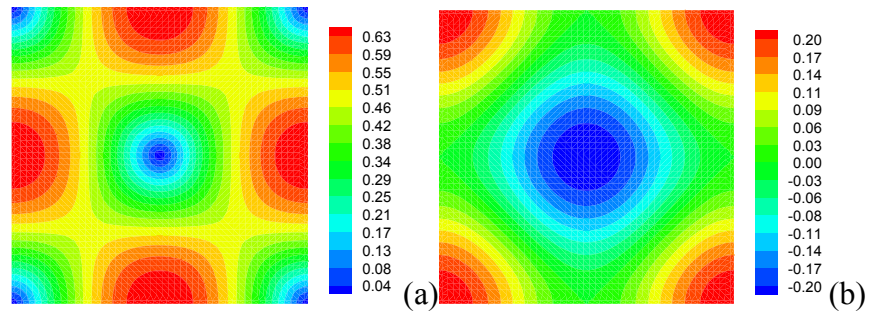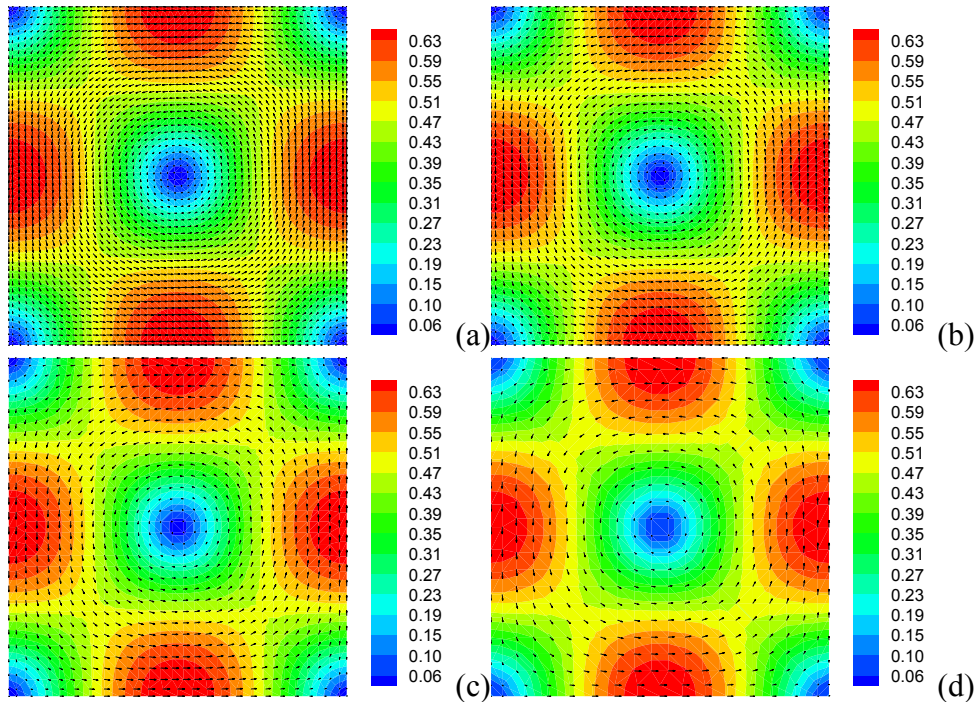Figure 4.1: The decaying vortex velocity (a) and pressure (b) analytical solutions.

Figure 4.2: The decaying vortex velocity LCMM solutions with 2664(a), 1740(b), 968(c), and 444(d) point distribution density cases.
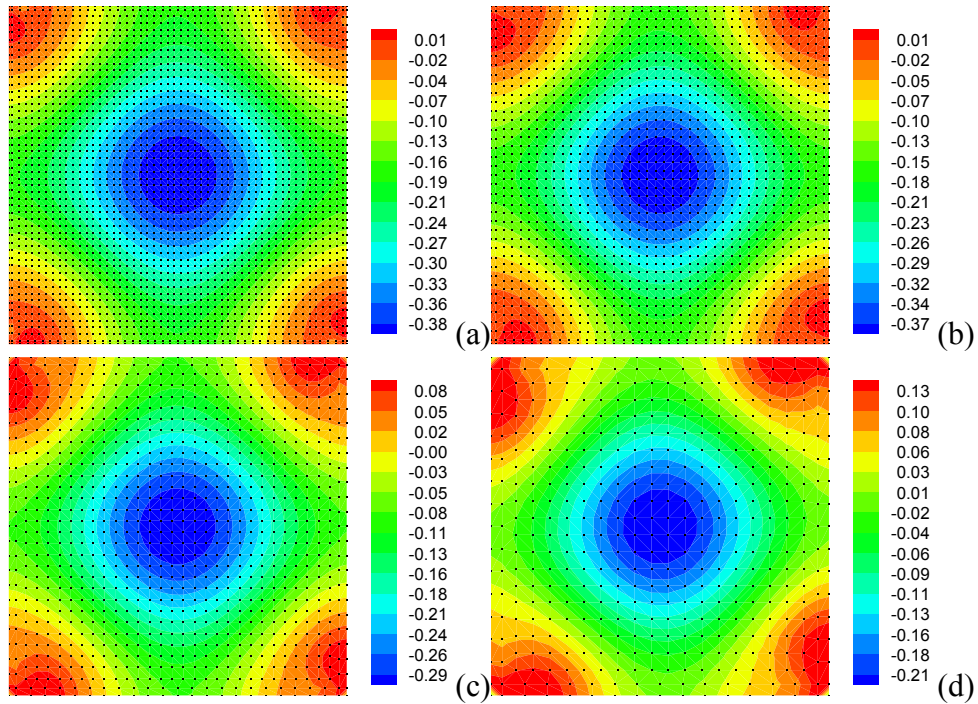
Figure 4.3: The decaying vortex pressure LCMM solutions with 2664(a), 1740(b), 968(c), and 444(d) point distribution density cases.

y = 3.0174x + 1.1505
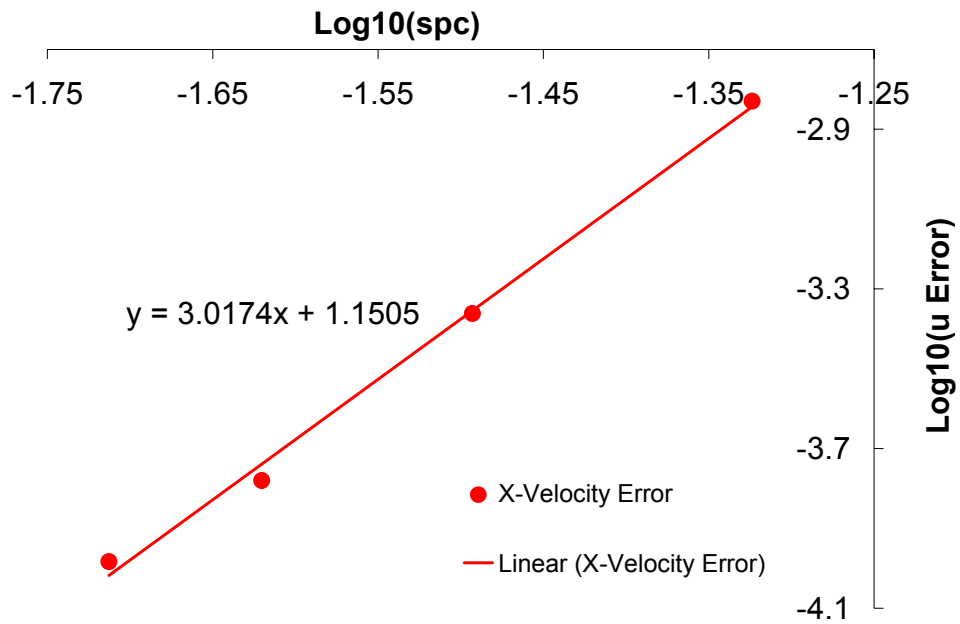
Figure 4.4: The linear curve-fit of the x-velocity error.
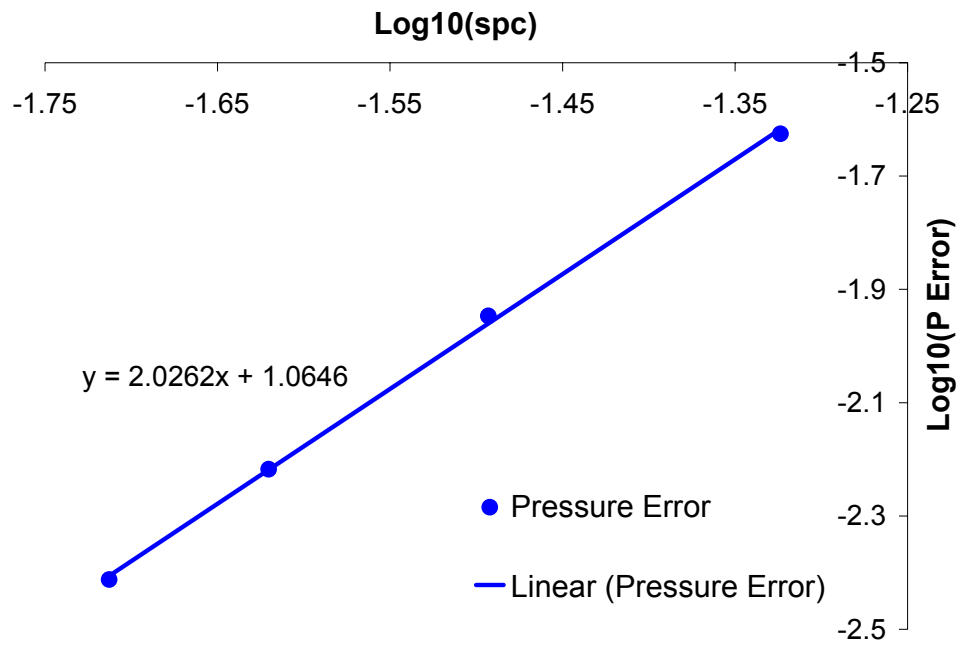
Figure 4.5: The linear curve-fit of the pressure error.

4.2.2 Steady Flow Validation

Three standard ETSDA model geometries are selected for the steady flow validation: the conventional model shown in Figure (4.6), the Miller Cuff model shown in Figure (4.7), and the hood model shown in Figure (4.8). For now, the steady flow is simulated with a constant Newtonian viscosity and a Reynolds number of 450 based on the bypass graft diameter. The blood density and dynamic viscosity are taken to be equal to 1060 (kg/m^3) and 0.004 $(N \cdot s/m^2)$ respectively. The bypass graft diameter is specified as 6 (mm) for all the three anastomotic models. The host artery diameter is equal to 4 (mm), which is within the diameter range of the popliteal artery (at the knee level) where bypass surgeries with synthetic grafts are usually performed. For both the conventional and Miller Cuff models, the anastomotic angle is chosen to be 45°. Besides, for the Miller Cuff model, the cuff height is chosen to be 3 (mm). For the hood

ETSDA model, the geometry of the hood consists of a cubic spline that is defined by four control points c_g, c_1, c_2, and c_a. Besides, the artery cut length (CL) is taken as 1.5 (mm) (CL is the horizontal distance between the heel location and the toe location). For all the ETSDA models, we assume that there is no proximal flow due to a complete blockage of the host artery at the proximal side.

Figure 4.6: The schematic of the conventional ETSDA geometry.

Figure 4.7: The schematic of the Miller Cuff ETSDA geometry.

Figure 4.8: The schematic of the hood ETSDA geometry.

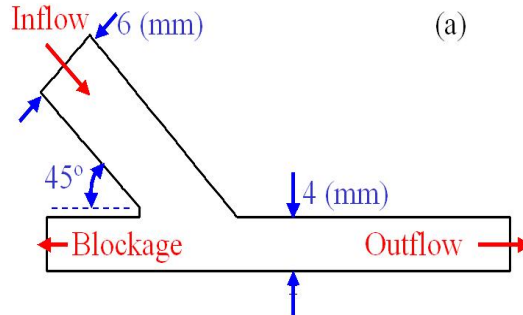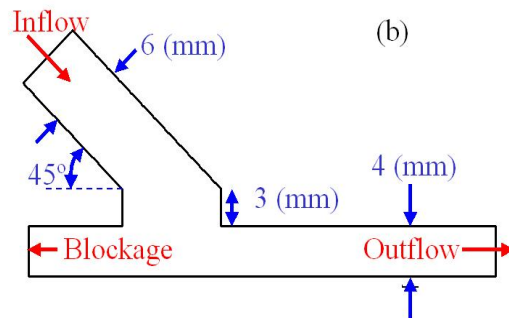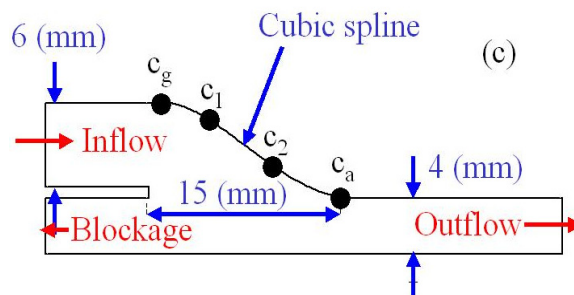Figure (4.9) through Figure (4.11) show the automated point distributions for the conventional, Miller Cuff, and hood ETSDA models respectively. Besides, Figure (4.12) through Figure (4.14) show the FVM mesh for the conventional, Miller Cuff, and hood ETSDA models respectively. The benchmarking of the LCMM is conducted based on three entities: the velocity magnitude, the x-velocity in the anastomosis vicinity, and the wall shear stress (WSS) on the floor of the host artery. It is important to ensure that the WSS meshless results on the host artery floor are accurate since the ETSDA shape optimization will depend on the WSS spatial and temporal gradients thereat.

The velocity magnitude comparison is provided in Figures (4.15), (4.16), and (4.17) for the conventional, Miller Cuff, and hood ETSDA models respectively as obtained by both the LCMM and the FVM solvers. The velocity magnitude contours of the three ETSDA models demonstrate a very good qualitative agreement between the values predicted by the FVM and the localized meshless solvers. Particularly, the meshless method is capable of capturing the flow recirculation at the floor of the host artery consistently with the FVM. Moreover, the flow acceleration as it emerges from the graft to the artery as predicted by the LCMM solver agrees well with the FVM solution.

To quantitatively validate the accuracy of the meshless method, we plot the meshless and FVM x-velocity profiles at five vertical sections (X1, X2, X3, X4, and X5) across the anastomoses of the three given ETSDA models. The locations of the velocity profiles for the three given ETSDA models are revealed in Figure (4.18) through Figure (4.20). The x-velocity profiles results are shown for the conventional ETSDA model, Miller Cuff ETSDA model, and the hood ETSDA model in Figures (4.21), (4.22), and (4.23) respectively. Although minor discrepancies are evident, the velocity profiles indicate a high level of quantitative agreement between the meshless method. and the FVM.
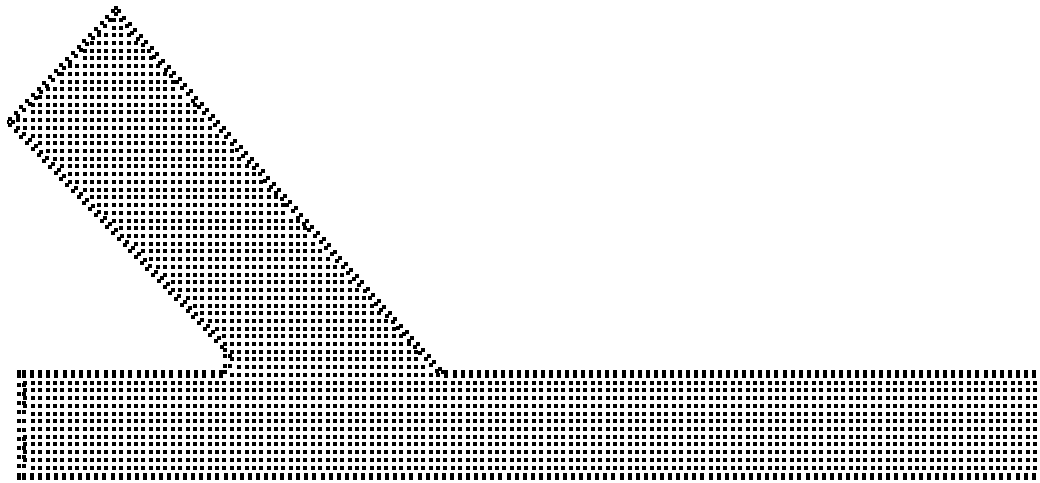
Figure 4.9: The automated point distribution in the conventional ETSDA geometry.
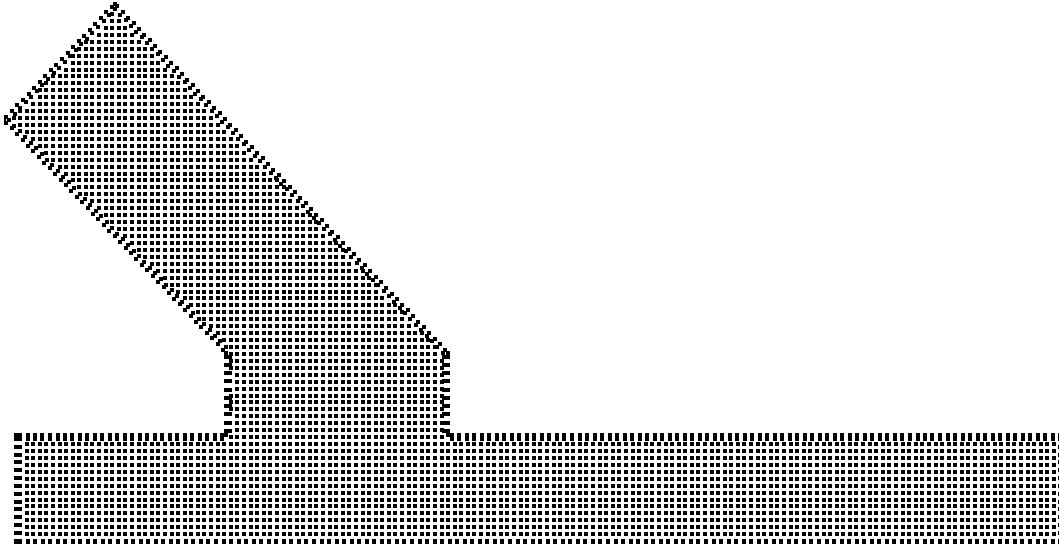
Figure 4.10: The automated point distribution in the Miller Cuff ETSDA geometry.
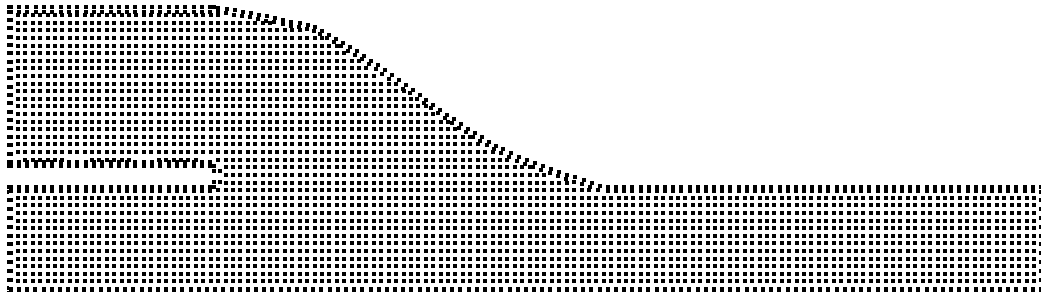
Figure 4.11: The automated point distribution in the hood ETSDA geometry.
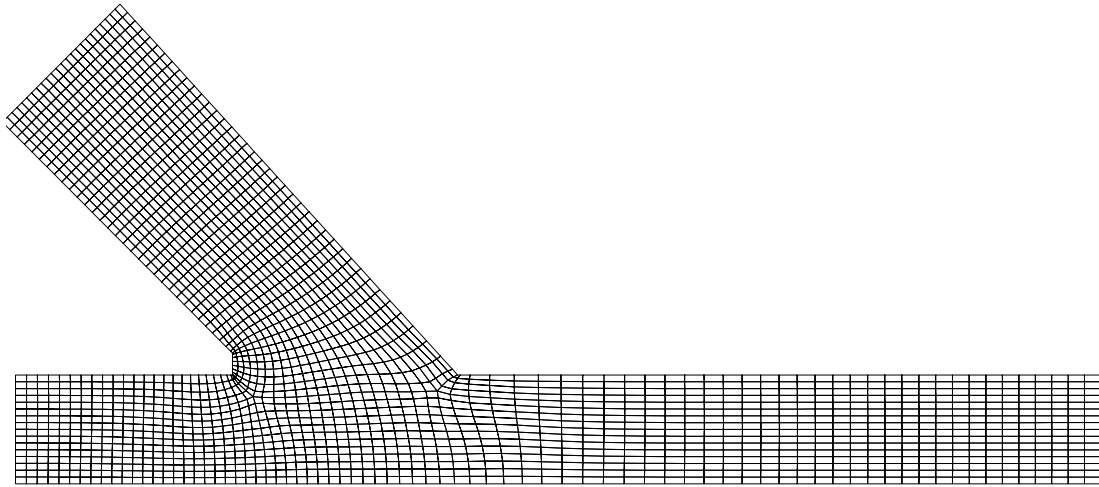
Figure 4.12: The FVM mesh in the conventional ETSDA geometry.
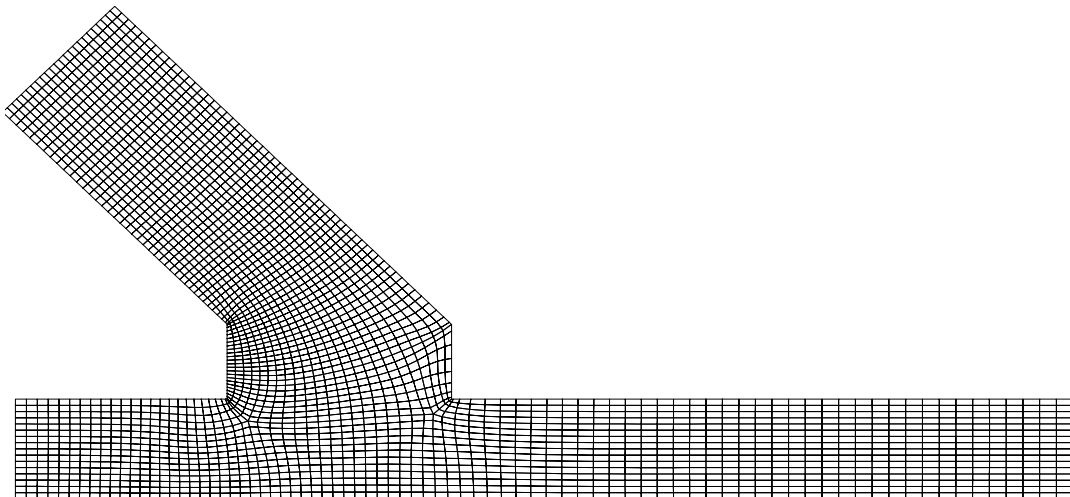
Figure 4.13: The FVM mesh in the Miller Cuff ETSDA geometry.
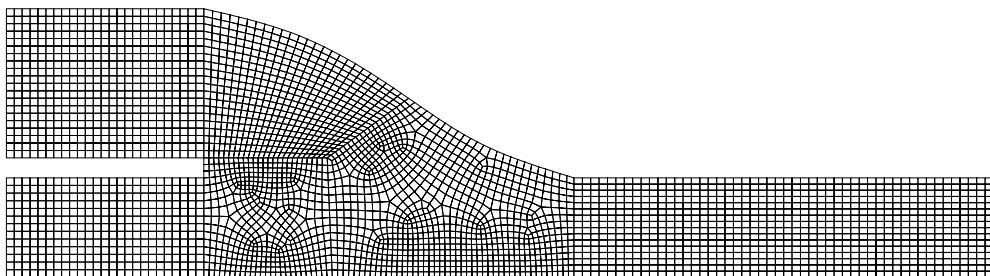
Figure 4.14: The FVM mesh in the hood ETSDA geometry.
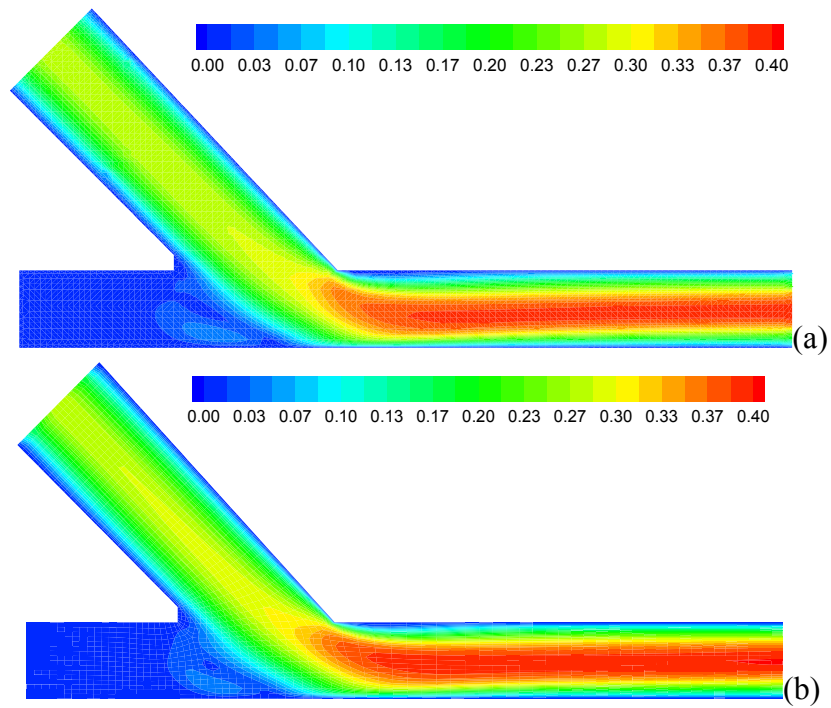
Figure 4.15: Conventional ETSDA model meshless (a) and FVM (b) velocity contours.
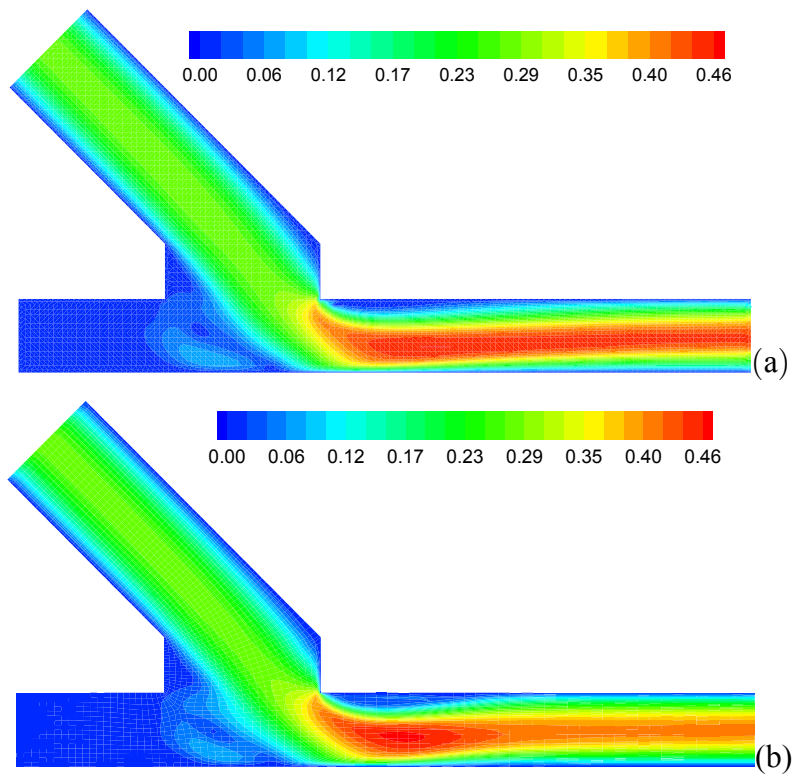
Figure 4.16: Miller cuff ETSDA model meshless (a) and FVM (b) velocity contours.
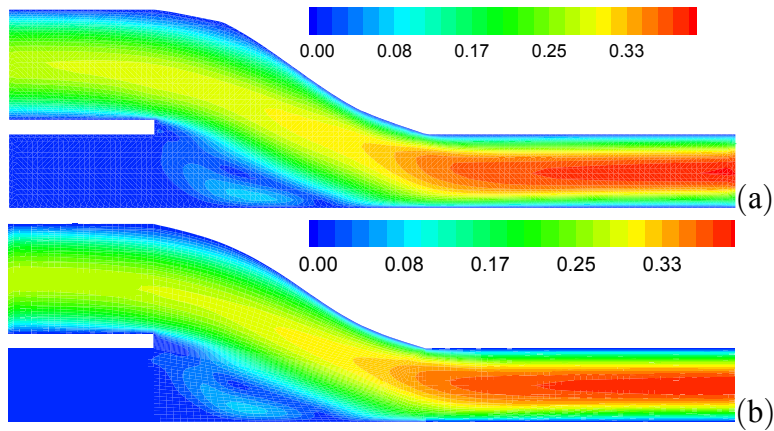
Figure 4.17: Hood ETSDA model meshless (a) and FVM (b) velocity contours.
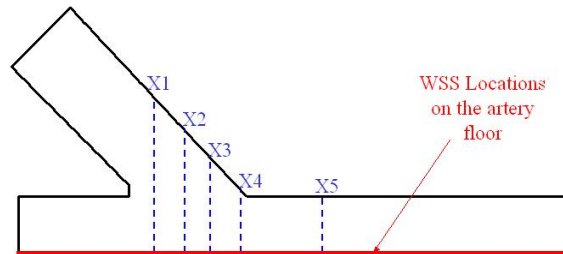
Figure 4.18: The x-velocity profiles and WSS locations for the conventional model.
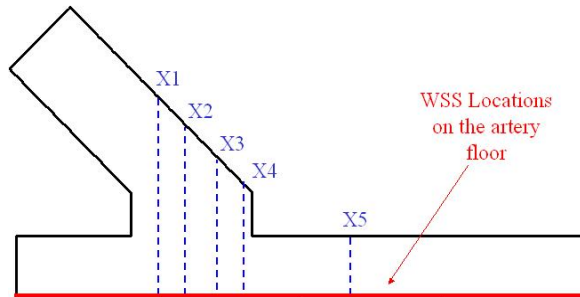
Figure 4.19: The x-velocity profiles and WSS locations for the Miller model.
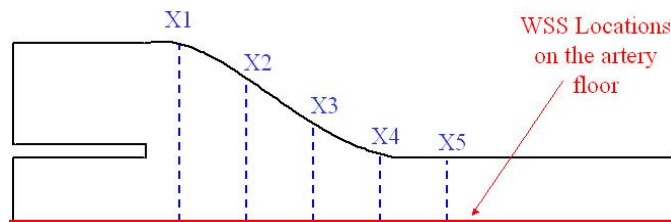
Figure 4.20: The x-velocity profiles and WSS locations for the hood model.
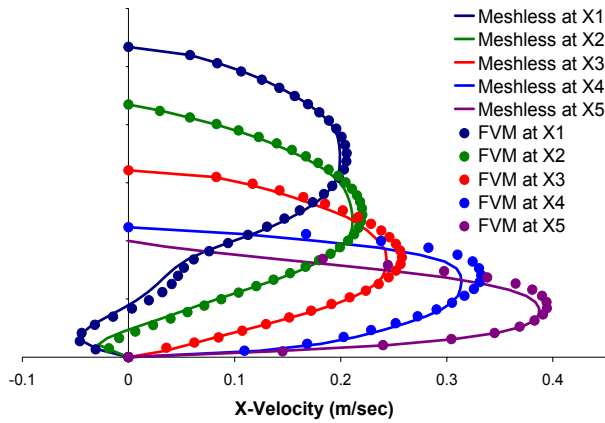
Figure 4.21: The x-velocity profiles the conventional ETSDA model.
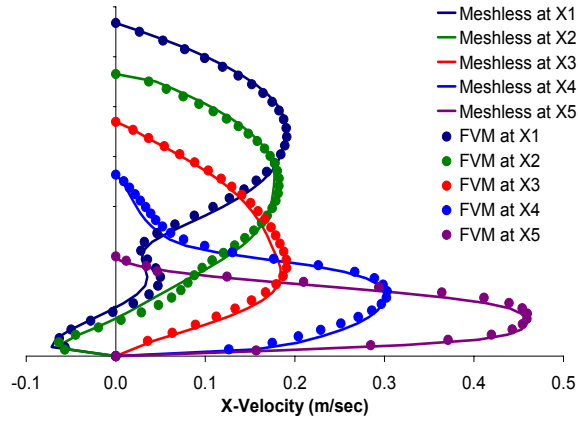
Figure 4.22: The x-velocity profiles for the Miller Cuff ETSDA model.
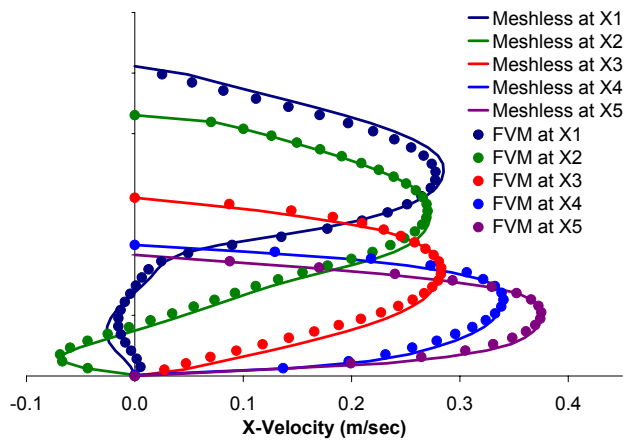
Figure 4.23: The x-velocity profiles for the hood ETSDA model.

Prior to reporting the validation results of the WSS on the ETSDA host artery floor, the definition of the WSS expression is briefly reviewed. As indicated earlier in the literature review, the WSS has a very important significance in hemodynamics and cardiovascular disease biogenesis. By definition, the WSS magnitude is equal to the norm of the traction vector

$$WSS = \left\| \vec{t} \right\| \tag{4.19}$$

The traction vector $\vec{t}$ is determined from the dot product between the unit normal vector ($\vec{n}$) at the boundary and the viscous stress tensor ($\overrightarrow{\overrightarrow{\tau}}$).

$$\vec{t} = \vec{n} \cdot \overrightarrow{\overrightarrow{\tau}} \tag{4.20}$$

For the sake of review, the incompressible flow viscous stress tensor in a 3D Cartesian coordinate system is given in Equation (4.21).

$$\overrightarrow{\overrightarrow{\tau}} = \mu \begin{bmatrix} 2\frac{\partial u}{\partial x} & \left(\frac{\partial u}{\partial y} + \frac{\partial v}{\partial x} \right) & \left(\frac{\partial u}{\partial z} + \frac{\partial w}{\partial x} \right) \\ \left(\frac{\partial u}{\partial y} + \frac{\partial v}{\partial x} \right) & 2\frac{\partial v}{\partial y} & \left(\frac{\partial v}{\partial z} + \frac{\partial w}{\partial y} \right) \\ \left(\frac{\partial u}{\partial z} + \frac{\partial w}{\partial x} \right) & \left(\frac{\partial v}{\partial z} + \frac{\partial w}{\partial y} \right) & 2\frac{\partial w}{\partial z} \end{bmatrix} \tag{4.21}$$

Subsequently, the x, y and z components of the traction vector are expressed as

$$t_x = \mu \left[2\frac{\partial u}{\partial x}n_x + \left(\frac{\partial u}{\partial y} + \frac{\partial v}{\partial x} \right)n_y + \left(\frac{\partial u}{\partial z} + \frac{\partial w}{\partial x} \right)n_z \right] \tag{4.22}$$

$$t_y = \mu \left[\left(\frac{\partial u}{\partial y} + \frac{\partial v}{\partial x} \right)n_x + 2\frac{\partial v}{\partial y}n_y + \left(\frac{\partial v}{\partial z} + \frac{\partial w}{\partial y} \right)n_z \right] \tag{4.23}$$

$$t_z = \mu \left[\left(\frac{\partial u}{\partial z} + \frac{\partial w}{\partial x} \right)n_x + \left(\frac{\partial v}{\partial z} + \frac{\partial w}{\partial y} \right)n_y + 2\frac{\partial w}{\partial z}n_z \right] \tag{4.24}$$

The WSS magnitudes are shown on the host artery floor for the 2D conventional ETSDA model, Miller Cuff ETSDA model, and the hood ETSDA model in Figures (4.24), (4.25), and (4.26) respectively.
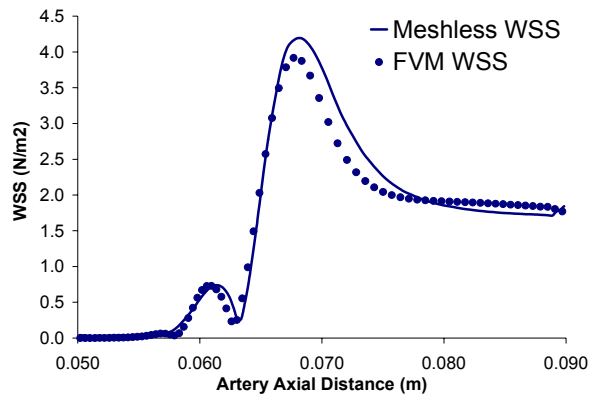
Figure 4.24: Meshless and FVM WSS plots at the artery floor of the conventional model.
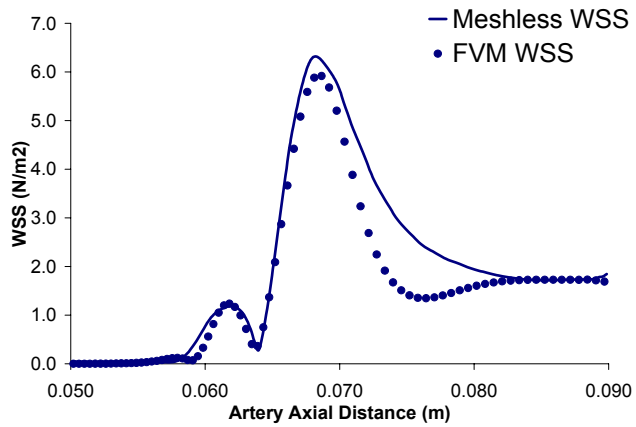
Figure 4.25: Meshless and FVM WSS plots at the artery floor of the Miller Cuff model.
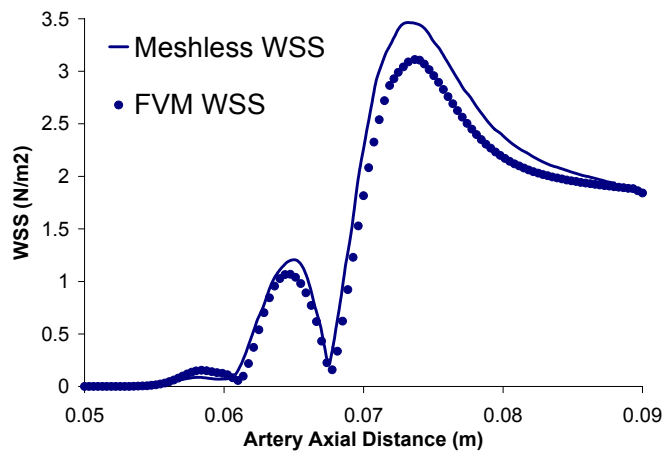
Figure 4.26: Meshless and FVM WSS plots at the artery floor of the hood model.

81

4.2.3 Pulsatile Flow Validation

Following the validation of the LCMM steady-state results, the unsteady capability of the LCMM is now tested through two different cases involving pulsatile flows in the conventional ETSDA geometry shown in Figure (4.6). The first case consists of a sinusoidal flow input waveform with an amplitude range between 0 and 125 (ml/min) and a period of 0.5 (sec). The plot of this sinusoidal waveform is illustrated in Figure (4.27). Note that four distinct times t_1, t_2, t_3, and t_4 are specified throughout the sinusoidal pulsatile cycle as indicated in Figure (4.27). The validation of the LCMM will be conducted at those four times.

The velocity contours of the LCMM sinusoidal pulsatile flow results as benchmarked against the FVM solver are revealed at t_1, t_2, t_3, and t_4 in Figures (4.28), (4.29), (4.30), and (4.31) respectively. Then, the sinusoidal pulsatile flow meshless and FVM x-velocity profiles at sections X1, X2, X3, X4, and X5 are plotted at the times t_1, t_2, t_3, and t_4 in Figures (4.32), (4.33), (4.34), and (4.35) respectively. The host artery floor WSS values subject the sinusoidal pulsatile flow are revealed in Figure (4.36) at all the four specified cycle times.
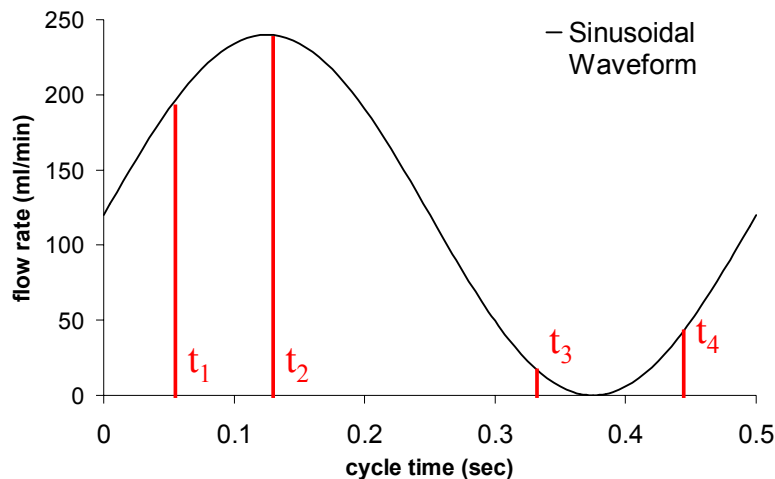
Figure 4.27: The sinusoidal flow waveform at the conventional ETSDA geometry inlet.
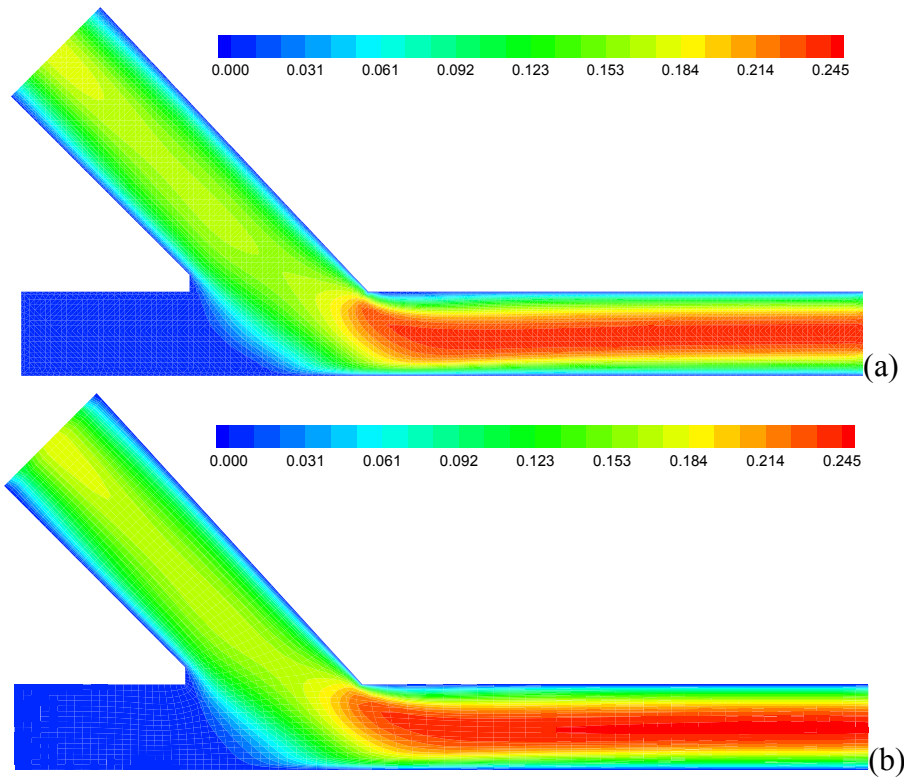
Figure 4.28: Meshless (a) and FVM (b) velocity contours at t_1 with sinusoidal flow.
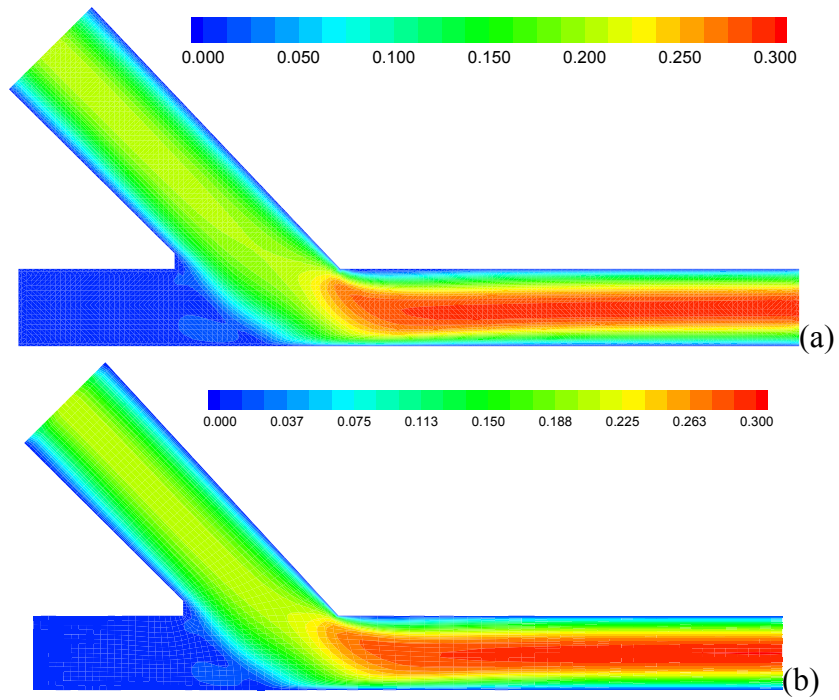
Figure 4.29: Meshless (a) and FVM (b) velocity contours at t_2 with sinusoidal flow.
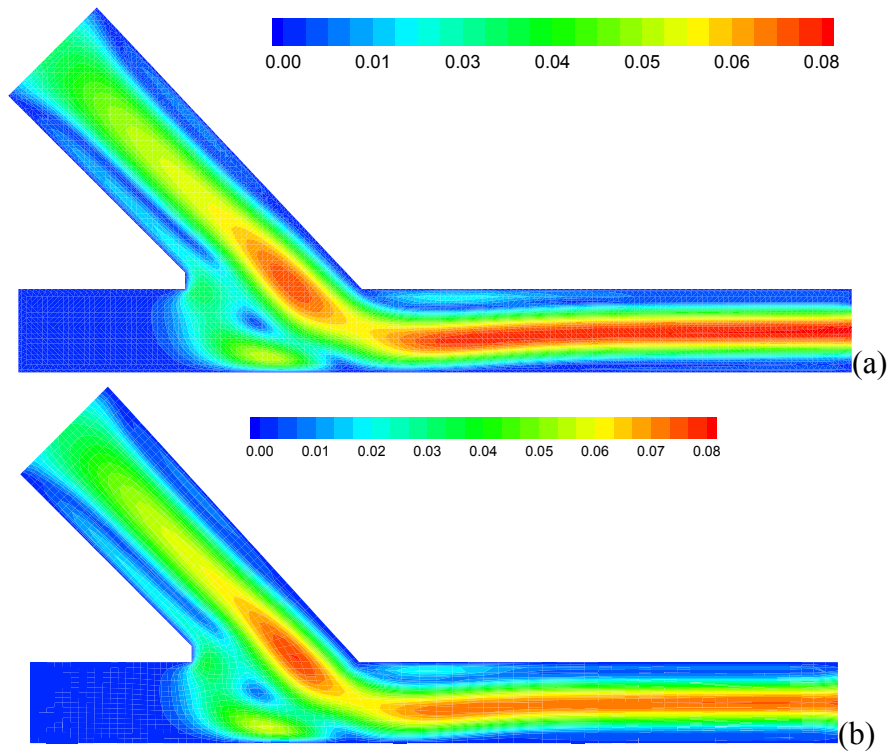
Figure 4.30: Meshless (a) and FVM (b) velocity contours at t_3 with sinusoidal flow.
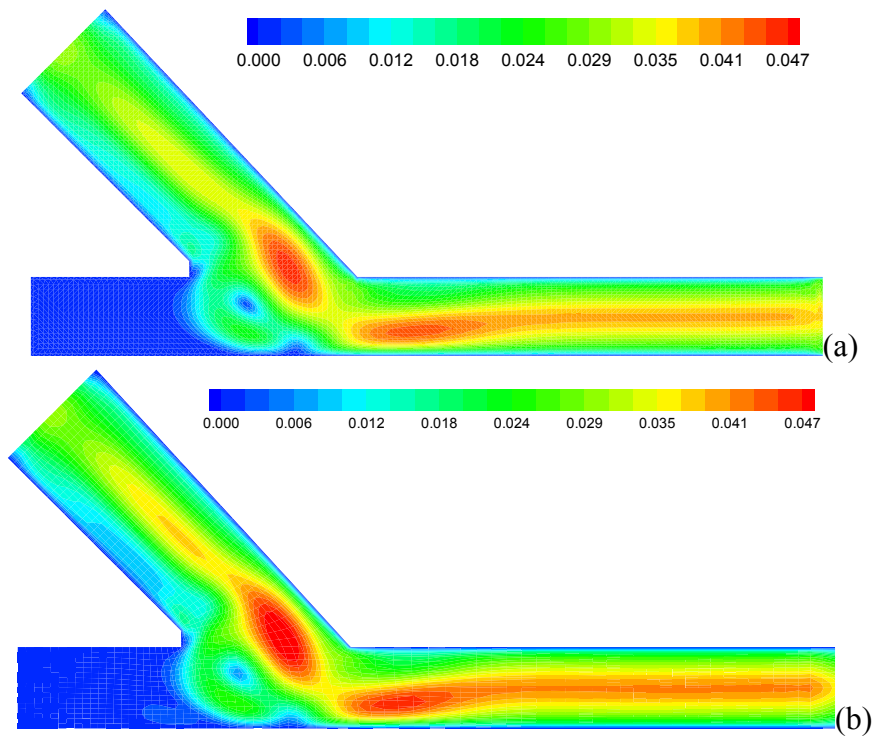
Figure 4.31: Meshless (a) and FVM (b) velocity contours at t_4 with sinusoidal flow.
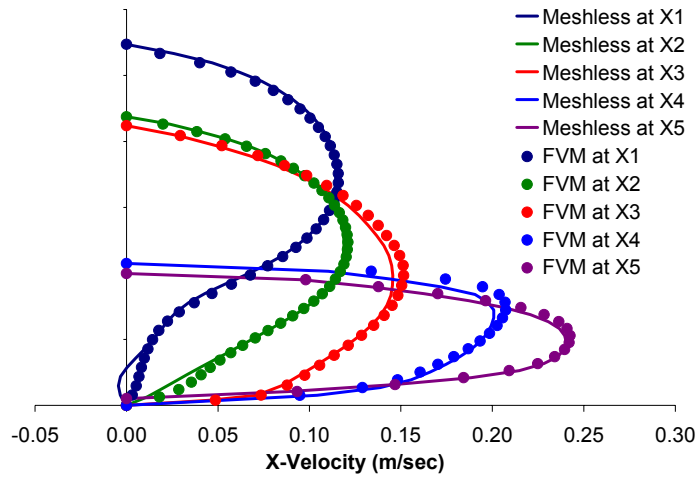
Figure 4.32: The x-velocity profiles for the conventional model at t_1 with sinusoidal flow.
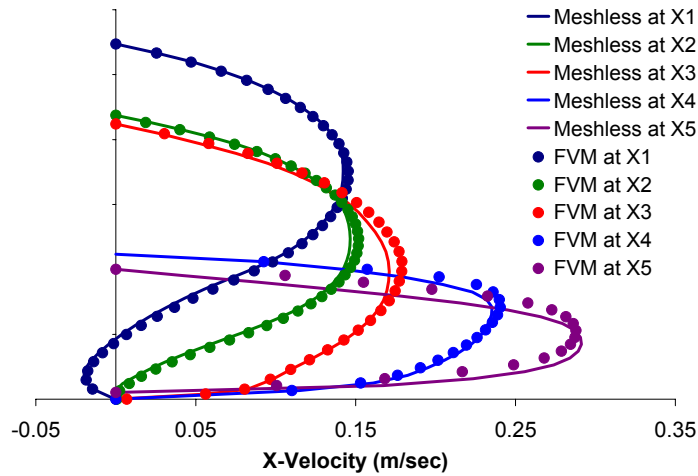
Figure 4.33: The x-velocity profiles for the conventional model at t_2 with sinusoidal flow.
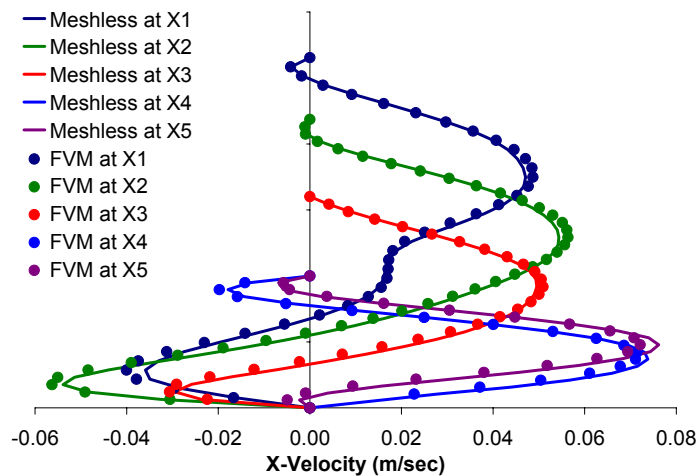
Figure 4.34: The x-velocity profiles for the conventional model at t_3 with sinusoidal flow.
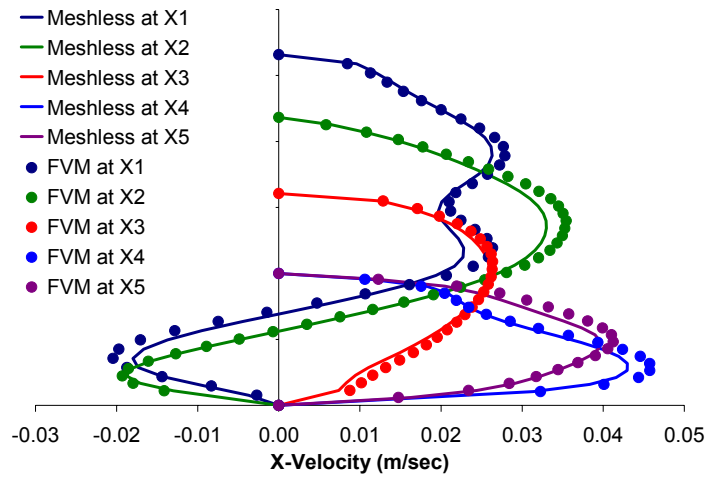
Figure 4.35: The x-velocity profiles for the conventional model at t_4 with sinusoidal flow.
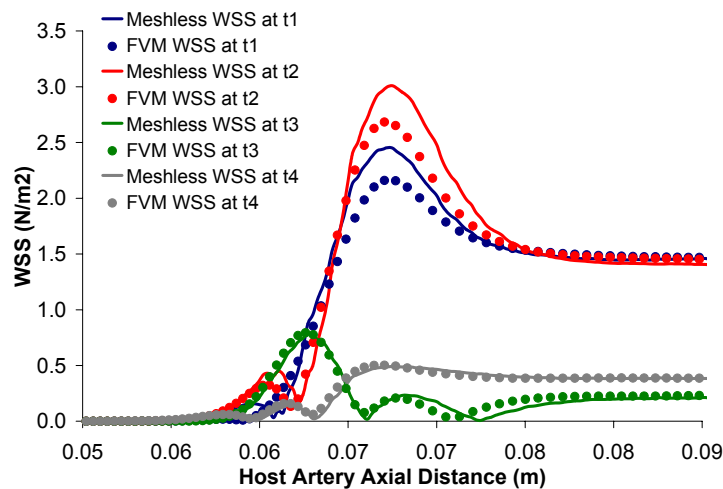
Figure 4.36: WSS in the conventional model at t_1, t_2, t_3, and t_4 with sinusoidal flow.

The pulsatile flow validation second case consists of a femoral artery flow input waveform with an amplitude range between 0 and 480 (ml/min) and a period of 0.7 (sec). Higher Reynolds numbers are expected through the femoral flow cycle compared to the previous sinusoidal flow cycle. The plot of the femoral inflow waveform is illustrated in Figure (4.37). The velocity contours of the LCMM femoral pulsatile flow results as benchmarked against the FVM solver are revealed at t_1, t_2, t_3, and t_4 in Figures (4.38), (4.39), (4.40), and (4.41)

respectively. Then, the femoral pulsatile flow meshless and FVM x-velocity profiles at sections X1, X2, X3, X4, and X5 are plotted at the times t_1, t_2, t_3, and t_4 in Figures (4.42), (4.43), (4.44), and (4.45) respectively. The host artery floor WSS values subject the femoral pulsatile flow are revealed in Figure (4.46) at all the four specified cycle times.
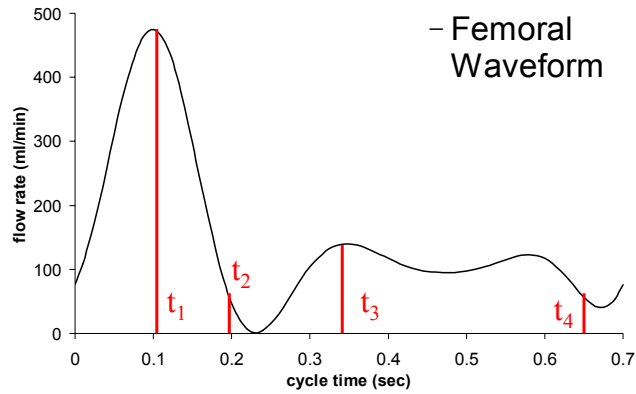
Figure 4.37: The femoral flow waveform at the conventional ETSDA geometry inlet.
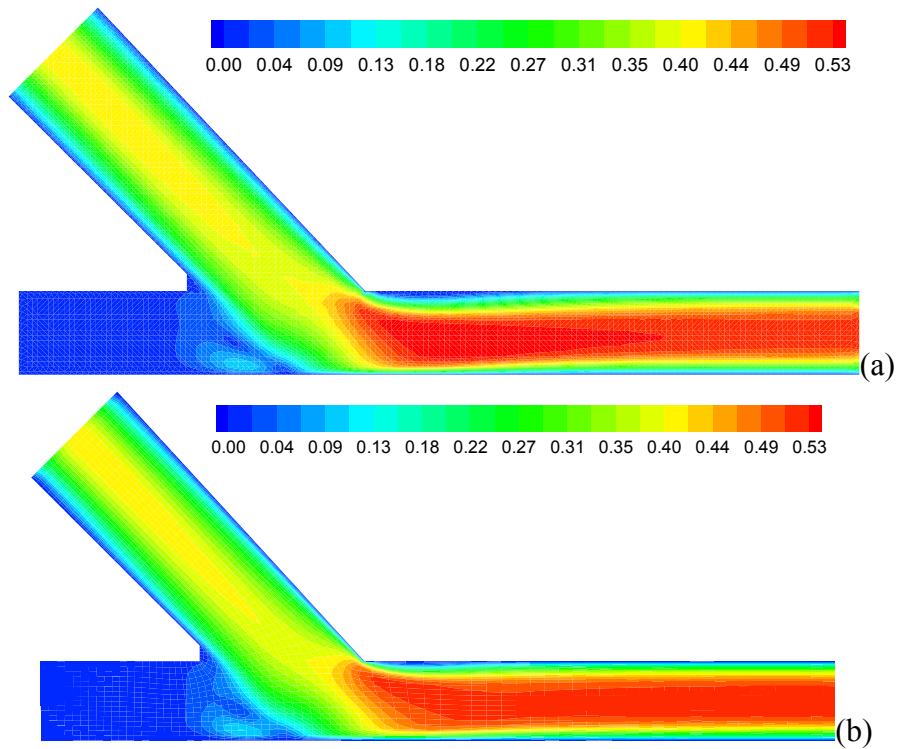
Figure 4.38: Meshless (a) and FVM (b) velocity contours at t_1 with femoral flow.
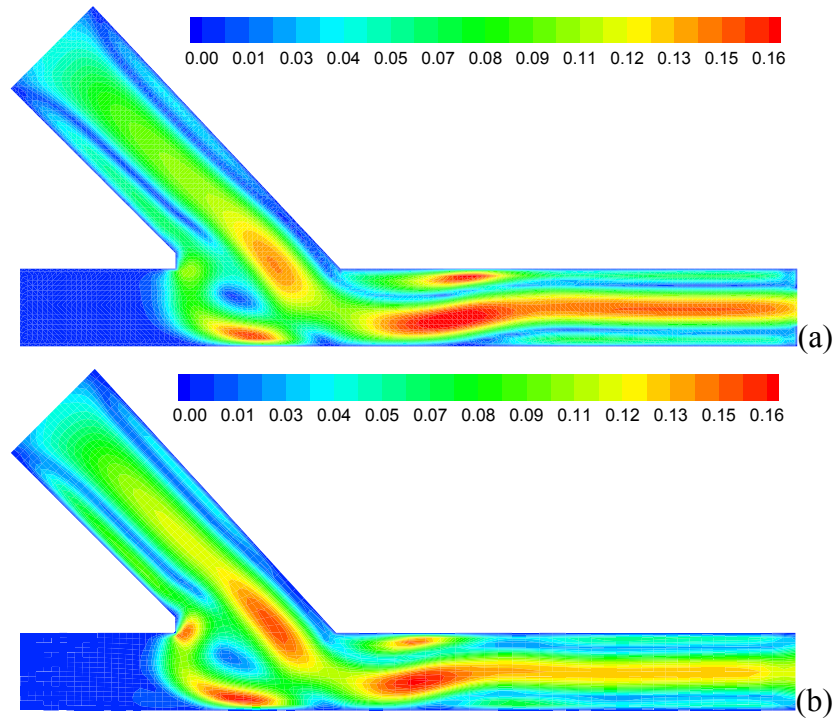
Figure 4.39: Meshless (a) and FVM (b) velocity contours at t_2 with femoral flow.
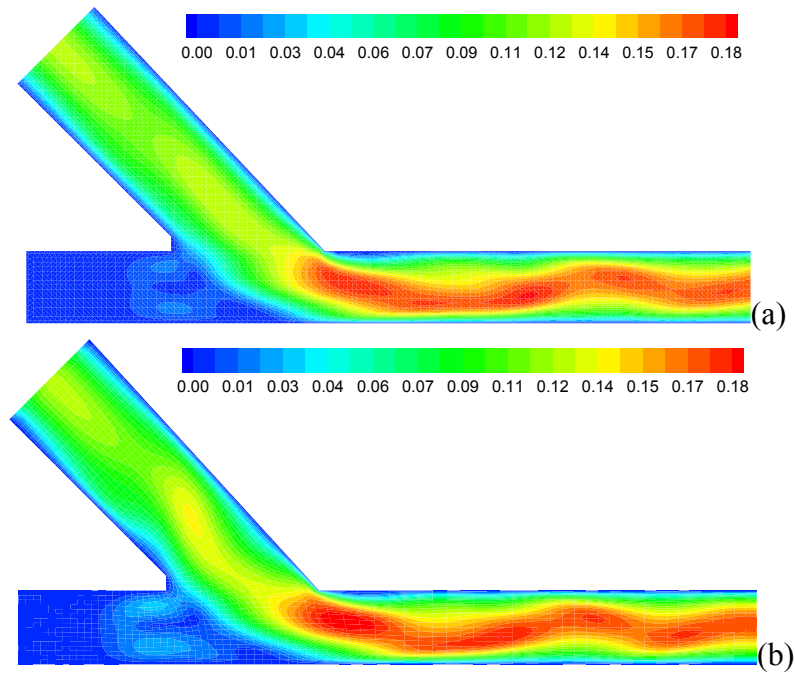
Figure 4.40: Meshless (a) and FVM (b) velocity contours at t_3 with femoral flow.
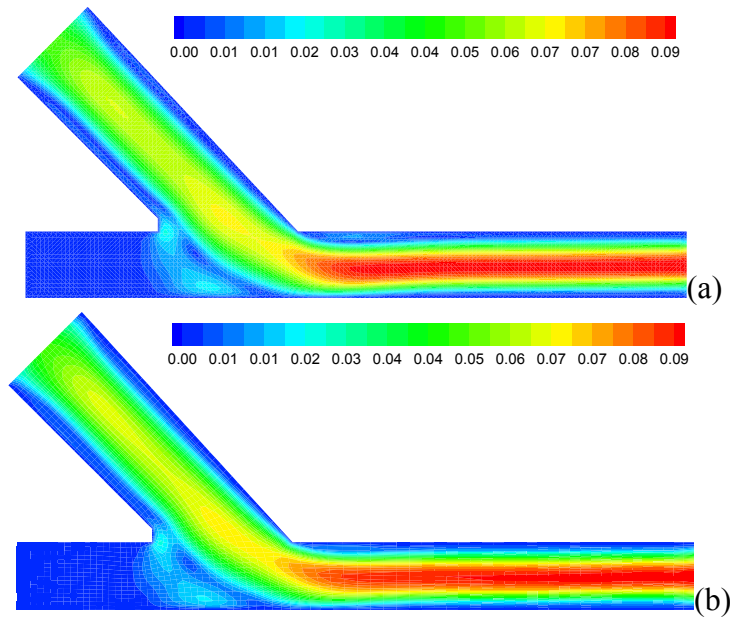
Figure 4.41: Meshless (a) and FVM (b) velocity contours at t_4 with femoral flow.
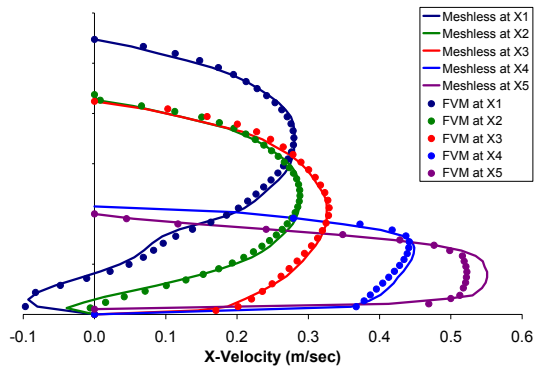
Figure 4.42: The x-velocity profiles for the conventional model at t_1 with femoral flow.
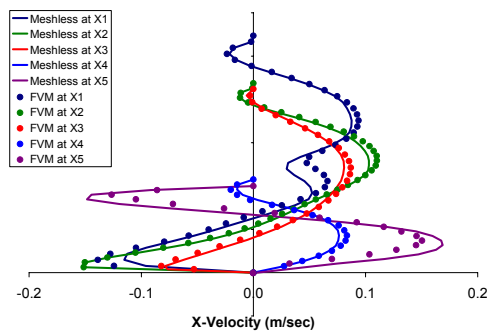
Figure 4.43: The x-velocity profiles for the conventional model at t_2 with femoral flow.
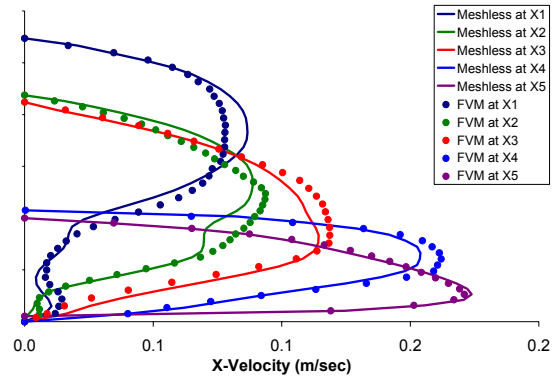
Figure 4.44: The x-velocity profiles for the conventional model at t_3 with femoral flow.
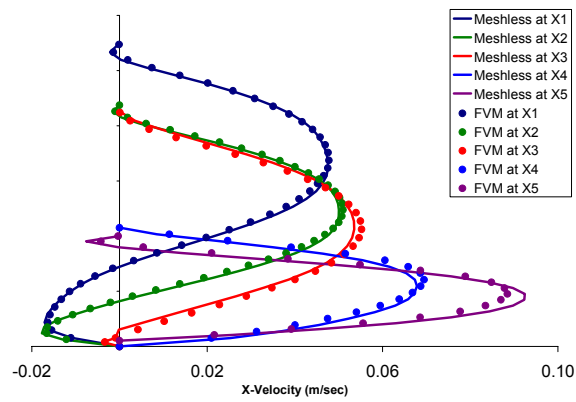
Figure 4.45: The x-velocity profiles for the conventional model at t_4 with femoral flow.
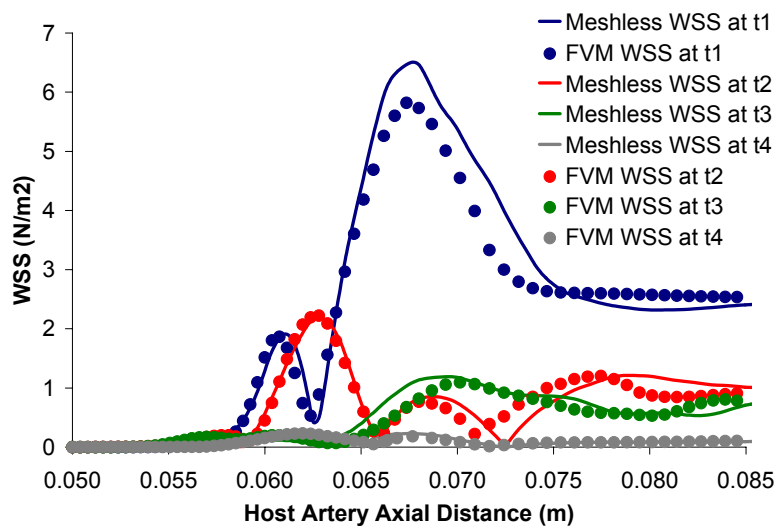
Figure 4.46: WSS in the conventional model at t_1, t_2, t_3, and t_4 with femoral flow.

All the velocity contours for the pulsatile flow validation cases indicate an acceptable level of accuracy of the LCMM. Discrepancies seems to occur mainly during the decelerating phase of the pulsatile cycle as in Figures (4.30) and (4.39). Besides, the x-velocity profiles and the host artery floor WSS comparisons demonstrate a good agreement between the unsteady flow capabilities of both the LCMM and the FVM solver.

4.2.4 LCMM Capability on Highly Irregular Geometries

The present sub-section is intended to prove that the LCMM is able to simulate the incompressible flow not only on mildly irregular geometries as in Figures (4.6), (4.7), and (4.8), but also on highly irregular geometries such as the one seen in Figures (4.6). This irregular geometry actually replicates the growth of the IH on the vulnerable heel, toe and arterial floor areas in the ETSDA. The femoral waveform in Figure (4.27) is employed to drive the pulsatile flow in this particular geometry. The automated point distribution for this particular example is revealed in Figure (4.48). The capability of the LCMM with regard to irregular geometries is proven through the velocity contours shown at t_1, t_2, t_3, and t_4 in Figures (4.49), (4.50), (4.51), and (4.52) respectively.

The capability of the LCMM of simulating cardiovascular flows in complex-shaped irregular geometries would have a great significance for the cardiovascular research community. FVM-based mesh generation is a very intricate task for image-reconstructed cardiovascular anatomical geometries. Thus, the LCMM can be an alternative in this particular biomedical engineering application thanks to its seamless automated pre-processing. The simulation of the blood flow in these geometries is of tremendous interest for scientists to understand the ETSDA IH biogenesis [95,96].
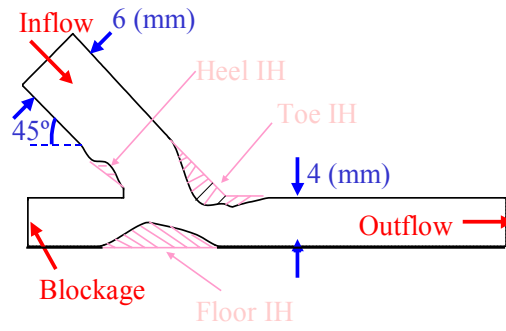
Figure 4.47: The conventional ETSDA geometry with the IH disease condition.
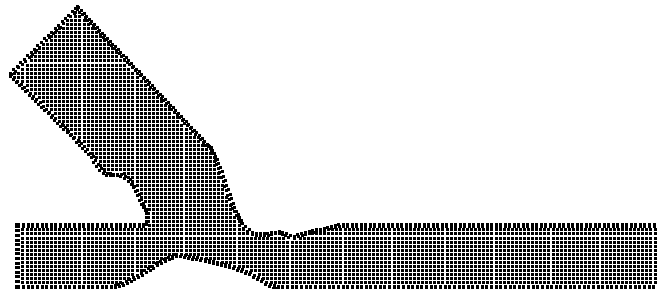
Figure 4.48: The point distribution in the diseased conventional ETSDA geometry.
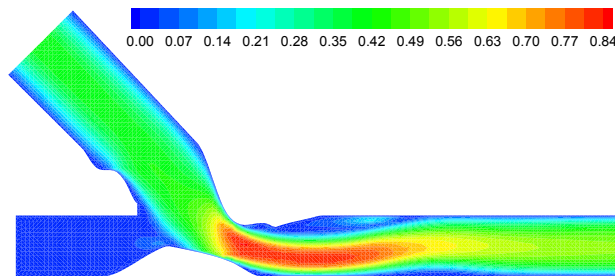
Figure 4.49: Meshless velocity contours at t_1 in the diseased conventional ETSDA.
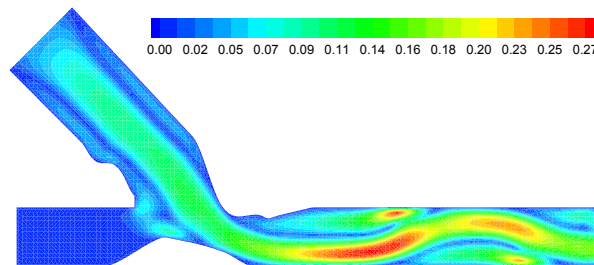
Figure 4.50: Meshless velocity contours at t_2 in the diseased conventional ETSDA.

92
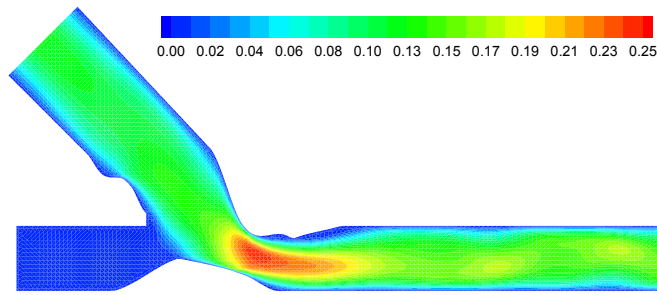
Figure 4.51: Meshless velocity contours at t_3 in the diseased conventional ETSDA.
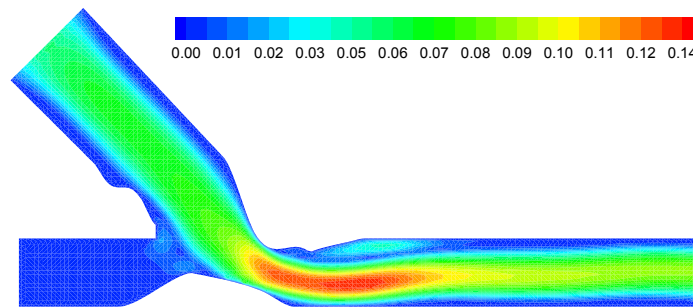
Figure 4.52: Meshless velocity contours at t_4 in the diseased conventional ETSDA.

4.3 The LCMM Non-Newtonian Model

4.3.1 Review on the Blood Rheology

An infinitesimal fluid element is non-Newtonian when the relationship between the shear stress and the shear rate on that element is non-linear. Theoretically, for a Newtonian fluid at a given temperature the stress varies linearly with the shear rate and the viscosity has a constant value. High molecular weight polymer fluids as well as particles carrying fluids are usually non-Newtonian. The non-Newtonian fluids are classified as shear-thinning or shear-thickening depending on the viscosity variation with the shear rate. For a shear thinning fluid, the viscosity decreases as the shear rate increases. The shear thinning property is found in daily-used complex solutions, such as ketchup, tooth paste, paint, and nail polish [97]. On the other hand, the

viscosity increases as the shear rate increases in a shear thickening fluid. An attractive application of the shear thickening fluids is found in bullet-proofing clothes. Those clothes are made with fabric treated with shear-thickening granular suspensions that can turn soft material into solid protective gear when struck by a projectile [98].

For the particular application of hemodynamics, blood is considered as a non-Newtonian fluid due to its particle-suspended-aqueous composition. More specifically, blood consists of plasma as a bulk medium transporting several types of particles. The plasma is an aqueous solution of electrolytes and organic substances, mainly proteins. Those proteins comprise of fibrinogen (5% in volume), globulins (45% in volume), albumin (50% in volume), and minute traces of beta lipoprotein and lipalbumin. The blood particles consist of the Red Blood Cells (RBCs) also known as erythrocytes, the White Cells (WBCs) also known as leucocytes, and the Platelets also known as thrombocytes. The RBCs are the major constituent of the particles (95% in volume). A single RBC consists of an elastic membrane containing a concentrated solution known as 'Haemoglobin' which specific gravity is five times that of the plasma. As a mechanical consequence, the RBCs will settle at the bottom of a container including blood at static (zero shear) conditions. The settlement of RBCs forms a continuous structure of cell aggregates made up of single cells; those cell aggregates are called flocs or rouleaux. In regions where the RBCs are aggregated, the blood viscosity is at a high end known as the zero-shear viscosity. As blood is gradually sheared under certain flow conditions, the RBC flocs or rouleaux break down to smaller clusters decreasing the viscosity to a low end value known as the infinite-shear viscosity. The blood behaves as Newtonian once the viscosity is at the infinite shear level, whereas it behaves as non-Newtonian when the viscosity is between the zero-shear and infinite-shear limits; this viscosity behavior indicates that blood is a shear thinning fluid. Figure (4.53) reveals the blood rheological behavior; for low shear rates the stess-shear rate relation in non-linear (non-Newtonian behavior), whereas for high shear rates the relation is linear (Newtonian behavior where the viscosity is constant).
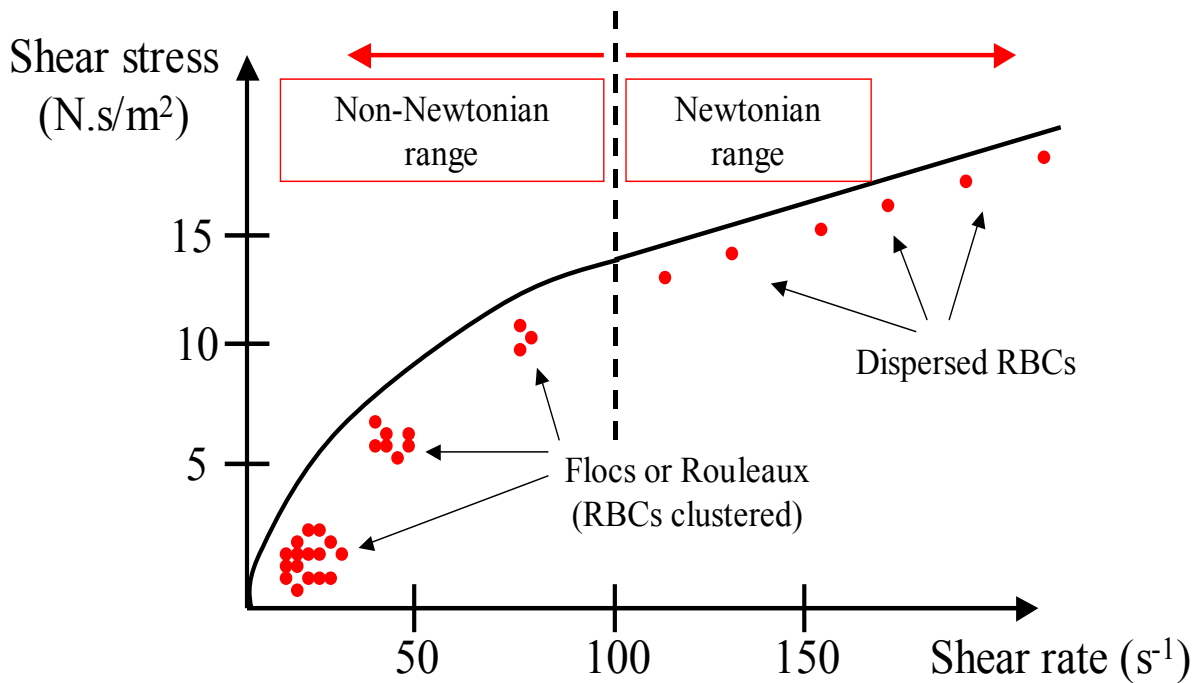
Figure 4.53: The blood linear and non-linear rheological behavior.

There are several mathematical models that represent the blood viscosity as a function of the shear rate $\dot\gamma$ in the non-Newtonian range. The Casson model [99,103] is one of the first such models that accounts for the yield stress; the Casson model assumes that the yield stress must be surpassed before the RBC rouleaux could be broken. The advantage of the Casson model is that it can express the stress-strain behavior for a wide range of RBC concentration and shear rates [1-100000 $(\sec^{-1})$]. Conversely, the Casson model disadvantage is signaled by the inverse relationship between the viscosity and the shear rate; the near-zero values of the shear rate lead to major difficulties in numerical modeling. To circumvent the Casson model shortcomings, the power law model of Walburn and Schneck [100,102,103], the Quemeda model [101,102,103] and the Carreau model [104] were then proposed. The viscosity-shear-rate relations for the power law and Quemeda models are illustrated in Figure (4.54) and for the Carreau model in Figure (4.55). All the models seem to agree very well with experimental data from Merill [105]

while covering the non-Newtonian range of the shear rate. The Carreau model is selected for the LCMM simulation of the blood flow.
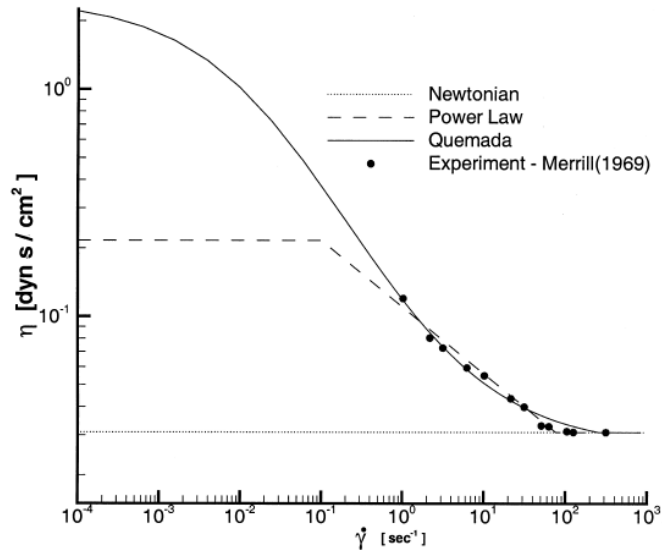
Figure 4.54: Viscosity non-Newtonian trends for the Power Law and Quemeda models [102].
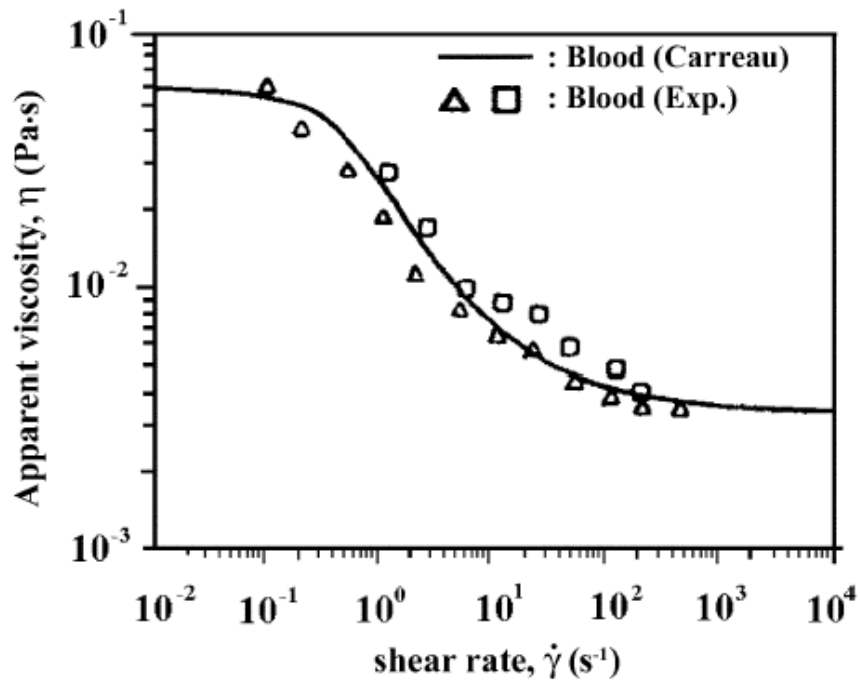
Figure 4.55: Viscosity non-Newtonian trends for the Carreau model [104].

4.3.2 Non-Newtonian Form of the Navier-Stokes Equations

This sub-section entails the re-formulation of the linear momentum equation in order to account for the non-Newtonian effects. Examining Equation (4.2), the viscosity spatial variability needs to be addressed in the divergence of the viscous stress tensor term $\overrightarrow{\overrightarrow{\tau}}$. The x-momentum equation is

$$\rho \frac{\partial u}{\partial t} + \rho \overrightarrow{V} \cdot \nabla u = -\frac{\partial p}{\partial x} + \nabla \cdot \overrightarrow{\tau_x} \tag{4.25}$$

Here $\overrightarrow{\tau_x}$ is the x-component of $\overrightarrow{\overrightarrow{\tau}}$ and it can be expressed as

$$\overrightarrow{\tau_x} = \left[\mu \left(2\frac{\partial u}{\partial x} \right) \right]\overrightarrow{i} + \left[\mu \left(\frac{\partial u}{\partial y} + \frac{\partial v}{\partial x} \right) \right]\overrightarrow{j} + \left[\mu \left(\frac{\partial u}{\partial z} + \frac{\partial w}{\partial x} \right) \right]\overrightarrow{k} \tag{4.26}$$

The divergence of $\overrightarrow{\tau_x}$ is then expressed as

$$\nabla \cdot \overrightarrow{\tau_x} = \frac{\partial}{\partial x}\left[\mu \left(2\frac{\partial u}{\partial x} \right) \right] + \frac{\partial}{\partial y}\left[\mu \left(\frac{\partial u}{\partial y} + \frac{\partial v}{\partial x} \right) \right] + \frac{\partial}{\partial z}\left[\mu \left(\frac{\partial u}{\partial z} + \frac{\partial w}{\partial x} \right) \right] \tag{4.27}$$

by chain rule

$$\nabla \cdot \overrightarrow{\tau_x} = \mu \frac{\partial}{\partial x}\left(2\frac{\partial u}{\partial x} \right) + \mu \frac{\partial}{\partial y}\left(\frac{\partial u}{\partial y} + \frac{\partial v}{\partial x} \right) + \mu \frac{\partial}{\partial z}\left(\frac{\partial u}{\partial z} + \frac{\partial w}{\partial x} \right)$$
$$+ 2\frac{\partial u}{\partial x}\frac{\partial \mu}{\partial x} + \left(\frac{\partial u}{\partial y} + \frac{\partial v}{\partial x} \right)\frac{\partial \mu}{\partial y} + \left(\frac{\partial u}{\partial z} + \frac{\partial w}{\partial x} \right)\frac{\partial \mu}{\partial z} \tag{4.28}$$

or finally

$$\nabla \cdot \overrightarrow{\tau_x} = \mu \nabla \cdot (\nabla u) + \mu \frac{\partial}{\partial x}\left(\nabla \cdot \overrightarrow{V} \right) + \nabla u \cdot \nabla \mu + \left(\nabla \cdot \overrightarrow{V} \right)\frac{\partial \mu}{\partial x} \tag{4.29}$$

Recognizing the free divergence of an incompressible velocity field, Equation (4.29) reduces to

$$\nabla \cdot \overrightarrow{\tau_x} = \mu \nabla^2 u + \nabla u \cdot \nabla \mu \tag{4.30}$$

Substituting Equation (4.30) into Equation (4.33) leads to a new form of the x-direction linear momentum equation as

$$\rho\frac{\partial u}{\partial t} + \rho\left(\vec{V} - \frac{\nabla\mu}{\rho}\right)\cdot\nabla u = -\frac{\partial p}{\partial x} + \mu\nabla^2 u \tag{4.31}$$

Likewise, the divergence of the $\overrightarrow{\tau}$ y- and z-components can be executed to eventually lead to new forms of the y- and z-directions linear momentum equations

$$\rho\frac{\partial v}{\partial t} + \rho\left(\vec{V} - \frac{\nabla\mu}{\rho}\right)\cdot\nabla v = -\frac{\partial p}{\partial y} + \mu\nabla^2 v \tag{4.32}$$

$$\rho\frac{\partial w}{\partial t} + \rho\left(\vec{V} - \frac{\nabla\mu}{\rho}\right)\cdot\nabla w = -\frac{\partial p}{\partial z} + \mu\nabla^2 w \tag{4.33}$$

More generally, the linear momentum equation can be re-written in a vector form accounting for the non-Newtonian effects as

$$\rho\frac{\partial\vec{V}}{\partial t} + \rho\left(\vec{V} - \frac{\nabla\mu}{\rho}\right)\cdot\nabla\vec{V} = -\nabla p + \mu\nabla^2\vec{V} \tag{4.34}$$

For the re-formulated linear momentum equation, $\rho\left(\vec{V} - \frac{\nabla\mu}{\rho}\right)\cdot\nabla\vec{V}$ represents the convective term that must be treated to avoid numerical instabilities. As such, the entity $\left(\vec{V} - \frac{\nabla\mu}{\rho}\right)$ is considered as an effective velocity based on which the upwinding Reynolds numbers are determined. For the non-Newtonian form of the N-S equations, the expressions of the upwinding Reynolds numbers, Re_x, Re_y and Re_z, are given in Equations (4.35), (4.36), and (4.37) respectively. The upwinding strategy is the same as previously explained.

$$Re_x = \rho\left\|u - \frac{1}{\rho}\frac{\partial\mu}{\partial x}\right\|\delta/\mu \tag{4.35}$$

$$Re_y = \rho\left\|v - \frac{1}{\rho}\frac{\partial\mu}{\partial y}\right\|\delta/\mu \tag{4.36}$$

$$Re_z = \rho\left\|w - \frac{1}{\rho}\frac{\partial\mu}{\partial z}\right\|\delta/\mu \tag{4.37}$$

As discussed earlier, the dynamic viscosity μ is a function of the shear rate $\dot{\gamma}$; The expression of μ is given by the Carreau model such as shown in Equation (4.38).

$$\mu = \mu_\infty + (\mu_0 - \mu_\infty)\left[1 + (\lambda\dot{\gamma})^2\right]^{\frac{n-1}{2}} \tag{4.38}$$

Here μ_∞ is the infinite shear viscosity, μ_0 is the zero shear viscosity, λ is the time constant, and npl is the power law index. The analytical curvefit shown in Figure (4.55), requires the following Carreau model parameters: $\mu_\infty = 0.00345\,(Nsec/m^2)$, $\mu_0 = 0.056\,(Nsec/m^2)$, $\lambda = 3.31\,(sec)$, $n = 0.357$. The shear rate is expressed in terms of the viscous stress tensor $\overrightarrow{\overrightarrow{\tau}}$ magnitude as given in Equation (4.39).

$$\dot{\gamma} = \left\| \overrightarrow{\overrightarrow{\tau}} \right\| = \sqrt{\frac{1}{2}\overrightarrow{\overrightarrow{\tau}} : \overrightarrow{\overrightarrow{\tau}}} \tag{4.39}$$

4.3.3 Validation of the LCMM Non-Newtonian Model

The validation of the LCMM Carreau non-Newtonian results is conducted under pulsatile flow conditions driven by the femoral waveform shown in Figure (4.37). The non-Newtonian case validation geometry, point distribution, and FVM mesh are shown in Figures (4.56), (4.57), and (4.58) respectively. The incoming flow through the graft is split in a one-third and two-third proportions as it impinges on the floor of the host artery. The two-third proportion exits the domain via the distal outlet, whereas the one-third proportion exits via the proximal outlet. The splitting proportions remain the same throughout the entire pulsatile cycle. The velocity contours of the LCMM pulsatile and non-Newtonian results as benchmarked against the FVM solver are revealed at t_1, t_2, t_3, and t_4 in Figures (4.60), (4.61), (4.62), and (4.63) respectively. Figure (4.59) shows the locations of the validation x-velocity profiles and WSS. The pulsatile flow LCMM and FVM x-velocity profiles at sections X1, X2, X3, and X4 under non-Newtonian conditions are plotted at the times t_1, t_2, t_3, and t_4 in Figures (4.64), (4.65), (4.66), and (4.67)

respectively. The host artery floor WSS values subject the femoral pulsatile flow under non-Newtonian conditions are shown in Figure (4.68) at t_1, t_2, t_3, and t_4.
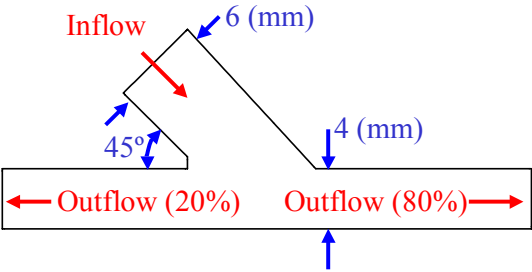
Figure 4.56: The schematic of the non-Newtonian case geometry.
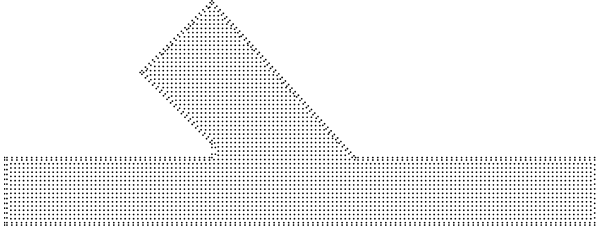
Figure 4.57: The automated point distribution for the non-Newtonian case.
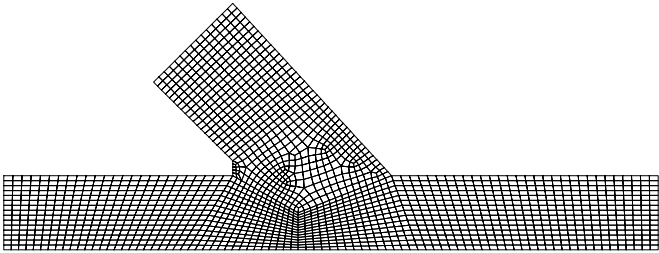
Figure 4.58: The FVM mesh for the non-Newtonian case.
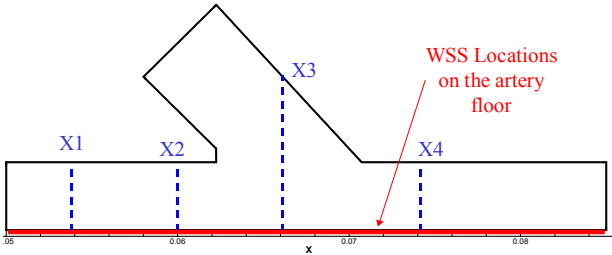
Figure 4.59: The x-velocity profiles and WSS locations for the non-Newtonian case.
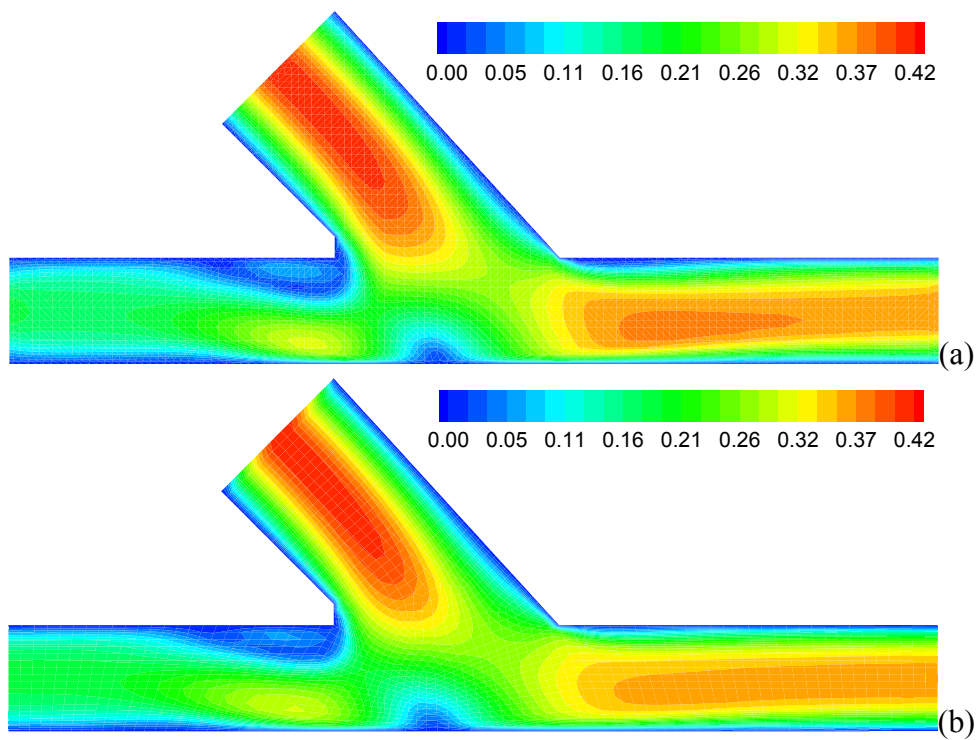
Figure 4.60: Meshless (a) and FVM (b) non-Newtonian velocity contours at t_1.
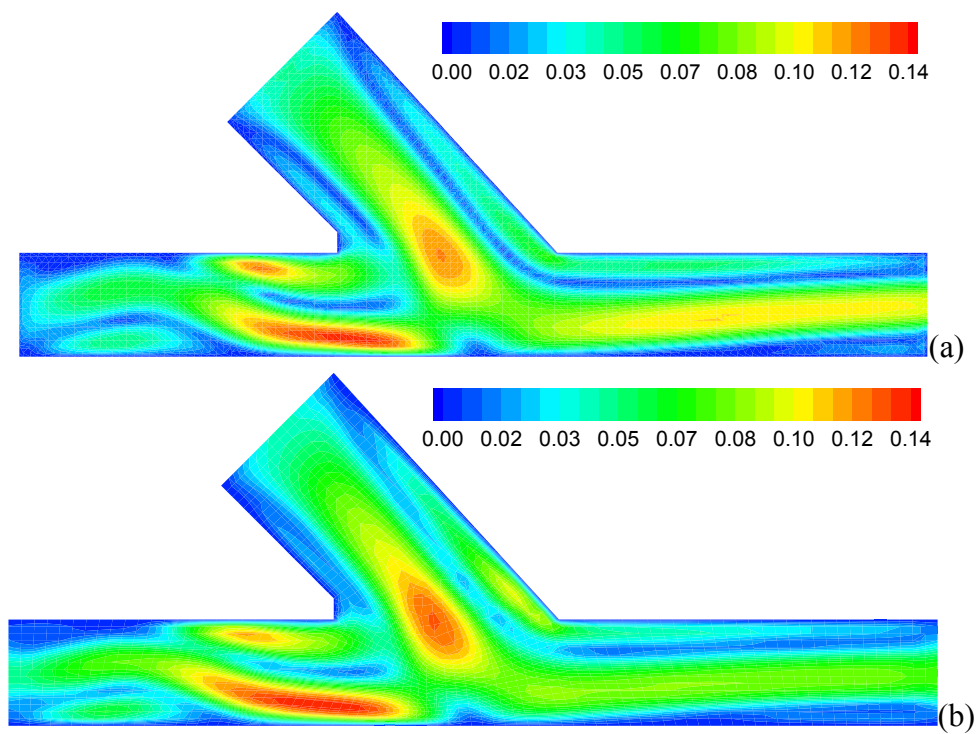
Figure 4.61: Meshless (a) and FVM (b) non-Newtonian velocity contours at t_2.
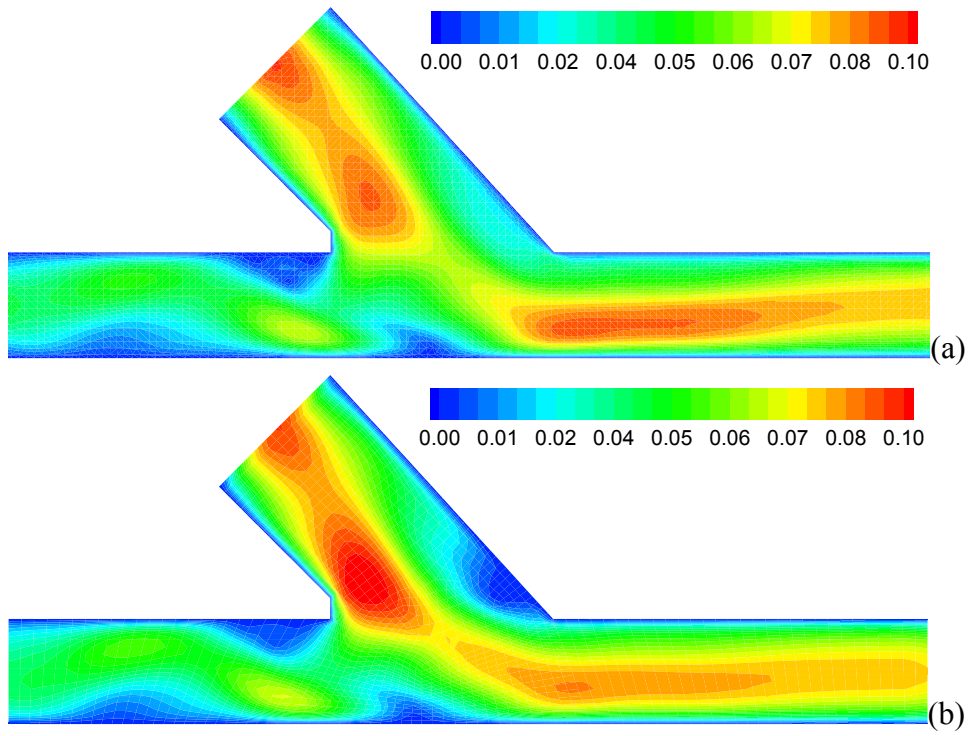
Figure 4.62: Meshless (a) and FVM (b) non-Newtonian velocity contours at t_3.
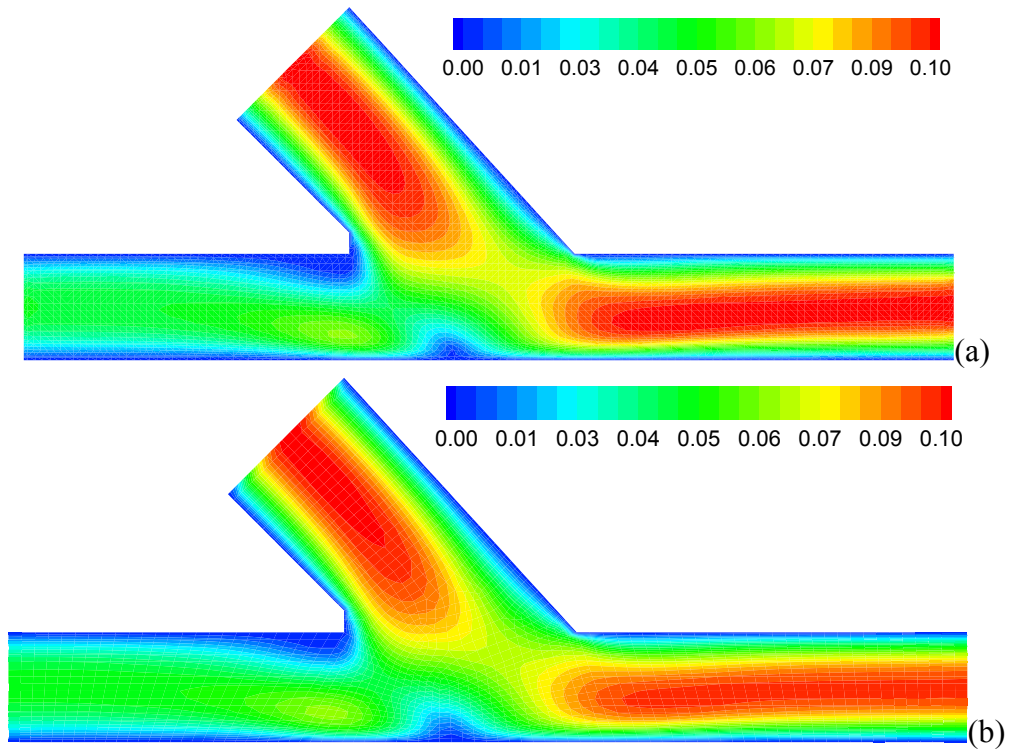
Figure 4.63: Meshless (a) and FVM (b) non-Newtonian velocity contours at t_4.
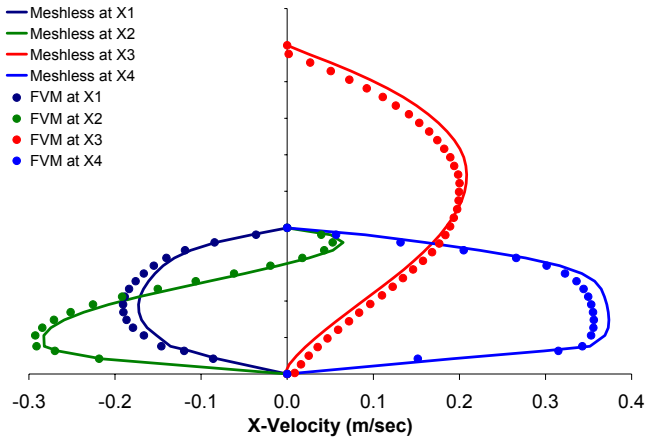
Figure 4.64: The non-Newtonian case x-velocity profiles for the conventional model at t_1.
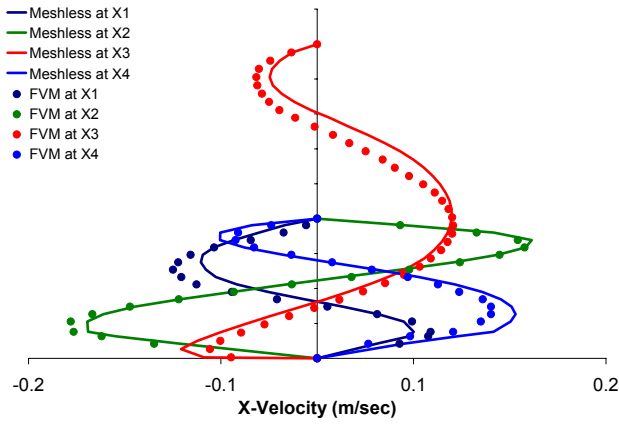
Figure 4.65: The non-Newtonian case x-velocity profiles for the conventional model at t_2.
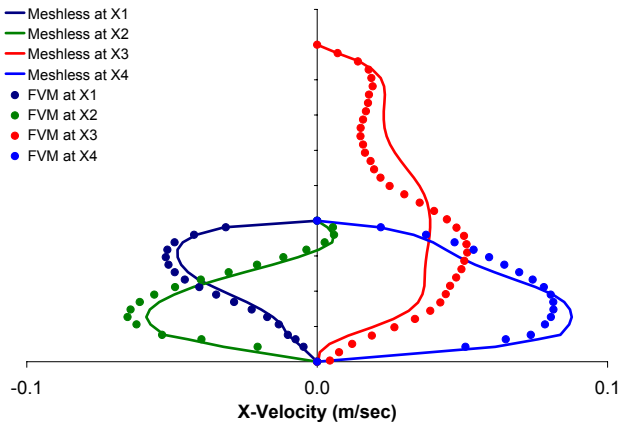
Figure 4.66: The non-Newtonian case x-velocity profiles for the conventional model at t_3.
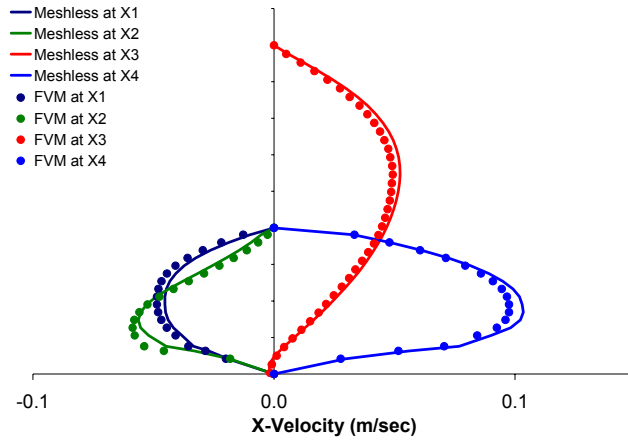
Figure 4.67: The non-Newtonian case x-velocity profiles for the conventional model at t_4.
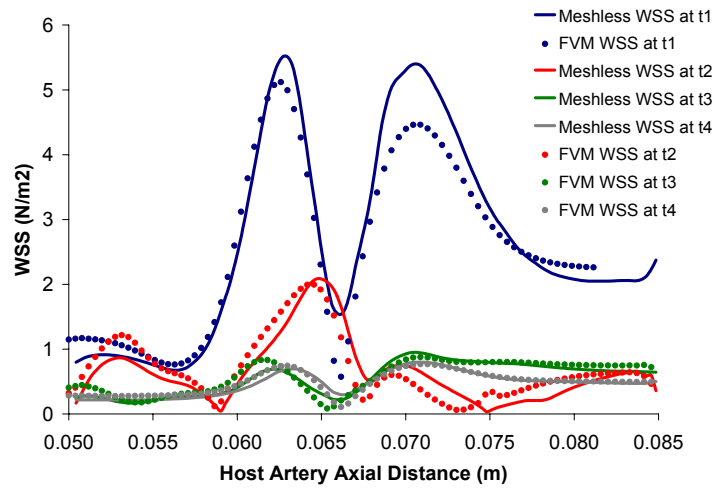
Figure 4.68: The non-Newtonian case WSS on the conventional model floor at t_1, t_2, t_3, and t_4.

CHAPTER 5: THE ESTDA SHAPE OPTIMIZATION

5.1 Evolutionary Optimization Review

The current section holds a review on the concept of evolutionary optimization. The section starts with a presentation of the general framework of evolutionary algorithms. Then, a discussion on the genetic algorithms and their operations is developed. Subsequently, the concepts of single-objective and multi-objective optimization will be investigated.

5.1.1 A General Framework of Evolutionary Algorithms

Evolutionary optimization is the study of optimization approaches that use ideas and derives inspirations from the natural evolution of living systems. Evolutionary optimization is intended to optimize systems that exhibit high non-linear behaviors and noisy data. All evolutionary optimization algorithms have two prominent features which distinguish themselves from other optimization algorithms. First, they work with a population of individuals representing different solutions, instead of a single solution representing one single individual. Second, there is communication exchange among individuals in the population. Such communication and information exchange are the result of selection and/or recombination of evolutionary algorithms. A general framework of the evolutionary algorithms can be summarized by the following,

1   Set $i=0$

2   Generate the initial generation $GEN(i)$

3   REPEAT

    a.   Evaluate the Fitness of each individual in $GEN(i)$

b.   Select Parents from $GEN(i)$ based on their fitness

c.   Apply SEARCH OPERATORS to the parents and produce generation $GEN(i+1)$;

4   UNTIL a preset number of generations is reached.

The search operators are used to generate offsprings (new individuals) from parents (existing individuals). Different representations of individuals and different schemes for implementing fitness evaluation, selection and search operators define different algorithms.

5.1.2 The Theory of Genetic Algorithms

A comprehensive review and insight on the genetic algorithms (GAs) can be found in the textbooks of Goldberg [106] and Haupt [107]. The GAs optimization process begins by setting a random set of individuals, each with an arbitrary fitness value. This population of individuals has a fixed size. Each individual is genetically represented by a chromosome string that holds a certain number of genes as illustrated in Figure 5.1. In fact each gene in the chromosome pertains to an optimization variable that influences the individual's fitness value. Each optimization variable is bounded by a minimum and a maximum value, forming a search range for the optimal solution(s). Note that the optimization variable value is encoded in bits of binary numbers within the chromosome string. The representation of the optimization target is crucial to the efficiency of the GAs. Increasing the number of bits for each gene results in a better resolution of the search range. A good representation makes the problem easier to solve; conversely, a poor representation does the opposite. The GAs operate in a manner that maximizes the fitness value of each individual at every generation, eventually leading to the fittest generation. The individual's fitness value is usually obtained from the individual's objective function value; thus if the objective function is misrepresented then the GAs will not

106

lead to the real fittest generation. As will discussed later, the GAs can operate to drive either a single-objective or a multi-objective optimization problem. The difference in the GA application for those two genre of optimization problems lies in the evaluation method of the individual fitness. In the case of a single-objective optimization, the fitness value is simply the value of whatever quantity to be maximized. For instance, if the single objective is to only minimize a certain quantity QNT, then the fitness value will be the inverse value of QNT. The fitness value of an individual in the case of a multi-objective optimization cannot be an explicit function of the multiple quantities to be maximized, rather it has to be determined via the aggregating function or the non-dominated sorting techniques. It is important at this stage to connote that a single-objective optimization leads to a unique optimal individual or solution whereas the multi-objective should lead to multiple solutions distributed on an optimal front known as the 'Pareto' front.
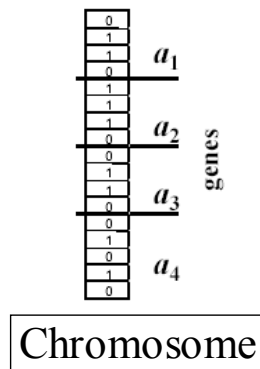
Figure 5.1: Example of an individual characterized by four parameters (genes) encoded in a chromosome [108].

In the course of their numerical work to detect sub-surface cavities, Divo et al. [108] gave a detailed explanation of the GAs functionality. They stated that the GAs rely on an iterative approach where each iteration represents a generation of individuals. At each iteration, the processes of selection, cross-over, and mutation operators are used to alter the individuals

optimization parameters such that each individual objective function is minimized. A selection operator is first applied to the population in order to determine and select the individuals that are going to pass information in a mating process with the rest of the individuals in the population. The probability of being a selected individual is calculated as the ratio of the individual's fitness function value to the sum of all the population individuals fitness function values. A weighted roulette wheel is then generated, where each individual of the current population is assigned a portion of the wheel in proportion to its probability of selection. The wheel is spun as many times as there are individuals in the population leading to the survival of the fittest individuals and the death of the worst ones. Upon the selection process, the mating or crossover process starts and it allows the genetic information contained in the best individuals to be combined to form offsprings. The probability of crossover is an important parameter that defines the expected population size of chromosomes which undergoes crossover operation. Additionally, a mutation operator randomly affects the information obtained by the mating of individuals for further improvement. The probability of mutation gives the expected number of mutated bits and every bit in all chromosomes in the whole population has an equal chance to undergo mutation. Following selection, crossover and mutation the new population is ready for its next evolution until a convergence criterion is reached. In summary, the GAs can be applied as follows,

1. INITIALIZE the generation $GEN(0)$

2. REPEAT

   a. Evaluate the Fitness of each individual in $GEN(i)$

   b. Select Parents from $GEN(i)$ based on their fitness as follows:

   Given the fitness of n individuals as $F_1, F_2, ..., F_n$. Then, select individual i with probability expressed in Equation (5.1).

$$p_i = \frac{F_i}{\sum_{j=1}^{n} F_i} \qquad (5.1)$$

This is often called the 'roulette wheel selection'.

c. Apply MATING operator to the selected parents.

d. Apply MUTATION operator to the newly-born individuals.

e. Replace parents by the newly-born individuals to produce generation $GEN(i+1)$

3. UNTIL no further optimal solution(s) is detected.

5.1.3 Multi-objective Evolutionary Optimization and Pareto-optimality

A general review of some of the most relevant research currently taking place in evolutionary multi-objective optimization can be found in the work of Coello [109]. In the optimization of most real world problems it is tedious to define all the aspects of interest in terms of a single objective. Defining those aspects in terms of multiple objectives offers more flexibility to the optimization procedure. In a single-objective optimization approach, only one global optimal solution is sought. In a multi-objective optimization approach, there are several possibly contradicting objectives to be optimized simultaneously. Hence, a multi-objective optimization will lead to a whole set of possible solutions of equivalent quality. The reason for the optimality of many solutions is that no one solution can be considered to be better than any other with respect to all the objective functions.

The solution of the multi-objective optimization problems is of the form:

$$minmize[f_1(x), f_2(x), ..., f_k(x)] \tag{5.2}$$

subject to the m inequality constraints:

$$g_i(x) \leq 0 \quad i = 1, 2, ..., m \tag{5.3}$$

and the p equality constraints:

$$h_i(x) = 0 \quad i = 1, 2, ..., p \tag{5.4}$$

where k is the number of objective functions f_i. $x=[x_1,x_2,...,x_n]$ is the vector of optimization variables. The ultimate goal is to determine the particular set of optimization variables that yields the optimum values of all the objective functions. The vector x is defined to be Pareto-optimal if there exists no feasible vector of optimization variables which would decrease some criterion without causing a simultaneous increase in at least one other criterion. The image of the Pareto-optimal vector of optimization variables is the so-called 'Pareto' front.

A straightforward approach to handling multiple objectives is the technique of aggregating functions. This technique relies on the combination of all the objectives into a single one using either an addition, multiplication or any other combination of arithmetical operations. An example of this approach is a linear sum of weights of the form:

$$min \sum_{i=1}^{k} w_i f_i(x) \tag{5.5}$$

where $w_i \geq 0$ are the weighting coefficients representing the relative importance of the k objective functions of our problem. It is usually assumed that:

$$\sum_{i=1}^{k} w_i = 1 \tag{5.6}$$

The usage of the aggregating function technique requires a prior knowledge of the relative importance among all the objective functions involved in the multi-objective optimization problem. Say that the design optimization of a certain component should meet three objectives: A, B, and C. If the relative importance among those objectives is such as $A : B : C = 6 : 3 : 1$, then the weighting coefficients should be assigned as follows: $w_A = 0.6$, $w_B = 0.3$, and $w_C = 0.1$. This technique is characterized by its simplicity as the objective has a single value and hence the fitness value can be easily determined by taking the inverse of the objective function value. The shortcoming of this technique however lies in the fact that the relative importance among all the objectives is not always known and hence assuming values for the weighting

coefficients becomes inaccurate. Besides, a mutli-objective optimization is primarily intended to provide a selection of optimal solutions where a trade-off space is accessible by the designer/analyst and the aggregating function technique is obviously incapable of doing so as it only converges to a single optimal solution. An enhancement of the aggregating function technique was offered by Gerace et al. [110], who demonstarted that a Pareto front can be generated by executing this technique multiple times where at each there is a different combination of the weighting coefficients. Although very accurate, the approach in [110] becomes inefficient when the optimization problem relies on time-consuming field variable solvers such as the full Navier-Stokes solvers.

An effective cure to the shortcomings of the aggregating function multi-objective technique is the non-dominated sorting approach to evaluate the fitness for individuals. The rationale of this approach is to assign a rank to each individual based on its dominance by the other individuals in the same generation [111]. The non-dominated sorting approach can be also applied to ranking fronts of individuals instead of single individuals where the rank of each front is determined based on it dominance by other fronts [112]. In the former individual ranking approach, the rank of an arbitrary individual is equal to a unity plus the number of individuals that dominate it; if for example an individual happens to be dominated by no other individuals, then its rank will be equal to 1. According to Hilbert [111], an individual A is said to dominate an individual B if, for at least one of the objectives, A is strictly more fit than B and if, for all other objectives, A is not less fit than B. Figure (5.2) shows a bi-objective optimization space where the goal is to minimize the values of two quantities QNT_1 and QNT_2 for 15 individuals at a given generation. The purpose of Figure (5.2) is to elucidate the rank evaluation for each individual in the generation; each of the 15 individuals is represented by a blue dot and with the individual's rank shown next to it. Looking at the individual X with the rank 9 in Figure (5.2), one can prominently identify the eight individuals that are strictly fitter than X (All those eight individuals have their QNT_1 and QNT_2 values lower than the QNT_1 and QNT_2 values of X).

Equation (5.7) reveals the multi-objective optimization fitness value expression for an individual i at an arbitrary generation consisting of $NIDV$ individuals.

$$F(i) = \frac{NIDV - Rank(i) + 1}{\sum\limits_{j=1}^{NIDV} (NIDV - Rank(j) + 1)} \tag{5.7}$$

If Equation (5.7) is applied on the individual X then the corresponding fitness will be equal to 0.044586. Conversely, if Equation (5.7) is applied to any of the individuals with the rank 1 then the corresponding fitness will be equal to 0.095541. By applying Equation (5.7), the selection probability of the individuals with the rank 1 will be higher than the selection probability of individual X. Thus, as the rank becomes lower the selection probability will become higher.

Eventually, the evolving population through many generations will lead to a front of individuals in the optimization space that represent the lowest combination of QNT_1 and QNT_2 values. This front is recognized as the "Pareto" Front and all the individuals on that front must have a rank of 1. The positive aspect of the Pareto front is that it enables the designer/analyst to choose among a bunch of optimal solutions (or designs) depending first on the feasibility of their optimization (or design) parameters and second on the comprise that should be done between the two (or more) quantities that needs to be maximized/minimized.
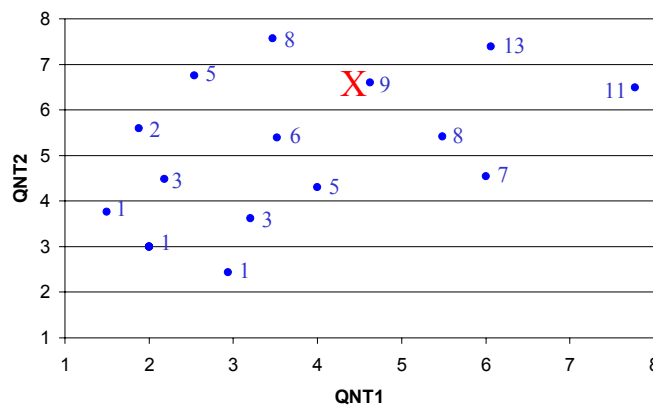
Figure 5.2: The ranking of a 15-individual generation in a bi-objective optimization space.

5.1.4 GA-based Shape Optimization Examples

The current sub-section reviews some of the prior GA-based shape optimization research activities with single and multiple objectives. To begin with, Divo et al. [113] coupled a GA to an acoustic boundary element method (BEM) numerical solver to optimize the shape of acoustic scattering bodies. To illustrate the functionality of the genetic algorithm in shape optimization, he presented an example where the shape of an acoustic scattering 'torpedo-like' object was optimized. The optimization was single-objective and served to minimize the acoustic intensity that is captured by a receiver located at a given distance from that scattering 'torpedo-like' object. Figure 5.3 displays the configuration of the 'torpedo-like' object including the optimization variables (cbl, hl, hr and cbr) that the genetic algorithm has to modify in order to reach an optimal configuration that yields a minimum value of the acoustic intensity on the receiver body. The optimal shape of the 'torpedo-like' object is presented in Figure 5.4. Annicchaiarico et al. [114] also coupled the BEM with the GA to find the optimal shape of a 2D cantilever beam and a 3D L-shaped structure. The geometry of those structural components was parameterized by the implementation of B-spline curves. The single goal of the shape optimization in [114] was to reduce the structure weights while not exceeding a maximum Von-Mises stress limit. Hamalainen.et al. [115] coupled a GA to a stabilized FEM laminar incompressible Navier-Stokes solver to optimize the shape of a flow divider shape; the single goal of this shape optimization application was to realize an equal division of the flow. Another interesting single-objective GA-based shape optimization example was carried out by Díaz Casás et al. [116]. The shape optimization in [116] was carried out for 2D airfoil profiles positioned along the span of 3D wind turbine blade. The optimization target was the maximization of the wind turbine efficiency. The efficiency of each individual was evaluated via a 'panel method' potential flow solver coupled with an 'integral boundary layer' to account for the viscous effects. The optimization parameters of the airfoil are the angle of attack, the chord length, and the NACA
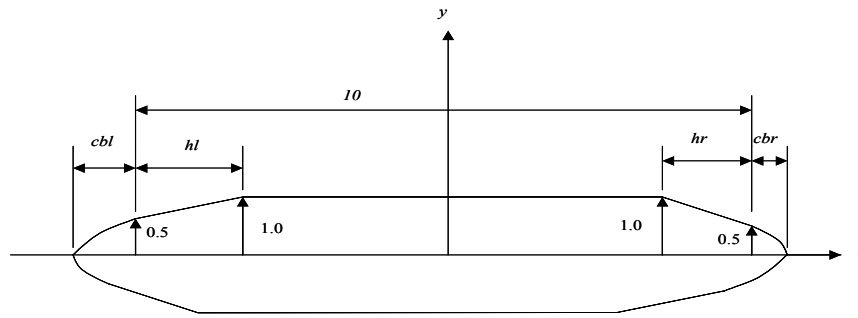
Figure 5.3: Generatrix of the 'torpedo-like' object showing the optimization variables [113].
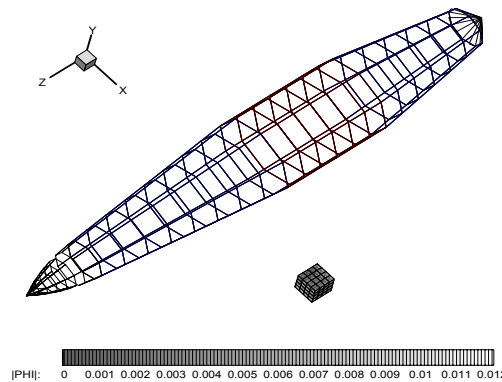
Figure 5.4: The torpedo GA-based optimal shape [113].

four digits family of profiles. After 1370 generations of global search, the authors in [116] were able to find a blade design that achieves an efficiency of 79.4%. In terms of multi-objective shape optimization problems, the rank-based non-dominated sorting approach of Marco [112] stands out. The multi-objective GA-based approach in [112] was first validated through some academic problems and then applied to optimize the shape of an airfoil in an inviscid Eulerian flow based on two objectives: first increase the lift at a subsonic Mach number of 0.2 and second decrease the drag at a transonic Mach number of 0.77. In addition to the single-objective optimization flow divider problem in [115], Hamalainen.et al. applied the individual-based non-dominated sorting multi-objective optimization approach to simultaneously minimize the drag and the electromagnetic backscatter of an airfoil while keeping sufficient lift; the flow Mach

number over that airfoil was 0.69 while the viscous effects were all accounted for in the turbulent boundary layer. Hilbert et al. [111] carried out the same multi-objective approach as in [115], however the FVM was employed to solve for the field variables. The shape optimization in [111] was carried out for a heat exchanger airfoils and the two objectives of this optimization were to maximize the heat flux across the airfoil surfaces while minimizing the flow pressure drop.

5.2 The ETSDA Shape Optimization Strategy

The reason underlying the use of the shape optimization genetic algorithm (SOGA) is to systemize the shape optimization procedure of the ETSDA. As mentioned early on, the current dissertation involves the ETSDA shape optimization based on controlling the undesirable hemodynamics patterns; a solid mechanics solver should be further appended to the SOGA whereby the compliance mismatch reduction can be embedded in the objective of the shape optimization. As the SOGA has an evolutionary basis, the ETSDA is analogized as an individual who is characterized by a set of design optimization variables. This section first elaborates on the composition of the SOGA objective function, then the geometric variability of all the considered ETSDA models is revealed, and finally a thorough description of the SOGA machinery as applied to the ETSDA is presented.

5.2.1 The Shape Optimization Objective Function

The shape optimization of the ETSDA models will be executed based on minimizing the undesirable hemodynamics parameters that are thought to be contributory to the IH growth. Each undesirable hemodynamics parameter will be represented by an objective function whose value depends on the ETSDA design optimization variables. In particular, the host artery floor is the

ETSDA area where the undesirable hemodynamics parameters will be minimized; essentially the undesirable hemodynamics patterns do occur at the suture line [16,45,41], nonetheless the findings in [6,7,117] indicate that the compliance mismatch contribution to the IH development is much more significant than the hemodynamics contribution. Thus the IH cause on the suture line would be best represented by the compliance mismatch rather than by the undesirable hemodynamics parameters and that will be left for future investigations.

As advised in the literature review chapter, the publications concerned with the IH development point towards low WSS, the oscillatory WSS, high SWSSG, and high TWSSG. Regarding the publications favoring the low and oscillatory shear theories [6,15,30,31,32,33,35,45,51], the authors withdrew their conclusions following two class of research methodologies. The first class consists of computational fluid dynamics (CFD) studies [32,33,51] and in-vitro experiments [30,31,45] to match up the locations of IH occurrence (the ETSDA floor, toe, and heel areas) and the WSS values at those same locations. The second class consists of in-vivo graft implant experiments [6,15,35] where regression analyses are carried out after the graft explantations to correlate the IH thickness to the WSS magnitude. The analyses in [6,15,30,31,32,33,35,45,51] offer an insight on what might be the IH hemodynamics root(s), yet they bank on a location correspondence observation between the IH sites and the WSS values at those sites. The fact of the matter is that those analyses offer too little as far as experimenting with the early biological response of the arterial wall to the ETSDA WSS values.

To understand the arterial wall biological response to hemodynamics, some researchers [36,37,38,40] have built in-vitro experiments in which the endothelium was exposed to irregular flow patterns similar to the ones that occur over the ETSDA host artery floor. The results from [36,37] show that high SWSSG values cause an endothelial proliferation and migration leading to a denudation of the endothelium. The results in [38] show that high values of the SWSSG also alters the re-generation of a denuded endothelium. The results in [40] emphasizes the great role of the high TWSSG values in inducing an endothelial proliferative response. To that end, the

high WSS spatial and temporal gradients were experimentally proven to initiate a direct damage to the endothelium more than the WSS does. Recall that the endothelium is the front shield of the arterial wall; hence once denuded, blood particles will infiltrate in the arterial wall and subsequently enhance the growth factors proven to lead to IH. Acknowledging the intact endothelial morphology of the host artery floor before the bypass surgery, it is more likely that high WSS gradients initiate the endothelial damage thereat rather than the WSS itself. The instantaneous SWSSG value is basically obtained by calculating the norm of the tangential traction vector gradient dotted by the tangential unit vector $\vec{t_g}$ [20]. The instantaneous TWSSG value is obtained from a first order backward temporal differentiation of the WSS at the corresponding pulsatile cycle instant. The expressions of the instantaneous SWSSG and TWSSG values are given in Equations (5.8) and (5.9) respectively.

$$\|SWSSG\| = \left\| (\vec{\nabla t}) \cdot \vec{t_g} \right\| \tag{5.8}$$

$$\|TWSSG\| = \frac{\partial (WSS)}{\partial t} \tag{5.9}$$

Two types of ETSDA shape optimization are carried out in the current dissertation. The first shape optimization type is single-objective where the steady-state SWSSG value is minimized assuming a steady Newtonian flow in the ETSDA geometry. The second shape optimization type is bi-objective where both the average SWSSG and TWSSG values are minimized given the flow pulsatility and the blood non-Newtonian rheology; the blood pulsatile cycle is denoted by T_{pulse}. The average SWSSG and TWSSG values are expressed in Equations (5.10) and (5.11).

$$\|SWSSG\|_{avg} = \frac{1}{T_{pulse}} \int_0^{T_{pulse}} \|SWSSG\| dt \tag{5.10}$$

$$\|TWSSG\|_{avg} = \frac{1}{T_{pulse}} \int_0^{T_{pulse}} \|TWSSG\| dt \tag{5.11}$$

Note that all the single/multi-objective minimizations of the WSS gradients will take place on the floor of the host artery where hemodynamics is the main cause of endothelial damage. More specifically, the WSS averaged spatial and temporal gradients will be minimized on the floor artery section situated across from the graft suture line; this floor artery section is referred to as the 'floor optimization section' and is shown in Figure (5.5).
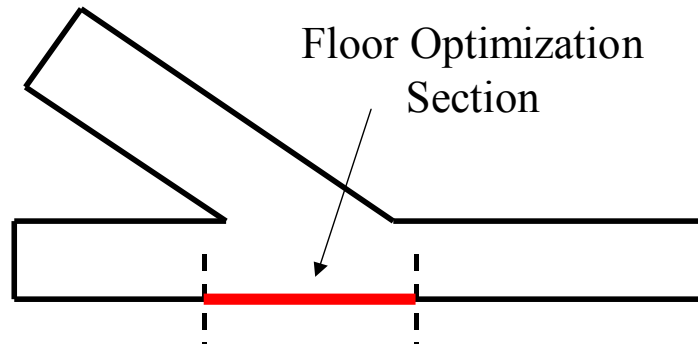
Figure 5.5: The floor optimization location in the ETSDA.

For the single-objective shape optimization, the objective function is equal to the L_2 norm of the steady-state SWSSG values at all the computational points on the floor optimization section. The L_2 norm expression of the single-objective function is taken over N_{BF} computational boundary points on the floor optimization section as illustrated in Equation (5.14).

$$f = \sqrt{\frac{1}{N_{BF}}\sum_{i=1}^{N_{BF}}\|SWSSG\|_{steady-state}} \qquad (5.12)$$

For the bi-objective shape optimization, the L_2 norms of the averaged SWSSG and TWSSG values will form the coordinate axes of a bi-objective optimization space, similar to the one shown in Figure (5.2), in which the Pareto optimality front is sought. The L_2 norm expressions of the two single-objective functions are taken over N_{BF} computational boundary points on the floor optimization section and are shown for the averaged SWSSG and TWSSG in Equations (5.13) and (5.14) respectively.

$$f_{SWSSG} = \sqrt{\frac{1}{N_{BF}} \sum_{i=1}^{N_{BF}} \|SWSSG\|_{avg}} \qquad (5.13)$$

$$f_{TWSSG} = \sqrt{\frac{1}{N_{BF}} \sum_{i=1}^{N_{BF}} \|TWSSG\|_{avg}} \qquad (5.14)$$

5.2.2. Geometric Variability of the ETSDA Models

The task of the SOGA is to constantly modify the values of the ETSDA design optimization variables such that the objective function(s) is/are constantly minimized throughout the evolutionary process. The ETSDA shape will be formally optimized as soon as the objective function(s) converge(s) to a minimal value(s), indicating the least damaging hemodynamics conditions to the endothelium. When modified, the design optimization variables would significantly affect the WSS gradients on the floor optimization section where IH favorably occurs. Those design optimization variables are subject to appropriate constraints that would be set by the vascular surgeons. Traditionally, those constraints involve the allowable ranges of the graft caliber and the anastomotic angle; they might also involve the amount of vein in the case of adding vein cuffs or patches to the ETSDA. Otherwise stated, each ETSDA design optimization variable falls into a search range limited by a maximum bound and a minimum bounds.

The set of design optimization variables for the conventional ETSDA model consists of two parameters: the anastomotic angle, β, and the graft caliber, D_{graft}. The search range for β is limited between 30° and 60°, whereas the search range for D_{graft} is limited between 4 (mm) and 6 (mm). The generatrix of the Direct ETSDA model is shown in Figure (5.6). The set of design optimization variables for the Miller Cuff ETSDA model consists of three parameters: the anastomotic angle, β, the graft caliber, D_{graft}, and the cuff height, H_{cuff}. The Cuff is made of a vein material that is interposed between the bypass graft and the host artery. The purpose of

using the Miller cuff is to reduce the compliance mismatch between the synthetic graft material and the biological material of the host artery. Reducing the compliance mismatch with the Miller Cuff have proven better post-operative performances of synthetic bypass grafts [26]. Similarly to the conventional ETSDA model, the search range for β is limited between 30° and 60°, and the search range for D_{graft} is limited between 4 (mm) and 6 (mm). Besides, the search range for H_{cuff} is set between 3 (mm) and 6 (mm). The generatrix of the Miller Cuff ETSDA model is shown in Figure (5.7). For the hood ETSDA model, we adapt a fixed diameter of 6 (mm) for the graft. Given a cut length of 15 (mm), the anastomosis shape variability only depends on the cubic spline defining the hood shape. The two end control points of the spline c_g and c_a are kept fixed, whereas the other two control points c_1 and c_2 are allowed to move within limited specified two-dimensional ranges. The ranges of motion for c_1 and c_2 are specified within a two-dimensional coordinate system representing the hood generatrix that is shown in Figure (5.8). Note that the hood ETSDA is similar to the Taylor Patch model shown in Figure (2.1a) but with a zero angle.
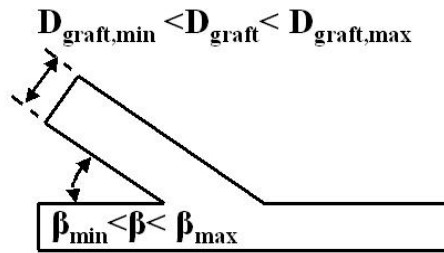
Figure 5.6: The conventional ETSDA model generatrix.
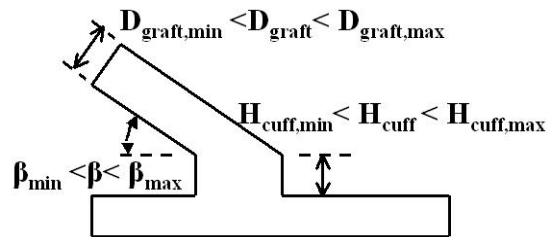
Figure 5.7: The generatrix of the Miller Cuff ETSDA model.
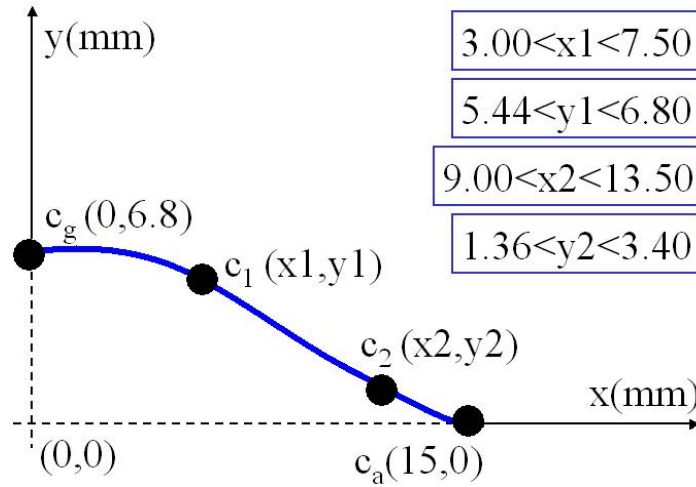
Figure 5.8: The generatrix of the hood ETSDA model.

5.2.3. The Information Passage Loop

The planned shape optimization process for the ETSDA consists of linking three main independent computational objects; the automated pre-processor, the LCMM solver, and the shape optimization genetic algorithm (SOGA). These three objects have to be coupled together through a loop called 'Information Passage Loop' or simply 'IPL'. This coupling consists of an iterative process by which the ETSDA geometry is modified at each iteration of the evolutionary process. Once the iteration process is converged, then the optimal ETSDA configuration(s) is/are attained. Figure (5.9) shows a detailed schematic for the IPL.

At the initial iteration, a population of ETSDA configurations are built and pre-processed in the automated pre-processor then sent to the meshless CFD solver to solve the blood flow. In the meshless CFD solver, the flow field within the ETSDA configurations is solved in an unsteady manner to account for the temporal variation of the flow at the inlet through the pulsatile cycle. At each time step of the pulsatile cycle, the averaged SWSSG and TWSSG L_2 norms are recorded at the floor optimization section. Following this, the averaged SWSSG and TWSSG L_2 norms are sent to the SOGA to evaluate the objective function(s).

121
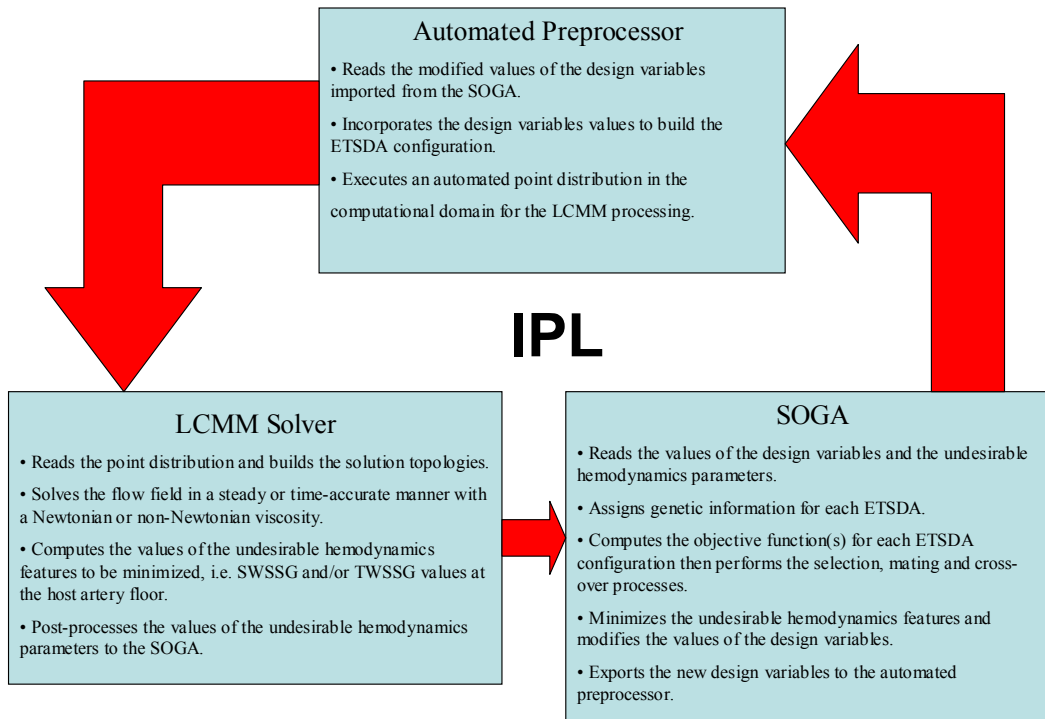
Figure 5.9: The mechanism of the information passage loop.

The single-objective or multi-objective function(s) is/are evaluated for each ETSDA configuration to determine its fitness value. Once the fitness value is determined for each individual, the selection process starts by evaluating the probabilities of selection. Once again, the more fitness an individual has the higher its probability of selection will be. After the most fit individuals are selected, the mating process is performed to genetically diversify the remaining population that has survived after the selection process. In the mating or cross-over process, a probability of cross-over is evaluated to specify the number of mating individuals who interchange the genetic information contained in their chromosomes. After the mating process, the newly-born individuals undergo a mutation process to further improve their genetic information. Following the mutation process, the SOGA yields the modified values of the design variables for every ETSDA configuration and then exports these variables to the automated preprocessor to build and distribute points in the new configurations. The newly-modified

population will then undergo a new iteration in the evolutionary optimization process. This process reiterates itself until convergence, i.e. the minimal SWSSG and TWSSG values, which imply the healthiest hemodynamics conditions for the host artery floor endothelium morphology.

5.3 The ETSDA Shape Optimization Results

The current section contains examples on the application of GA-based single- and multi-objective optimizations. The first set of examples entails the application of the SOGA single-objective version to optimize the conventional, Miller cuff, and hood ETSDA shapes assuming a steady anastomotic flow with a Newtonian viscous behavior. Then, a validation example is presented to demonstrate the accuracy of the individuals non-dominated sorting approach as applied for multi-objective optimizations. Once validated, the non-dominated sorting approach is incorporated in the SOGA to optimize the aforementioned ETSDA models shape taking into account the anastomotic flow pulsatility and the blood a non-Newtonian behavior.

5.3.1 Single-Objective ETSDA Shape Optimization

For all the single-objective GA-based ETSDA shape optimization cases, the jump and creep mutation probabilities are taken as 0.02 and 0.2 respectively. The fixed-size population at each generation consists of 34 individuals. Also, the host artery diameter is taken as constant and equal to 4 (mm) for all the three anastomotic models and the inlet volumetric flow rate is taken as 480 (ml/min) (corresponding to a graft-diameter-based Re number of 450).

The shape optimization of the conventional ETSDA model took 46 generations to spot the optimal solution. The objective function convergence for the conventional ETSDA model is shown in Figure (5.10). It is noted that each one of the objective function values displayed in Figure (5.10) pertains to the fittest individual found in the corresponding generation. The shape

optimization process for the conventional ETSDA model resulted in a β optimal value of 30.7059° and a D_{graft} optimal value of 5.9686 (mm). In order to illustrate the gain achieved by the conventional ETSDA shape optimization, we plot in Figure (5.11) the SWSSG values on the floor optimization sections of both the current optimized shape and a typical shape considered for optimization. We choose the typical shape with the following design variables: β=45° and D_{graft}=6 (mm). Although both SWSSG plots in Figure (5.11) exhibit similar trends, notice that the red curve (corresponding to the standard shape) was lowered to the level of the blue curve (corresponding to the optimal shape) thanks to the shape optimization process.

Regarding the Miller Cuff ETSDA model, the optimal shape was found after 12 generations as it is apparent from the objective function convergence path in Figure (5.12). The β optimal value was found as 32.9412° and the D_{graft} optimal value was found as 5.9059 (mm). Also, the optimal H_{cuff} value was found to be equal to 3.0588 (mm). Again, to illustrate the gain achieved by the Miller cuff ETSDA shape optimization, we plot in Figure (5.13) the SWSSG values on the floor optimization sections of both the current optimized shape and a selected typical shape considered for optimization. We choose a Miller ETSDA typical shape with the following design variables: β=45°, D_{graft}=6 (mm) , and H_{cuff}= 3 (mm).

The hood ETSDA model shape optimization took 54 generation for convergence; the SOGA predicted [x1=3.4235 (mm) , y1=6.384 (mm)] as optimal coordinates for the control point c_1 and [x2=11.2588 (mm) , y2=1.656 (mm)] as optimal coordinates for the control point c_2. The convergence of the objective function for the hood ETSDA shape optimization is displayed in Figure (5.14). A non-optimal hood ETSDA shape is picked with the following coordinates of the moving control points: [x1=3.0 (mm), y1=5.44 (mm), x2=12.75 (mm), y2=1.36 (mm)]. Plots of the SWSSG on the host artery floor of both the non-optimal and the optimized hood ETSDA models are shown in Figure (5.15). The narrow modification from the non-optimal hood ETSDA shape to the optimized hood ETSDA shape justifies the slight drop in the SWSSG values in Figure (5.15).
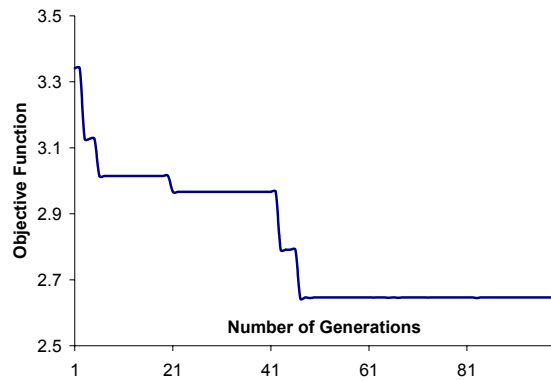
Figure 5.10: The objective function minimization for the conventional ETSDA model.
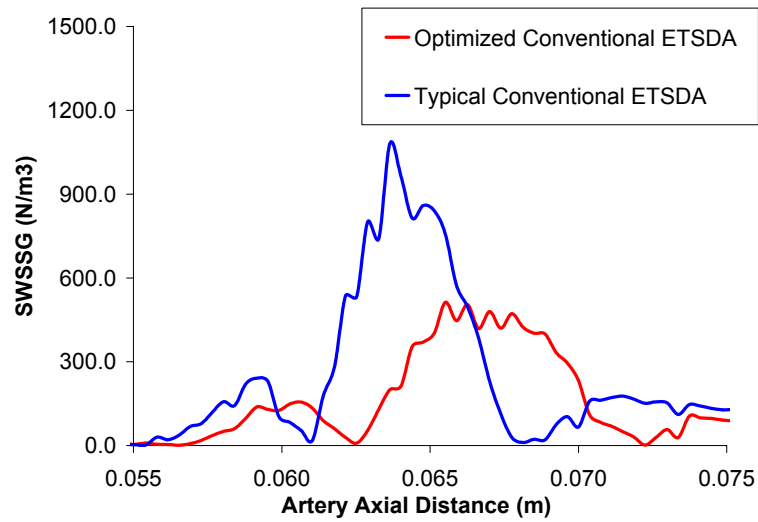
Figure 5.11: SWSSG plots for the typical and optimized conventional ETSDA models.
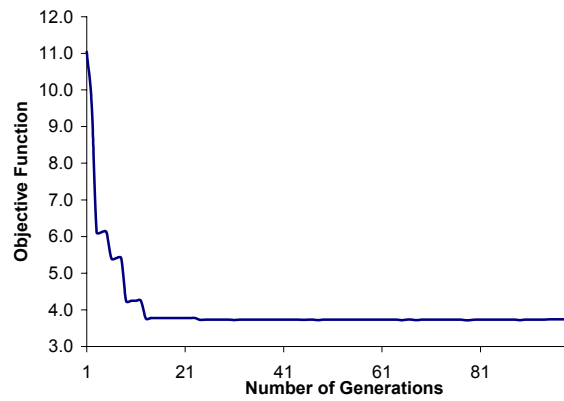
Figure 5.12: The objective function minimization for the Miller Cuff ETSDA model.

125
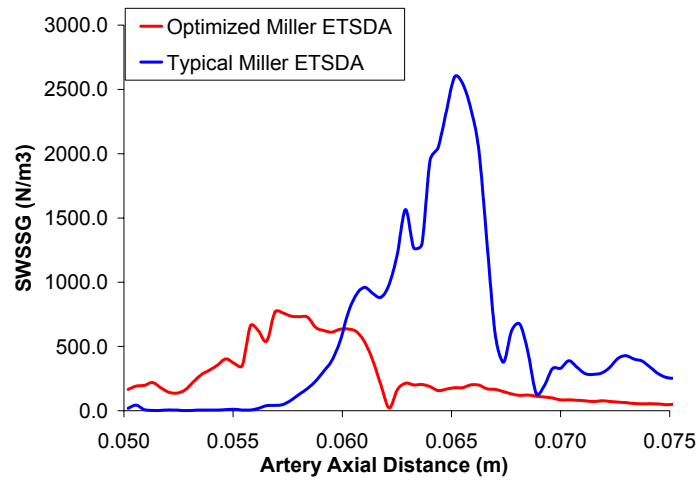
Figure 5.13: SWSSG plots for the typical and optimized Miller Cuff ETSDA models.
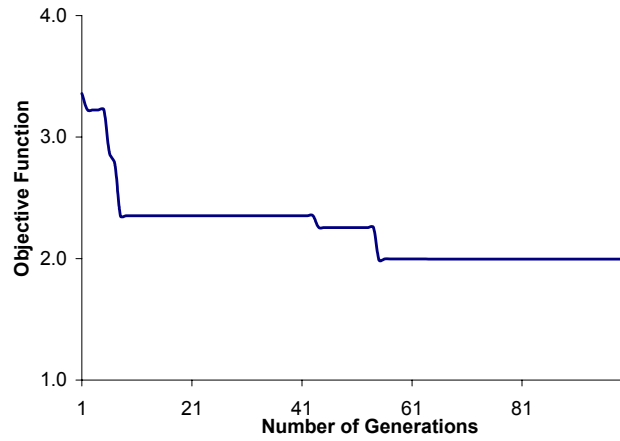
Figure 5.14 : The objective function minimization for the hood ETSDA model.
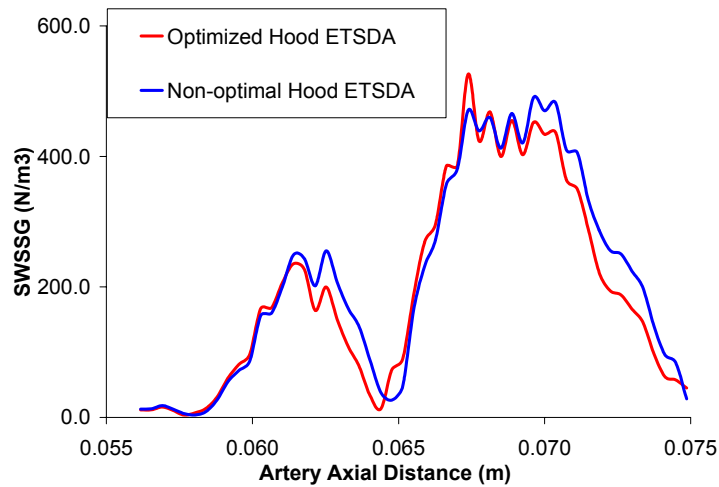
Figure 5.15: SWSSG plots for the non-optimal and optimized hood ETSDA models.

126

The main purpose of the current single-objective shape optimization application was to prove the successful communication between three different computational objects: the automated pre-processor, the meshless CFD solver and the SOGA. However this single-objective application is inadequate in terms of medical relevance. A more realistic shape optimization should also invoke the TWSSG in the objective function once the meshless solver is capable of handling pulsatile flows.

5.3.2 Validation of the Non-dominated Sorting Approach

Consider the following two-objective functions optimization problem involving two optimization parameters x and y; this problem was previously employed as a benchmark by Marco et al. [112] in their non-dominated sorting front ranking approach. The optimization goal of this problem is to simultaneously minimize the value of two functions f_1 and f_2 that are given in Equations (5.15) and (5.16) respectively.

$$f_1(x,y) = (x-1)^2 + (y-3)^2 \tag{5.15}$$

$$f_2(x,y) = (x-4)^2 + (y-2)^2 \tag{5.16}$$

with $(x,y) \in [-5,5] \times [-5,5]$ forming the relevant search range.

The Pareto front for this optimization problem can be analytically retrieved by combining $f_1(x,y)$ and $f_2(x,y)$ into a parametric single function $f(x,y)$ and then minimizing this function with respect to both x and y. The parametric expression of $f(x,y)$ is given in Equation (5.17) where w_p is a weighting coefficient that balances between $f_1(x,y)$ and $f_2(x,y)$.

$$f(x,y) = w_p f_1(x,y) + (1-w_p)f_2(x,y) \tag{5.17}$$

with $w_p \in [0,1]$. Taking the zero gradient of $f(x,y)$ with respect to both x and y leads to the following parametric optimal solutions: $x_{opt} = 4 - 3w_p$ and $y_{opt} = 2 + w_p$. By assigning a fine resolution of w_p within the $[0,1]$ range and incorporating the corresponding x_{opt} and y_{opt} values

127

in Equations (5.15) and (5.16), the analytical Pareto front can be recovered as illustrated in Figure (5.17) where the values of $f_1(x_{opt}, y_{opt})$ and $f_2(x_{opt}, y_{opt})$ will be bounded in a $[0, 10]$ range; this analytical front will be used as a benchmark to the front that will be determined by the current non-dominated sorting approach for individuals. Following the analytical solution of the Pareto front, the non-dominated-sorting-based GA is implemented on a population of 30 individuals evolving through 100 generations. Figure (5.16) reveals the bi-objective minimization space for $f_1(x, y)$ and $f_2(x, y)$; the blue dots represent all the 3000 individuals that have evolved through 100 generations and the red dots pertain to the optimal individuals that constitute the Pareto front. The search eventually identified 189 optimal individuals on the Pareto front. Notice that each optimal individuals minimizes one objective function more than the other and this what enables the user/analyst to make a trade-off between the minimal values of $f_1(x, y)$ and $f_2(x, y)$ before choosing a unique final optimal solution. Moreover, for some optimal values on the front, the design might be simply unfeasible and then the user/designer can always pick another optimal solution that allows a feasible design. In an ideal case where an optimal solution on the front equally minimizes the two objective functions (or all the objective functions for a more general optimization problem), then the point that represents this optimal solution on the Pareto front will be known as the "Utopia" point. The validity of the non-dominated sorting approach is indicated in Figure (5.17) as the computed Pareto Front completely matches with the analytical one. To this end, the non-dominated-sorting-based GA may be safely coupled to the LCMM solver to perform shape optimizations.

5.3.3 Bi-Objective ETSDA Shape Optimization

For all the bi-objective GA-based ETSDA shape optimization cases, the jump and creep mutation probabilities are both equal to 0.25. The reason that the bi-objective optimization mutation probabilities values are higher than the ones for the single-objective optimization is to
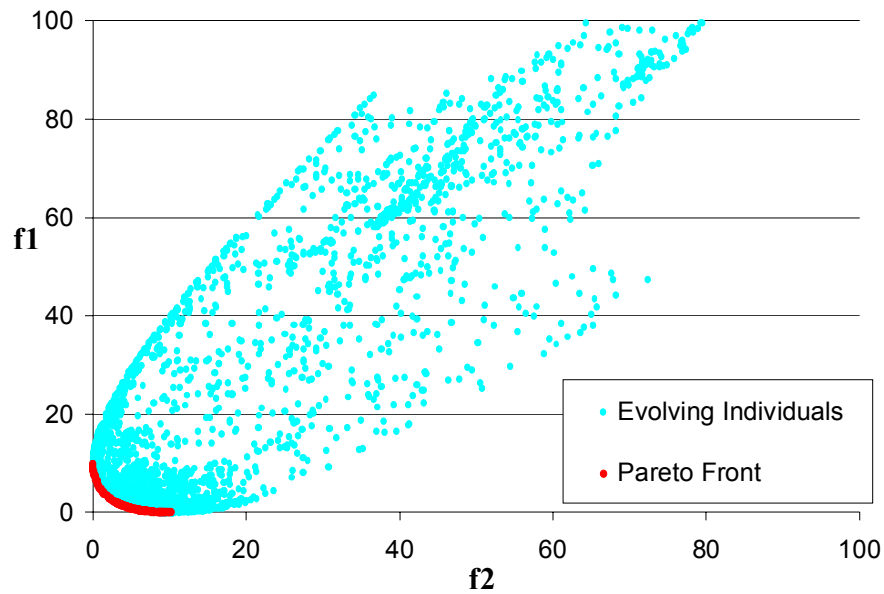
Figure 5.16: The bi-objective optimization space with the all evolving individuals.
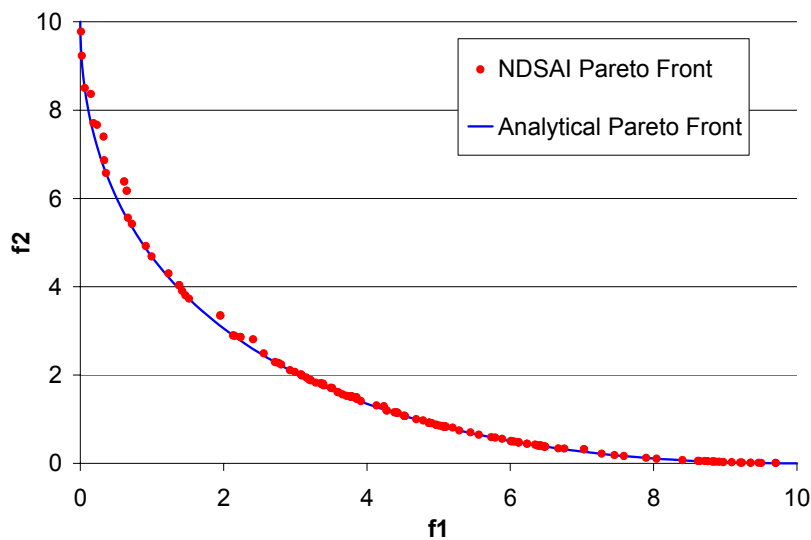
Figure 5.17: The matching between the analytical Pareto front and the non-dominated-sorting-computed one.

promote the genetic diversity of the evolving individuals and eventually capture a wider Pareto front with more optimal solutions. Besides, the population fixed-size (34 individuals in each generation) for all the ETSDA models (conventional, Miller cuff, and hood) design optimization

129

variables are the same ones for the prior ones in the single-objective optimization examples. Similarly to the single-objective cases, the host artery diameter is taken as constant and equal to 4 (mm) for all the three anastomotic models. The pulsatile volumetric flow rate shown in Figure (4.37) is applied at the graft inlet and 80% of the flow exists the host artery distally whereas the other 20% exists from the proximal side just as illustrated in Figure (4.56). The 80:20 outflow proportion is assumed to remain constant throughout the pulsatile cycle.

With respect to the conventional ETSDA model, the Pareto front was recovered after a 30 generation evolutionary global search and is shown in Figure (5.18); the red dots (there is 6 of them) in this figure represent the optimized shapes forming the Pareto front while the cyan dots (there is 1020 of them in the whole bi-objective optimization space) represent all the individuals design that were evaluated during the evolutionary process. The 6 optimal solutions on the Pareto front are all listed in Table (5.1). Figure (5.19) illustrates the averaged WSS spatial and temporal gradient minimization achieved by the current optimization; the SWSSG and TWSSG averaged values are plotted for two selected optimized shapes [β_{op1}=35.3°, $D_{graft,op1}$=5.983 mm,β_{op2}=30.0°, $D_{graft,op2}$=5.92 (mm)] and a typical shape [β_{typ}=45° and $D_{graft,typ}$=5 (mm)]. Note that both the averaged SWSSG and TWSSG are best minimized when the graft caliber is maximal [about 6 (mm)], however only the averaged SWSSG is best minimized when the anastomotic angle is minimum with a 30° value.

Table 5.1: The conventional ETSDA optimal parameters and objective function values.

SWSSG L2 Norm (N/m3)	TWSSG L2 Norm (N/sec.m2)	Graft Caliber (mm)	Anastomotic Angle (deg)
149.8	0.2660	0.005983	35.30
145.8	0.2761	0.005984	32.90
145.0	0.2809	0.005981	32.84
146.0	0.2752	0.005984	32.87
147.9	0.2706	0.005920	30.00
145.9	0.2759	0.005984	32.90
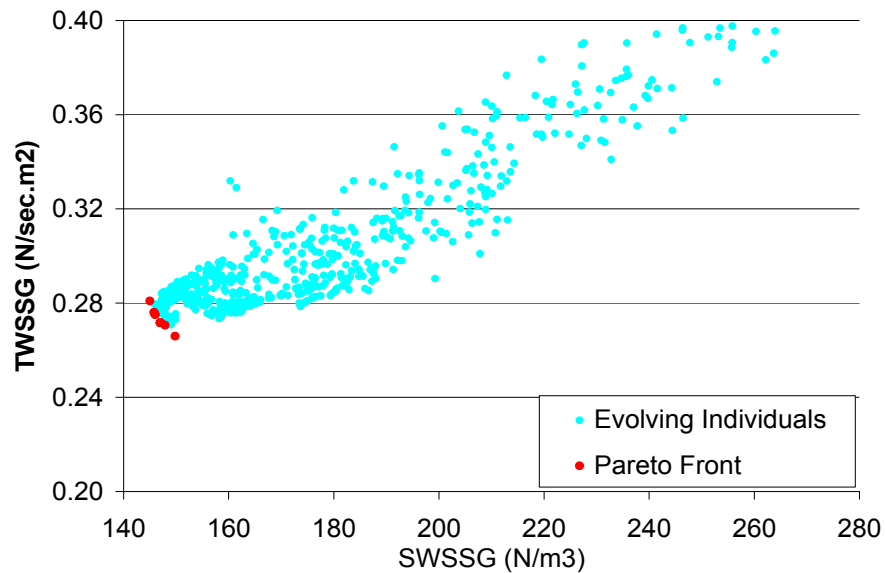
Figure 5.18: The Pareto Front for the conventional ETSDA multi-objective shape optimization.
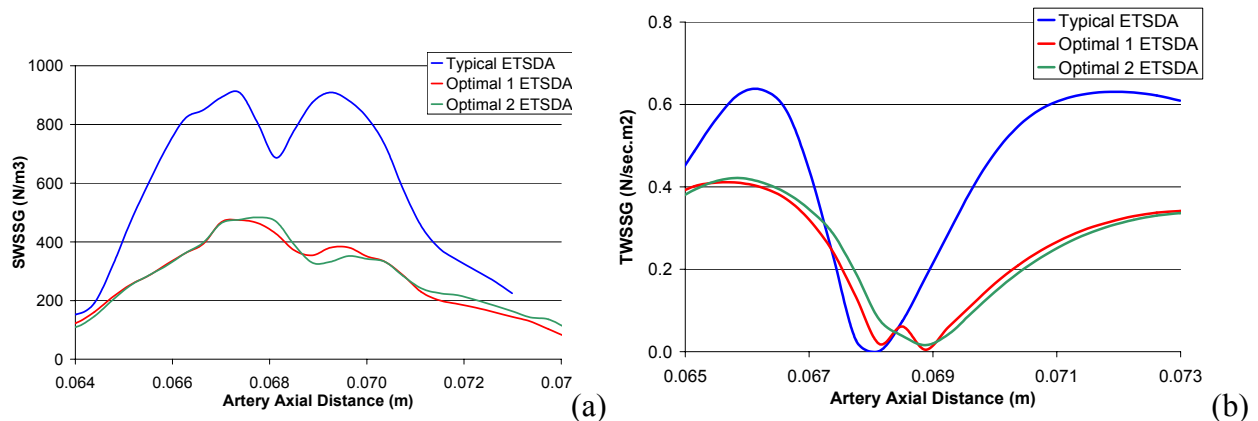
Figure 5.19: SWSSG (a) and TWSSG (b) plots for the typical and the two selected optimized conventional ETSDA models.

Regarding the Miller Cuff ETSDA model, the Pareto optimality front recovered after a 30 generations evolutionary global search and is shown in Figure (5.20); again, the red dots (there is 12 of them) in this figure represent the optimized shapes forming the Pareto front while the cyan dots (there is 1020 of them in the whole bi-objective optimization space) represent all the individuals design that were evaluated during the evolutionary process. The 12 optimal solutions on the Pareto front are all listed in Table (5.2). Figure (5.21) illustrates the averaged

131

WSS spatial and temporal gradient minimization achieved by the current optimization; the SWSSG and TWSSG averaged values are plotted for two selected optimized shapes [β_{op1}=49.33° , $D_{graft,op1}$=5.93 (mm) , $H_{cuff,op1}$=3.55 (mm) , β_{op2}=30.1° , $D_{graft,op2}$=5.96 (mm) , $H_{cuff,op2}$=3.65 (mm)] and for a typical shape [β_{typ}=45° , $D_{graft,typ}$=5 (mm) , $H_{cuff,typ}$=4.5 (mm)]. As observed in the conventional ETSDA bi-objective shape optimization, the averaged SWSSG and TWSSG are best minimized when the graft caliber is maximal [about 6 (mm)]. Also, it is observed that the averaged SWSSG would be best minimized with both the smallest anatomotic angle and the smallest cuff height. On the other hand, it seems that increasing the anastomotic angle and the cuff height would help minimizing the averaged TWSSG.

The hood ETSDA model Pareto front recovered after a 30 generations evolutionary global search and is shown in Figure (5.22); once more, the red dots (there is 14 of them) in this figure represent the optimized shapes forming the Pareto front while the cyan dots (there is 1020 of them in the whole bi-objective optimization space) represent all the individuals design that were evaluated during the evolutionary process. The 14 optimal solutions on the Pareto front are all listed in Table (5.3). Figure (5.23) illustrates the averaged WSS spatial and temporal gradients minimization achieved by the current optimization; the SWSSG and TWSSG averaged values are plotted for two selected optimized hood ETSDA shapes and a random non-optimal hood ETSDA shape. The spline control point coordinates for the two selected optimized shapes are [x1=5.79 (mm), y1=6.7592 (mm), x2=12.68 (mm), y2=3.3252 (mm)] and [x1=3.81 (mm), y1=5.888 (mm), x2=11.811 (mm), y2=1.91352 (mm)]; the spline control point coordinates for the non-optimal shape are [x1=3.0 (mm), y1=5.44 (mm), x2=12.75 (mm), y2=1.36 (mm)]. The averaged SWSSG and TWSSG are best minimized when the graft caliber is maximal (about 6 (mm)). Also Note only the averaged SWSSG is best minimized when the anastomotic angle is minimum with a 30° value.

Table 5.2: The Miller cuff ETSDA optimal parameters and objective function values.

SWSSG L2 Norm	TWSSG L2 Norm	Graft Caliber	Anastomotic Angle	Cuff Height
(N/m3)	(N/sec.m2)	(m)	(deg)	(m)
148.2000	0.2737	0.0060	34.5600	0.0034
142.6000	0.2886	0.0060	30.5800	0.0032
144.0000	0.2836	0.0060	30.3200	0.0033
149.6000	0.2733	0.0059	30.5700	0.0031
143.7000	0.2843	0.0060	30.1000	0.0037
145.2000	0.2750	0.0059	30.5300	0.0036
155.3000	0.2707	0.0059	37.8400	0.0038
175.1000	0.2556	0.0059	49.3300	0.0036
163.3000	0.2644	0.0059	39.9500	0.0035
173.3000	0.2597	0.0059	49.3100	0.0036
179.6000	0.2531	0.0059	51.4200	0.0037
157.1000	0.2678	0.0059	38.1800	0.0035
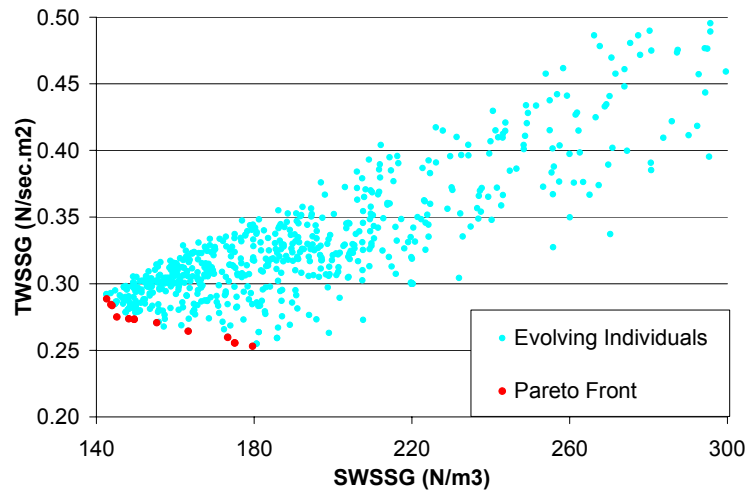
Figure 5.20: The Pareto Front for the Miller cuff ETSDA multi-objective shape optimization.
(a)(b)
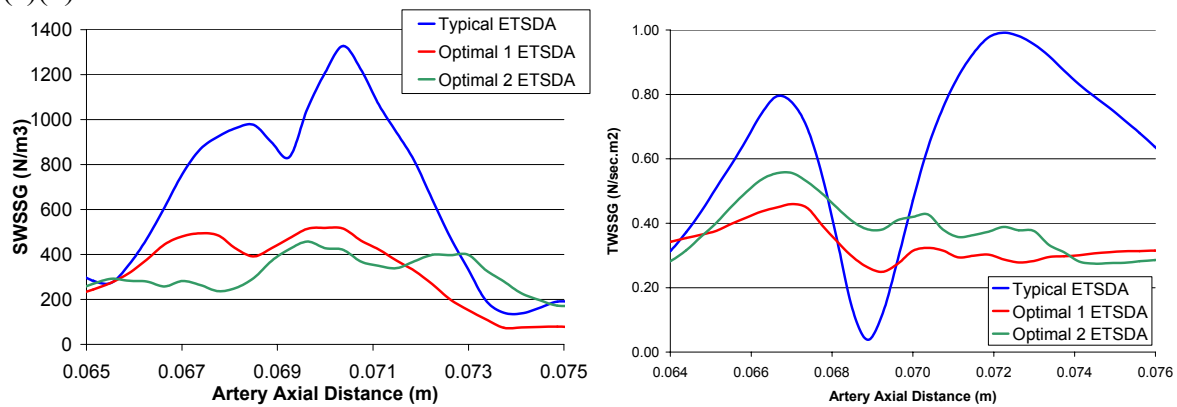
Figure 5.21: SWSSG (a) and TWSSG (b) plots for the typical and the two selected optimized Miller cuff ETSDA models.

Table 5.3: The hood ETSDA optimal parameters and objective function values.

| SWSSG L2 Norm	TWSSG L2 Norm	x1	y1	x2	y2
(N/m3)	(N/sec.m2)	(m)	(m)	(m)	(m)
133.9000	0.2852	0.0038	0.0059	0.0118	0.0019
126.9000	0.2927	0.0057	0.0067	0.0135	0.0030
125.7000	0.2962	0.0056	0.0067	0.0126	0.0034
125.4000	0.2968	0.0056	0.0068	0.0129	0.0032
125.4000	0.2967	0.0056	0.0068	0.0129	0.0032
126.2000	0.2951	0.0059	0.0067	0.0133	0.0030
126.7000	0.2941	0.0054	0.0067	0.0131	0.0032
123.9000	0.2989	0.0065	0.0067	0.0126	0.0027
124.7000	0.2985	0.0062	0.0065	0.0118	0.0029
123.5000	0.2996	0.0066	0.0067	0.0122	0.0026
130.3000	0.2893	0.0073	0.0057	0.0134	0.0027
128.4000	0.2902	0.0060	0.0066	0.0135	0.0033
125.0000	0.2983	0.0065	0.0067	0.0130	0.0028
125.3000	0.2973	0.0058	0.0068	0.0127	0.0033
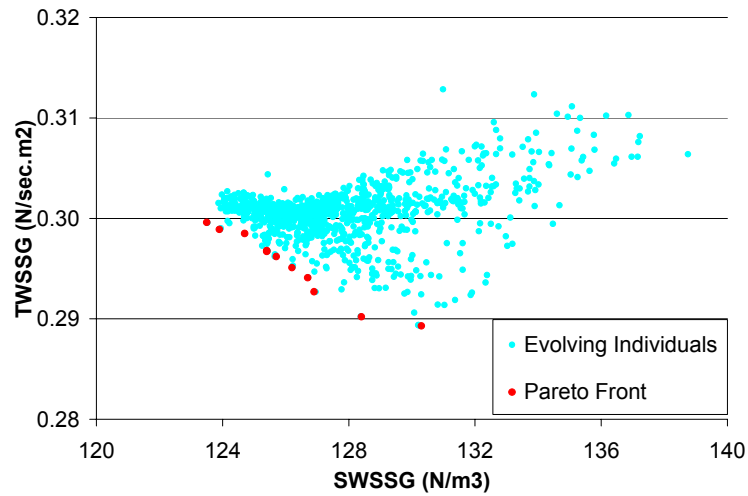
Figure 5.22: The Pareto Front for the hood ETSDA multi-objective shape optimization.
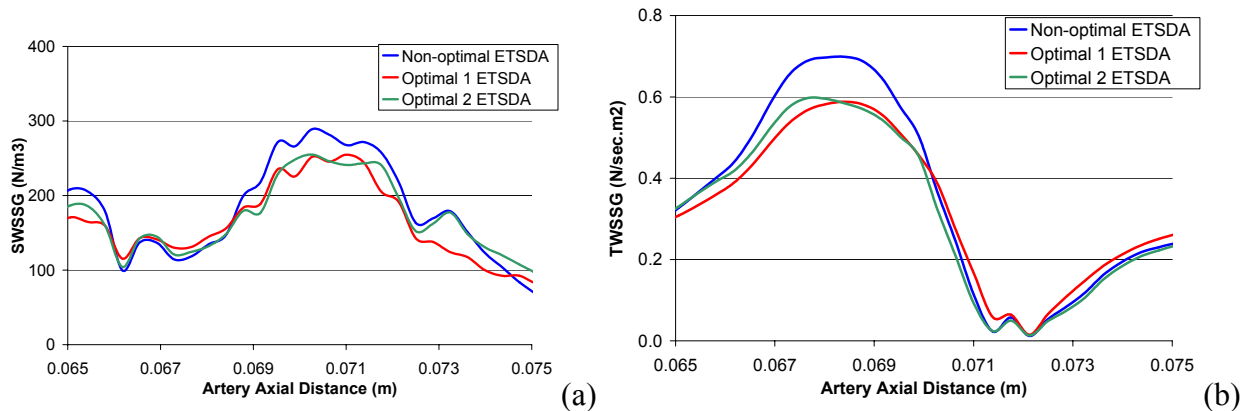
Figure 5.23: SWSSG (a) and TWSSG (b) plots for the non-optimal and the two selected optimized hood ETSDA models.

5.4 The ETSDA Shape Optimization Discussion

On the ground of the previous section findings, it seems that the proposed GA-based shape optimization approach would greatly improve the flow conditions on the host artery floor of both the conventional and the Miller cuff ETSDA models. Contrarily, the enhancement of the flow conditions on the hood ETSDA host artery floor would slightly benefit from the current GA-based shape optimization approach. To this end, the optimization of the hood shape in the hood ESTDA model does sound to be worthy as not much change will happen to the abnormal hemodynamics parameters on the host artery floor. As will be discussed in the sequel, the anastomotic angle and the graft caliber are the two major optimization design variables having impact on the floor of the ETSDA host artery.

In the single-objective shape optimization of the conventional ETSDA model, the typical model steady-state SWSSG on the host artery floor has been reduced by 31.67% with the 30.7059° angle and the 5.9686 (mm) graft caliber optimized shape. In the bi-objective shape optimization of the conventional ETSDA model, the typical model averaged SWSSG and averaged TWSSG on the host artery floor have been respectively reduced by 57.7% and 34.48% with the $[\beta_{op1}=35.3°$, $D_{graft,op1}=5.98$ (mm)] optimized shape and by 60.17% and 33.56% with the $[\beta_{op2}=30.0°$, $D_{graft,op2}=5.92$ (mm)] optimized shape. Besides, in the single-objective shape optimization of the Miller cuff ETSDA model the typical model steady-state SWSSG on the host artery floor has been reduced by 53.79% with the 32.9412° angle, 5.9059 (mm) graft caliber, and 3.0588 (mm) cuff height optimized shape. In the bi-objective shape optimization of the Miller cuff ETSDA model the typical model averaged SWSSG and averaged TWSSG on the host artery floor have been respectively reduced by 45.3% and 34.77% with the $[\beta_{op1}=49.33°$, $D_{graft,op1}=5.93$ (mm) , $H_{cuff,op1}=3.55$ (mm)] optimized shape and by 47.73% and 26.9% with the $[\beta_{op2}=30.1°$, $D_{graft,op2}=5.96$ (mm) , $H_{cuff,op2}=3.65$ (mm)] optimized shape. In regards to the single-objective shape optimization of the Hood ETSDA model, the non-optimized model

steady-state SWSSG on the host artery floor has been reduced by 7.14% with the [x1=3.4235 (mm) , y1=6.384 (mm) , x2=11.2588 (mm) , y2=1.656 (mm)] optimized shape. Then, in the bi-objective shape optimization of the hood ETSDA model the non-optimized model averaged SWSSG and averaged TWSSG on the host artery floor have been respectively reduced by 8.43% and 5.69% with the [x1=5.79 (mm), y1=6.7592 (mm) , x2=12.68 (mm), y2=3.3252 (mm)] optimized shape and by 4.82% and 8.98% with the [x1=3.81 (mm), y1=5.888 (mm), x2=11.811 (mm) , y2=1.91352 (mm)] optimized shape.

With respect to the conventional and the Miller-cuff ETSDA models, one can draw a confident conclusion that the graft caliber plays a very important role in mitigating the abnormal hemodynamics on the floor of the ETSDA host artery. This conclusion is illustrated from the bi-objective shape optimization data reported in Table (5.1) for the conventional ETSDA model and in Table (5.2) for the Miller cuff ETSDA model; it is noted that in those two tables all the optimized ETSDA shapes have a graft caliber value that is at the 6 (mm) maximum limit of the search range regardless of whether the averaged SWSSG or the averaged TWSSG is best minimized. Above this, the single-objective ETSDA shape optimization has demonstarted that the steady-state SWSSG is best minimized by the increasing the graft caliber. This observation on the graft caliber in improving the hemodynamics conditions in the ETSDA has been extended by many investigators throughout the literature [15,17,19,118,119]. The in-vitro and in-vivo results of Keynton et al. [15] show that increasing the graft caliber indeed reduces the SWSSG on the host artery floor and also yields a lower intimal thickness threat. Also, Lei et al. [17] proved via their numerical simulation that increasing the graft caliber significantly mitigates the SWSSG on the floor of the host artery. Similarly, O'Brien et al. [19] noticed through their numerical simulation shape optimization work that increasing the graft caliber lessens the abnormal hemodynamics patterns on the floor of the host artery. Also Qiao et al. [118] demonstarted in their CFD analysis that the increasing the graft caliber lowers the SWSSG on the floor of the ETSDA host artery floor. Abbott et al. [119] observations indirectly support the

argument of increasing the graft caliber after they remarked that larger caliber grafts lead to a higher success rate for the above-knee bypass procedures.

As far as the optimal choice of the anastomotic angle, both the averaged SWSSG and averaged TWSSG are competing for an optimal value on the Pareto front in the event of the bi-objective ETSDA shape optimization. This competition is mild in the case of the conventional ETSDA where the averaged SWSSG is best minimized with the 30° angle while the averaged TWSSG is best minimized with the 35.3° one. In the case of the Miller cuff ETSDA, the competition for the optimal angle is apparently higher as evidenced in Table (5.1) and in Table (5.2). It is prominent that the averaged SWSSG is best minimized by decreasing the angle all the way to the 30° minimum limit of the search range whereas the averaged TWSSG is best minimized by increasing the angle up to a value of 51.42°. In the case of a single objective ETSDA shape optimization, having the anastomotic near the lower limit of the search range would substantially reduce the steady-state SWSSG values on the host artery floor. The anastomotic angle effect on the ETSDA flowfield has been thoroughly studied by several researchers in the literature [46,47,48,19]. In line with the current GA-based angle optimization interpretation, Ojha et al. [46] opined that the angle reduction would mitigate the host artery floor hemodynamics patterns possibly related to the IH development. Fei et al. [47] had a very similar observation as he proposed that bypass grafts should be implanted with a minimal distal anastomotic angle. The present single-objective ETSDA shape optimization results are backed by the steady-flow in-vitro work of Wijesinghe et al. [48] who proved that decreasing the anastomotic angle would dampen the flow recirculation in both conventional and Miller cuff ETSDA geometries. Furthermore, O'Brien et al. [19] demonstarted that decreasing the anastomotic angle would mitigate the abnormal hemodynamics on the host artery floor.

Considering the single-objective ETSDA shape optimization of the Miller cuff ETSDA model, the steady-state SWSSG is best minimized with a cuff height near the 3 (mm) lower limit of the search range. Concerning the bi-objective ETSDA shape optimization of the Miller cuff

ETSDA model, all the optimal solutions existing on the Pareto front have a cuff height value ranging between 3.2 (mm) and 3.7 (mm). This suggests that the Miller cuff height should be considerably minimized. The current observation made about the Miller cuff height is endorsed by the results of Wijesinghe et al. [48] who, in addition to their observation on the anastomotic angle, demonstarted that increasing the cuff height would enlarge the flow recirculation in the Miller cuff ETSDA geometry. In contrast with the present findings, Fisher et al. [18] hinted that increasing the cuff height is favorable as it sustains a washout vortex in the cuff cavity that prevents low WSS values. They nevertheless ignored the fact that sustaining the vortex will lead to a high SWSSG on the host artery floor. Keeping in mind the direct endothelial damage caused by the high SWSSG caused by a sustained vortex, the Miller cuff should be lowered.

An interesting observation that has been prompted from the current shape optimization study is the relative performance of the three considered ETSDA models. The hood ETSDA model is superior to the conventional and the Miller cuff ETSDA models as far as the time-average SWSSG low values on the host artery floor. Figures (5.24) and (5.25) show the floor time-average SWSSG distribution for all the ETSDA models typical/non-optimal and optimized designs. The low time-average SWSSG values are attributed to the fact the flow impingement on the floor is substantially mitigated by the zero-angle between the graft and the host artery. The existence of the anastomotic angle in the conventional and Miller cuff ETSDA models lead to relatively stronger flow impingement on the floor and hence high spatial gradients of the WSS. On the other hand, the hood ETSDA model does not present a significant advantage over the other two models in regard to the time-averaged TWSSG. Figures (5.26) and (5.27) show the floor time-average TWSSG distribution for all the ETSDA models typical/non-optimal and optimized designs. The hood ETSDA model zero anastomotic angle leads to a greater motion of the floor stagnation point and this in turn lead to higher TWSSG values; the existence of an anastomotic angle in the conventional and Miller Cuff ETSDA models tend to actually lower the TWSSG values.
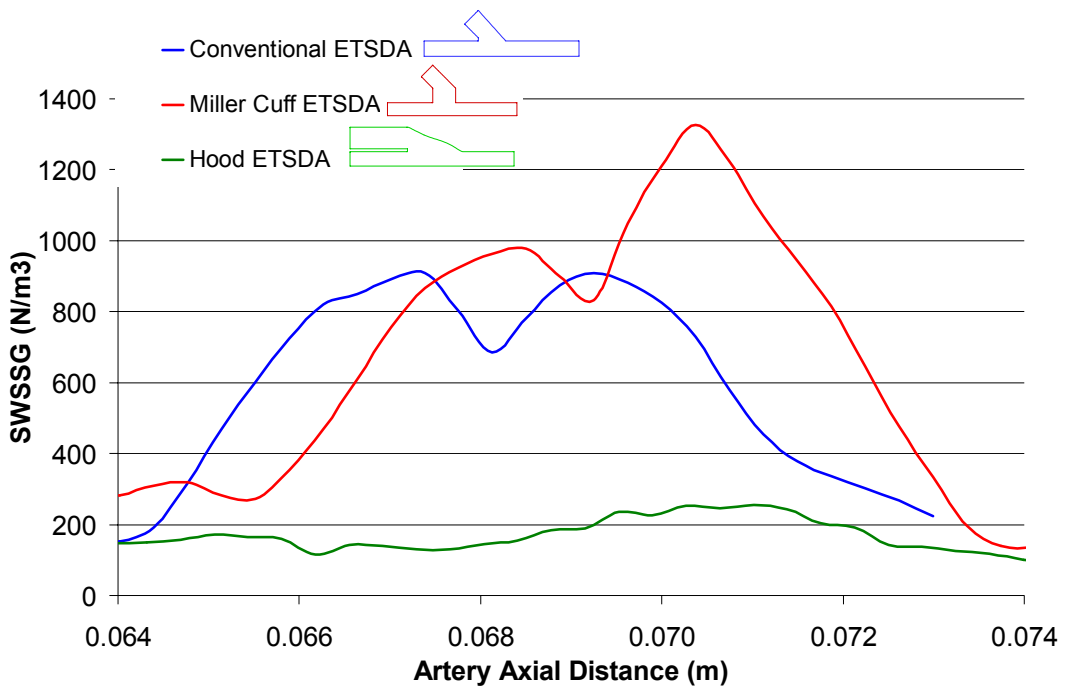
Figure 5.24: Floor time-average SWSSG resulting from the hemodynamics in the typical/non-optimal shapes of the conventional, Miller cuff, and hood ETSDA models.
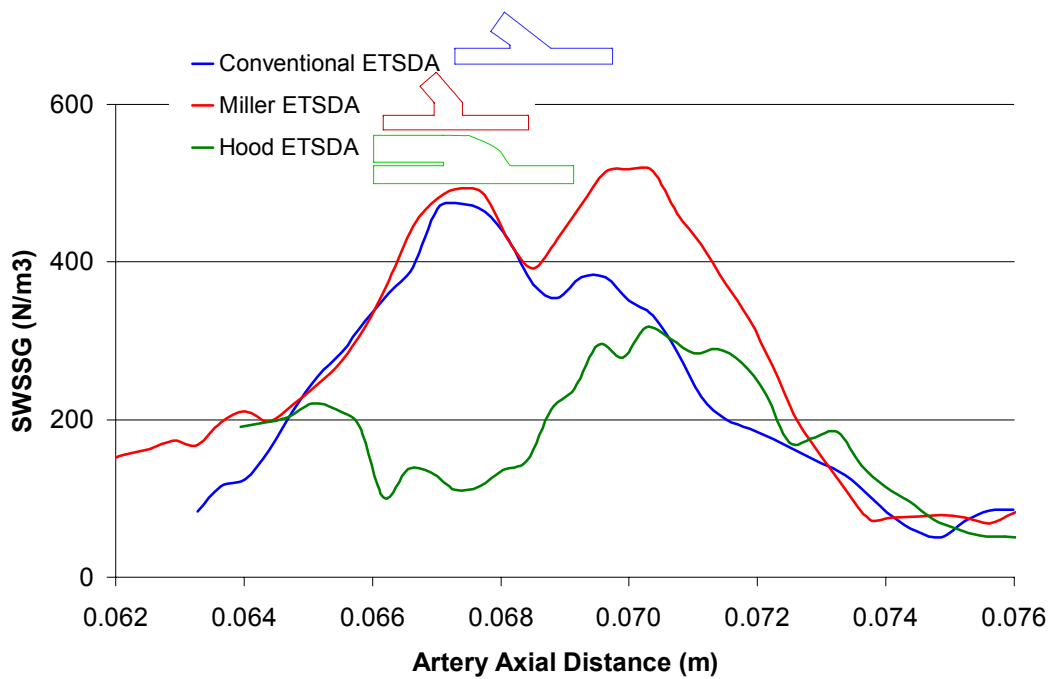
Figure 5.25: Floor time-average SWSSG resulting from the hemodynamics in the optimal shapes of the conventional, Miller cuff, and hood ETSDA models.

139
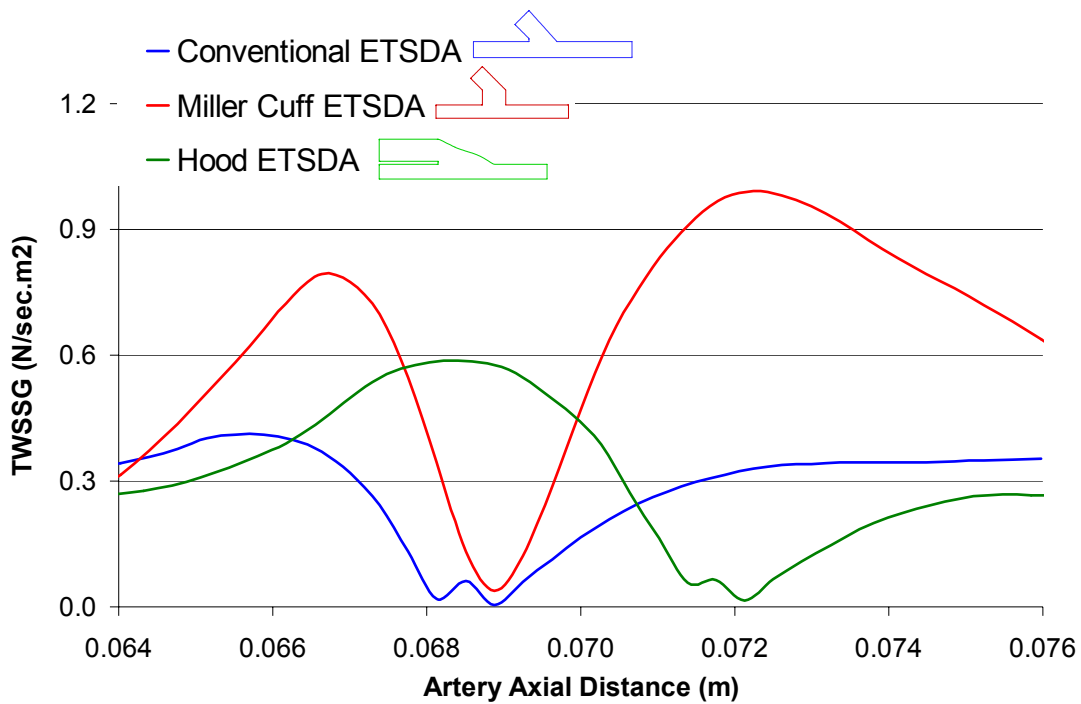
Figure 5.26: Floor time-average TWSSG resulting from the hemodynamics in the typical/non-optimal shapes of the conventional, Miller cuff, and hood ETSDA models.

Figure 5.27: Floor time-average TWSSG resulting from the hemodynamics in the optimal shapes of the conventional, Miller cuff, and hood ETSDA models.

140
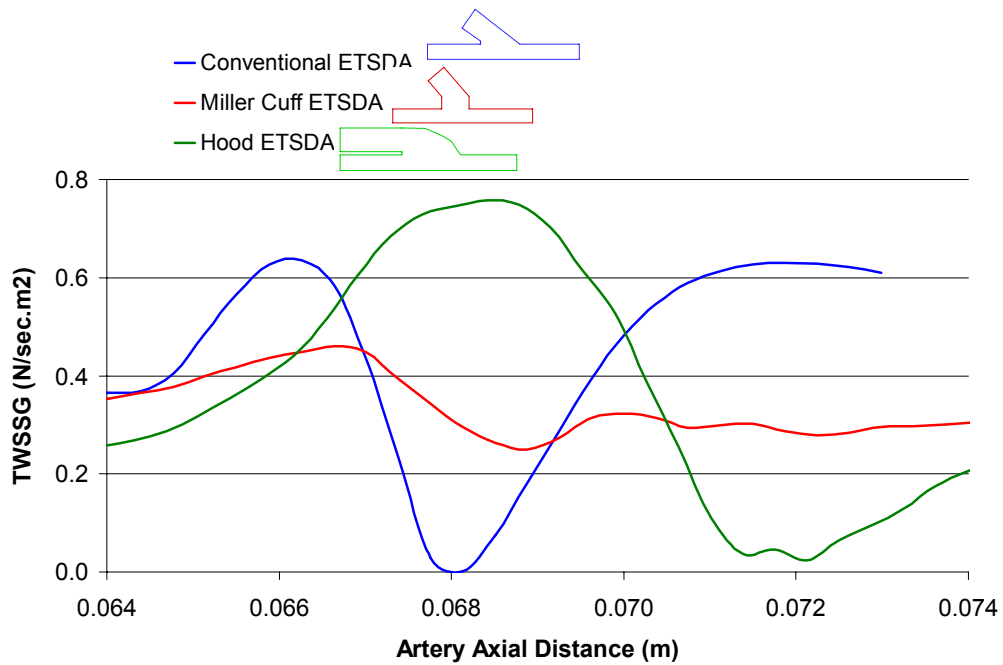
In conclusion, the SOGA results for the various ETSDA models clearly indicate that the graft caliber and the anastomotic are two important factors in the shape optimization based on improving the hemodynamics conditions on the floor of the host artery. In fact, one main reason that the shape optimization of the hood ETSDA model did not lead to meaningful gains is that the graft caliber and the anastomotic angle were kept constant during the optimization process. It suggested to include the cut length as a design parameter by which the hood ETSDA shape optimization becomes significant. The current shape optimization results would have surely be different had the WSS gradients on the suture line region been accounted for as their impact is masked by the compliance mismatch. Besides, note that the present shape optimization is conducted on idealized ETSDA models, hence the SWSSG and TWSSG would be overpredicted by the LCMM at the toe and heel sharp angles; in a real or natural ESTDA model those gradient values will be lower from what they would be predicted by the LCMM solver.

CHAPTER 6: CONCLUSION

A formal shape optimization for peripheral bypass grafts end-to-side distal anastomoses has been established in the current dissertation. Three different ETSDA models were considered for this optimization: the conventional, the Miller cuff, and the hood models. The long-term goal of this particular research effort is to lower morbidity and reduce medical costs for patients suffering from peripheral vascular diseases.

The technicality of the current shape optimization revolves around three computational components. The most important component is the LCMM solver that is capable of delivering accurate fluid dynamics solutions in physical domains in which the solution pre-processing is independent from the geometry. This pre-processing geometry independence is favorably practical to automate the design of the ETSDA models. The other two components involved in the shape optimization approach are an automated pre-processor and a genetic-algorithm-based optimizer. The automated pre-processor task is to distribute solution points in the ETSDA geometries whereas the task of the optimizer is to modify those geometries such that the abnormal hemodynamics patterns on the floor of the ETSDA are minimized.

The results of the research carried out in this dissertation were segregated in two main parts. The first is comprised comprises of stability analyses as well as steady and unsteady flow validation results of the numerical method underlying the LCMM flow solver. The validation results demonstrated a high degree of accuracy for the LCMM solver when dealing with incompressible flows. The second part includes single-objective and bi-objective shape optimization results for the ETSDA models using the LCMM. The optimization results were very significant in the case of conventional and Miller cuff anastomoses. This was not the case for the hood model as the changes in the hood curvature did not seem to impact the WSS gradients on the floor of the host artery; should the suture line cut length be parameterized as an optimization variable, then stronger impact will be witnessed.

It is still early to extend recommendations for vascular surgeons as far as optimizing their bypass procedures since the flow three-dimensionality and the compliance mismatch at the suture line have not been considered in the current optimization. A future extension of the current work should have an optimization target to minimize the host artery floor SWSSG and TWSSG values as well as the suture line principal stresses in 3D geometries that incorporates fluid structure interaction accounting for the interaction between the hemodynamics within the artery and the mechanical response of the arterial wall. For now, the work achieved in this dissertation constitutes a strong foundation and a stepping stone for the next phase of the bypass procedure optimization research.

LIST OF REFERENCES

[1]   American Heart Association. Peripheral Artery Disease Quick Facts. 2005. Dallas, Texas. American Heart Association.

[2]   Taylor LM, Edwards JM, and Porter JM, "Present Status of Reversed Vein Bypass Grafting: Five Year Results of a Modern Series," *Journal of Vascular Surgery*, Vol. 11, pp. 193-206, 1990.

[3]   Veith FJ, Gupta SK, et al., "Six-year Prospective Multicenter Randomized Comparison of Autologous Saphenous Vein and Expanded Polytetrafluoroethylene Grafts in Infrainguinal Arterial Reconstructions," *Journal of Vascular Surgery*, Vol. 3, pp. 104-114, 1986.

[4]   Rafferty TD, Avellon JC, et al., "A Metropolitan Experience with Infrainguinal Revascularization: Operative Risk and Later Results in Northeastern Ohio," *Journal of Vascular Surgery*, Vol. 6, pp. 365-371, 1987.

[5]   Kraiss LW, Clowes AW, "Response of the Arterial Wall to Injury and Intimal Hyperplasia," *The Basic Science of Vascular Disease*, Sidawy AN, Sumpio BE, DePalma RG, Armonk NY (eds.), Futura Publishing Company Inc., pp. 289-317, 1997.

[6]   Bassiouny HS, White S, Glagov S, Choi E, Giddens DP, and Zarins CK, "Anastomotic Intimal Hyperplasia: Mechanical Injury or Flow Induced," *Journal of Vascular Surgery*, Vol. 15, pp. 708-716, 1992.

[7]   Trubel W, Schima H, Czerny M, Perktold K, Schimek MG, and Poltrerauer, "Experimental Comparison of Four Methods of end-to-side Anastomosis with Expanded Polytetrafluoroethylene," *British Journal of Surgery*, Vol. 91, pp. 159-167, 2004.

[8]   Kleinstreuer C, Hyun S, Buchanan JR Jr., Longest PW, Archie JP Jr., and Truskey GA, "Hemodynamics Parameters and Early Intimal Thickening in Branching Blood Vessels," *Critical Reviews in Biomedical Engineering,* Vol. 29, pp. 1-64, 2001.

[9]   Sottiurai VS, "Distal Anastomotic Intimal Hyperplasia: Histocytromorphology, Pathophysiology, Etiology, and Prevention," *International Journal of Angiology*, Vol. 8, pp. 1-10, 1999.

[10]   Liu SQ, "Biomechanical Basis of Vascular Tissue Engineering," *Critical Reviews in Biomedical Engineering,* Vol. 27, pp. 75-148, 1999.

[11]   Logerfo FW, Quist WC, Nowak MD, Crawshaw HM, Hauden-schild CC, "Downstream Anastomotic Hyperplasia: A Mechanism for Failure in Dacron Arterial Grafts," *Annals of Surgery,* Vol. 197, pp. 479-483, 1983.

[12]   Sottiurai VS, Yao JST, et al., "Distal Anastomotic Intimal Hyperplasia: Histopathologic Character and Biogenesis," *Annals of Vascular Surgery*, Vol. 3, pp. 26-33, 1989.

[13]   Fry DL, "Acute Vascular Endothelia Changes Associated with Increased Blood Velocity Gradients," *Circulation Research*, Vol. 22, pp. 165-197, 1968.

[14]   Imparato AM, Baumann FG, and Pearson J, "Electron Microscopic Studies of Experimentally Produced Fibromuscular Arterial Lesions," *Surgery, gynecology & obstetrics,* Vol. 139, pp. 497-504, 1974.

[15]   Keynton RS, Evancho MM, Sims RL, Rodway NV, Gobin A, and Rittgers SE, "Intimal Hyperplasia and Wall Shear in Arterial Bypass Graft Distal Anastomoses: An *In* Vivo Model Study," *Journal of Biomechanical Engineering*, Vol. 123, pp. 464-473, 2001.

[16]   Ojha M, "Spatial and Temporal Variations of Wall Shear Stress within an End-to-side Arterial Anastomosis Model," *Journal of Biomechanics*, Vol. 26, pp. 1377-1388, 1993.

[17]   Lei M, Kleinstreur C, and Archie Jr. JP, "Geometric Design Improvement for Femoral Graft-Artery Junctions Mitigating Restenosis," *Journal of Biomechanics*, Vol. 29, pp. 1605-1614, 1996.

[18]   Fisher RK, How TV, Carpenter T, Brennan JA, and Harris PL, "Optimising Miller Cuff Dimensions. The Influence of Geometry on Anastomotic Flow Patterns," *European Journal of Vascular and Endovascular Surgery*, Vol. 21, pp. 251-260, 2001.

[19]   O'Brien T, Walsh M, and McGloughin T, "On Reducing Abnormal Hemodynamics in the Femoral End-to-Side Anastomosis: The Influence of Mechanical Factors," *Annals of Biomedical Engineering,* Vol. 33, pp. 310-322, 2005.

[20]   Rozza G, "Shape Design by Optimal Flow Control and Reduced Basis Techniques: Applications to Bypass Configurations in Haemodynamics," PhD Thesis, École Polytechnique Federal de Lausanne, November 2005.

[21]   Rozza G, "On optimization, control and shape design for an arterial bypass," *International Journal for Numerical Methods in Fluids*, Bill Morton Prize Paper, Vol. 47, pp. 1411-1419, 2005.

[22]   Taylor RS, Loh A, McFarland RJ, and Cox M, Chester JF, "Improved Technique for Polytetrafluoroethylene Bypass Grafting: Long-term Results Using Anastomotic Vein Patches," *British Journal of Surgery*, Vol. 79, pp. 348-354, 1995.

[23]   Divo E and Kassab AJ, "An Efficient Localized RBF Meshless Method for Fluid Flow and Conjugate Heat Transfer," *ASME Journal of Heat Transfer,* Vol. 129, pp. 124-136, 2007.

[24]   El Zahab Z, Divo E, Kassab AJ, and Mitteff E, "Two-dimensional Meshless Numerical Modeling of the Blood Flow within Arterial End-to-side Distal Anastomoses", in *ASME International Mechanical Engineering Congress and RD & D Expo*, Chicago, IL, USA, 2006.

[25]   Divo E. and Kassab A., "Localized Meshless Modeling of Natural Convective Viscous Flows," *Numerical Heat Transfer, Part B: Fundamentals*, *in print.*

[26]   Raptis M, and Miller JH, "Influence of a Vein Cuff on Polytetrafluoroethylene Grafts for Primary Femoropopliteal Bypass," *British Journal of Surgery*, Vol. 82, pp. 487-491, 1995.

[27]   Lemson MS, Tordoir JHM, Daemen MJAP, and Kitslaar PJEHM, "Intimal Hyperplasia in Vascular Grafts," *European Journal of Vascular and Endovascular Surgery*, Vol. 19, pp. 336-350, 2000.

[28]   Zarins CK, Zatina MA, Giddens DP, Ku DN, and Glagov S, "Shear Stress Regulation of Artery Lumen Diameter in Experimental Atherogenesis," *Journal of Vascular Surgery*, Vol. 5, pp. 413-420, 1987.

[29]   Kohler TR, Kirkman TR, Kraiss LW, Zierler BK, and Clowes AW, "Increased Blood Flow Inhibits Neointimlal Hyperplasia in Endothelialized Vascular Grafts," *Circulation Research*, Vol. 69, pp. 1557-1565, 1991.

[30]   Ku DN, Giddens DP, Zarins CK, and Glagov S, "Pulsatile Flow and Atherosclerosis in the Human Carotid Bifurcation: Positive Correlation between Plaque Location and Low and Oscillating Shear Stress," *Arteriosclerosis*, Vol. 5, 293-302, 1985.

[31] Li X and Rittgers, "Hemodynamic Factors at the Distal End-to-Side Anastomosis of a Bypass Graft With Different POS:DOS Flow Ratios," *Journal of Biomechanical Engineering*, Vol. 123, pp. 270-276, 2001.

[32]   Hofer M, Rappitsch G, Perktold K, Trubel W, and Schima H, "Numerical Study of Wall Mechanics and Fluid Dynamics in End-to-side Anastomoses and Correlation to Intimal Hyperplasia," *Journal of Biomechanics*, Vol. 29, pp. 1297-1308, 1996.

[33]   Leuprecht A, Perktold K, Prosi M, Berk T, Trubel W, and Schima H, "Numerical Study of Hemodynamics and Wall Mechanics in Distal End-to-side Anastomoses of Bypass Grafts," *Journal of Biomechanics*, Vol. 35, pp. 225–236, 2002.

[34]   Mondy JS, Linder V, Miyashiro JK, Berk BC, Dean RH, and Geary RL, "Platelet Growth Factor and Receptor Expression in Response to Altered Blood Flow In Vivo," *Circulation Research*, Vol. 81, pp. 320-327, 1997.

[35]   Loth F, Jones SA, Zarins CK, Giddens DP, Nassar RF, Seymour G and Bassiouny HS, "Relative Contribution of Wall Shear Stress and Injury in Experimental Intimal Thickening at PTFE End-to-Side Arterial Anastomoses," *Journal of Biomechanical Engineering*, Vol. 124, pp. 44-51, 2002.

[36]   DePaola N, Gimbrone Jr. MA, Davies PF, and Dewey Jr. CF, "Vascular Endothelium Responds to Fluid Shear Stress Gradients," *Arteriosclerosis, Thrombosis, and Vascular Biology*, Vol. 12, pp. 1254-1257, 1992.

[37]   Trady Y, Resnick N, Nagel T, Gimbrone Jr. MA, and Dewey Jr. CF, "Shear Stress Gradients Remodel Endothelial Monolayers in Vitro via a Cell Proliferation-Migration-Loss Cycle," *Arteriosclerosis, Thrombosis, and Vascular Biology*, Vol. 17, pp. 3102-3106, 1997.

[38]   Hsu PP, Song L, Li Y, Usami S, Ratcliffe A, Wang X, and Chien S, "Effects of Flow Patterns on Endothelial Cells Migration into a Zone of Mechanical Denudation," *Biochemical and Biophysical Research Communications*, Vol. 285, pp. 751-759, 2001.

[39]   Wells D, Archie JP, Kleinstreuer C, "The effect of Carotid Artery Geometry on the Magnitude and Distribution of Wall Shear Stress Gradients," *Journal of Vascular Surgery*, Vol. 23, pp. 667-678, 1996.

[40]   White CR, Heidekker M, Bao X, and Frangos JA, "Temporal Gradients in Shear, but Not Spatial Gradients, Stimulates Endothelial Cell Proliferation," *Circulation*, Vol. 103, pp. 2508-2513, 2001.

[41]   Leask RL, Butany J, Johnston KW, Ross Ethier C, and Ojha M, "Human Saphenous Vein Coronary Artery Bypass Graft Morphology, Geometry and Hemodynamics," *Annals of Biomedical Engineering*, Vol. 33, pp. 301-309, 2005.

[42]   Steinman DA, Vinh B, Ross Ethier C, Ojha M, Cobbod RSC, and Johnston, KW, "A Numerical Simulation of Flow in a Two-Dimensional End-to-Side Anastomosis Model," *Journal of Biomechanical Engineering*, Vol. 115, pp. 112-118, 1993.

[43]   Sumpio BE, Banes AJ, Levin LG, Johnson G, "Mechanical Stress Stimulates Aortic Endothelial Cells to Proliferate," *Journal of Vascular Surgery*, Vol. 6, pp. 252-256, 1987.

[44]   Ojha M, "Wall Shear Stress Temporal Gradient and Anastomotic Intimal Hyperplasia," *Circulation Research*, Vol. 74, pp. 1227-1231, 1994.

[45]   Lei M, Giddens DP, Jones SA, Loth F, and Bassiouny HS, "Pulsatile flow in an end-to-side vascular graft model: comparison of computations with experimental data", *Journal of Biomechanical Engineering*, Vol. 123, pp. 80-87, 2001.

[46]   Ojha M, and Cobbold RSC, "Influence of Angle on Wall Shear Stress Distribution for an End-to-Side Anastomosis," *Journal of Vascular Surgery*, Vol. 19, pp. 1067-1073, 1994.

[47]   Fei D, Thomas JD, and Rittgers SE, "The Effect of Angle and Flow Rate Upon Hemodynamics in Distal Vascular Graft Anastomoses: A Numerical Model Study," *Journal of Biomechanical Engineering*, Vol. 116, pp. 331-336, 1994.

[48]   Wijesinsghe LD, Mahmood T, Scott DJA, "Axial Flow Fields in Cuffed End-to-side Anastomoses: Effect of Angle and Disease Progression," *European Journal of Vascular and Endovascular Surgery*, Vol. 18, pp. 240-244, 1999.

[49]   Noori N, Scherer R, Perktold K, Czemy M, Kamer G, Trubel W, Polterrauer P, and Schima H, "Blood Flow in Distal End-to-side Anastomoses with PTFE and Venous Patch: Results of an *in vitro* Flow Visualization Study," *European Journal of Vascular and Endovascular Surgery*, Vol. 18, pp. 191-200, 1999.

[50]   Lei M, Archie Jr. JP, and Kleinstreur C, "Computational Design of a Bypass Graft That Minimizes Wall Shear Stress Gradients in the Region of the Distal Anastomosis," *Journal of Vascular Surgery*, Vol. 19, pp. 637-646, 1997.

[51]   Cole JS, Watterson JK, and O'Reilly MJG,"Numerical Investigation of the Hemodynamics at a Patched Arterial Bypass Anastomosis," *Medical Engineering and Physics*, Vol. 24, pp. 393-401, 2002.

[52]   Walsh MT, Kavanagh EG, O'Brien T, Grace PA, and McGloughin T, "On the Existence of an Optimum End-to-Side Junctional Geometry in Peripheral Bypass Surgery - A Computer Generated Study," *European Journal of Vascular and Endovascular Surgery*, Vol. 26, pp. 649-656, 2003.

[53]   Noori N, Scherer R, Perktold K, Czemy M, Kamer G, Trubel W, Polterrauer P, and Schima H, "Blood Flow in Distal End-to-side Anastomoses with PTFE and Venous Patch: Results of an *in vitro* Flow Visualization Study," *European Journal of Vascular and Endovascular Surgery*, Vol. 18, pp. 191-200, 1999.

[54]   Belytscho T, Lu YY, and Gu L, "Element-free Galerkin methods," *International Journal of Numerical Methods in Engineering,* Vol. 37, pp. 229-256, 1994.

[55]   Yagawa G and Furukawa T, "Recent Developments of Free Mesh Method," *International Journal of Numerical Methods in Engineering,* Vol. 47, pp. 1419-1443, 2000.

[56]   Divo E, Kassab AJ, Mitteff E, and Quintana L "A Parallel Domain Decomposition Technique for Meshless Methods Applications to Large-Scale Heat Transfer Problems," ASME Paper: HT-FED2004-56004. *Proceedings of the 2004 ASME Heat Transfer/Fluids Engineering Summer Conference*. July 11–15, 2004. Charlotte, North Carolina, USA.

[57]   Divo E, Kassab AJ, and El Zahab Z, "Parallel Domain Decomposition Meshless Modeling of Dilute Convection-Diffusion of Species," *Proceedings of BEM27/MRM* Kassab AJ, ,Brebbia CA and Divo EA (eds.), Computational Mechanics Publications, Southampton, U.K., 2005.

[58]   Divo E and Kassab AJ, "Iterative Domain Decomposition Meshless Method Modeling of Incompressible Flows and Conjugate Heat Transfer," *Engineering Analysis with Boundary Elements*, Vol. 30, pp. 465-478, 2006.

[59]   Chung KC, "A Generalized Finite Difference Method for Heat Transfer Problems of Irregular Geometries," *Numerical Heat Transfer*, Vol. 4, pp. 345–357, 1981.

[60]   Sridar D and Balakrishnan N, "An Upwind Finite Difference Scheme for Meshless Solvers," *Journal of Computational Physics*, Vol. 189, pp. 1–29, 2003.

[61]   Chew CS, Yeo KS, and Shu C, "A generalized Finite-difference (GFD) ALE Scheme for Incompressible Flows around Moving Solid Bodies on Hybrid Meshfree–Cartesian Grids," *Journal of Computational Physics*, Vol. 218, pp. 510–548, 2006.

[62]   Luo H, Baum JD, and Lohner R, "A Hybrid Cartesian Grid and Gridless Method for Compressible Flows," *43rd AIAA Aerospace Sciences Meeting and Exhibit*, 10-13, January 2005, Reno, Nevada.

[63]   Onate E and Idelshon S, "Meshless Analysis of Incompressible Flows Using the Finite Point Method," *Innovative Tools for Scientific Computation in Aeronautical Engineering*, Perjaux J, Joly P, Pironneau O, and Onate (Eds.), CIMNE, Barcelona, 2002.

[64]   Zhang XK, Kwon K, and Youn S, "The Least-squares Meshfree Method for the Steady Incompressible Viscous Flow," *Journal of Computational Physics*, Vol. 206, pp. 182–207, 2005.

[65]   Lin H and Atluri SN, "The Meshless Local Petrov-Galerkin (MLPG) Method for Solving Incompressible Navier-Stokes Equations," *Computer Modeling in Engineering and Sciences*, Vol. 2, pp. 117-142, 2001.

[66]   Fries T and Matthies H, "A Stabilized and Coupled Meshfree/Meshbased Method for the Incompressible Navier-Stokes Equations — Part I: Stabilization," Report, Department of Mathematics and Computer Science, Technical University Braunschweig, Brunswick, Germany, February, 2005.

[67]   Kirshman DJ and Liu F, "A Gridless Boundary Condition Method for the Solution of the Euler Equations on Embedded Cartesian Meshes with Multigrid," *Journal of Computational Physics*, Vol. 201, pp. 119–147, 2004.

[68]   Koh EPC, Tsai HM, and Liu F, "Euler Solution Using Cartesian Grid with a Gridless Least-Squares Boundary Treatment," *AIAA Journal*, Vol. 43, pp. 246-255, 2005.

[69] Kansa EJ, "Multiquadrics- a Scattered Data Approximation Scheme with Applications to Computational Fluid Dynamics I- Surface Approximations and Partial Derivative Estimates," *Computer and Mathematics with Applications,* Vol. 19*,* pp. 127-145, 1990.

[70] Kansa EJ, "Multiquadrics- a Scattered Data Approximation Scheme with Applications to Computational Fluid Dynamics II - Solutions to Parabolic, Hyperbolic and Elliptic Partial Differential Equations," *Computer and Mathematics with Applications*, 19*,* pp. 147-161, 1990.

[71]   Kansa EJ and Hon YC, "Circumventing the Ill-Conditioning Problem with Multiquadric Radial Basis Functions: Applications to Elliptic Partial Differential Equations," *Computer and Mathematics with Applications,* Vol. 39*,* pp. 123-137, 2000.

[72]   Buhmann, M.D., *Radial Basis Functions: Theory and Implementation*, Cambridge University Press, Cambridge, 2003.

[73]   Cheng, A.H.-D., Golberg, M.A., Kansa, E.J., Zammito, G., Exponential Convergence and H-c Multiquadric Collocation Method for Partial Differential Equations, *Numerical Methods in P.D.E.*, vol. 19, no. 5, pp. 571-594, 2003.

[74]   Sarler B, Perko J, and Chen CS, "Radial Basis Function Collocation Method Solution of Natural Convection in Porous Media", *International Journal of Numerical Methods for Heat & Fluid Flow*, Vol. 14, pp. 187-212, 2004.

[75]   Divo E and Kassab AJ, "Efficient Localized Meshless Modeling of Natural Convective Viscous Flows," *AIAA Paper AIAA-2006-3089*.

[76]   Chen HQ and Shu C, "An Efficient Implicit Mesh-free Method to Solve Two-dimensional Compressible Euler Equations," *International Journal of Modern Physics C*, Vol. 16, pp. 439–454, 2005.

[77]   Mitteff, E. A., Divo, E. A., and Kassab, A. J., 2006, "Automated Point Distribution and Parallel Segmentation for Meshless Methods," *Proceedings of CIMENICS 2006, 8th International Congress of Numerical Methods in Engineering and Applied Sciences.* held on Margarita Island, Venezuela, March 20-24, 2006, Gamez B., Ojeda D., Larrazabal G., and Cerrolaza M. (eds.), Sociedad Venezuelana de Methodos Numericos En Engineria, Valencia, Venezuela, pp. 93-100.

[78]   Tannehill JC, Anderson DA, and Pletcher RH, 1997, *Computational Fluid Mechanics and Heat Transfer*, Taylor & Francis, Washington, DC, USA.

[79]   Godunov SK, "A Difference Scheme for Numerical Solution of Discontinuous Solution of Hydrodynamic Equations," *Math. Sbornik*, Vol. 47, pp. 271-306, 1959.

[80]   Leonard BP, "A Stable and Accurate Convective Modelling Procedure Based on Quadratic Interpolation," *Computer Methods in Applied Mechanics and Engineering*, Vol. 19, pp. 59-98, 1979.

[81]   Borris JP and Book DL, "Flux-corrected Transport II: Generalizations of the Method," *Journal of Computational Physics*, Vol.18, pp. 248, 1975.

[82]   Harten A, "High Resolution Schemes for Hyperbolic Conservation Laws," *Journal of Computational Physics*, Vol. 49, pp. 357-393, 1983.

[83]   Van Leer B, "Towards the Ultimate Conservative Difference Scheme. V. A Second Order Sequel to Godunov's Method," *Journal of Computational Physics,* Vol. 32, pp. 101-136, 1979.

[84]   Chakravarthy SR, Osher S, "High Resolution Applications of the OSHER Upwind Scheme for the Euler Equations," *AIAA Paper 83-1943*, 1983.

[85]   Roe PL, "Some Contributions to the Modelling of Discontinuous Flows', *Lectures in Applied Mathematics*, Vol. 22, pp. 163-193, 1985.

[86]   Gaskell PH and Lau AKC, "Curvature Compensated Convective Transport: SMART, a New Boundedness Preserving Transport Algorithm," *International Journal of Numerical Methods in Fluids*, Vol. 8, pp. 617-641, 1988.

[87]   Leonard BP, "The ULTIMATE Conservative Difference Scheme Applied to Unsteady One-dimensional Advection," *Computer Methods in Applied Mechanics and Engineering*, Vol. 88, pp. 17-74, 1991.

[88]   Jasak H, Weller HG, Gosman AD, "High Resolution NVD differencing scheme for arbitrary unstructured meshes," *International Journal of Numerical Methods in Fluids*, Vol. 31, pp. 431-449, 1999.

[89]   Chandhini G and Sanyasiraju YVSS, "Local RBF-FD Solutions for Steady Convection–Diffusion Problems," *International Journal of Numerical Methods in Engineering,* Vol. 72*,* pp. 352–378, 2007.

[90]   Gu YT and Liu GR, "Meshless Techniques for Convection Dominated Problems," *Computational Mechanics*, Vol. 38, pp. 171–182, 2006.

[91]   Harlow FH and Welch JE, "Numerical Calculation of Time Dependent Viscous Incompressible Flow of Fluids with a Free Surface," *Physics of Fluids*, Vol. 8, pp. 2182-2189, 1965.

[92]   Patankar SV, *Numerical Heat Transfer and Fluid Flow*, Hemisphere Press, 1980.

[93]   Kim D and Choi H, "A Second-Order Time-Accurate Finite Volume Method for Unsteady Incompressible Flow on Hybrid Unstructured Grids," *Journal of Computational Physics*, Vol. 162, pp. 411-428 , 2000.

[94]   Zhang Y, Street RL, and Koseff JR, "A Non-Staggered Grid, Fractional Step Method for Time-Dependent Incompressible Navier-Stokes Equations in Curvilinear Coordinates," *Journal of Computational Physics*, Vol. 114, pp. 18-33 , 1994.

[95]   Longest PW and Kleinstreuer C, "Numerical Simulation of Wall Shear Stress Conditions and Platelet Localization in Realistic End-to-Side Arterial Anastomoses," *Journal of Biomechanical Engineering*, Vol. 125, pp. 671-681, 2003.

[96]   Giordana S, Sherwin SJ, Peiró J, Doorly DJ, Crane JS, Lee KE, Cheshire NJW, Caro CG, "Local and Global Geometric Influence on Steady Flow in Distal Anastomoses of Peripheral Bypass Grafts," *Journal of Biomechanical Engineering*, Vol. 127, pp. 1087-1098, 2005.

[97]   Barnes HA, "The yield stress—a review or '$\pi\alpha\nu\tau\alpha$ $\rho\epsilon\iota$'—everything flows?," *Journal of Non-Newtonian Fluid Mechanics*, Vol. 81, pp. 133–178, 1999.

[98]   Wetzel ED and Wagner NJ, "Protective Fabrics Utilizing Shear Protective Fabrics Utilizing Shear Thickening Fluids Shear Thickening Fluids (STFs)," *Industrial Fabrics Association International (IFAI) 4th International Conference on Safety and Protective Fabrics,* Pittsburgh, PA. October 27-29 2004.

[99]   Casson NA. "A flow equation for pigment-oil suspensions of the printing ink type," *Rheology of Disperse Systems,* Mills CC (ed.). Pergamon: Oxford, 1959; pp. 84–102.

[100]   Walburn FJ, Schneck DJ, "A constitutive equation for whole human blood," *Biorheology*, Vol. 13, pp. 201– 210, 1976.

[101]   Quemeda D, "Rheology of Concentrated Disperse Systems III. General Features of the Proposed non-Newtonian Model. Comparison with Experimental Data," *Rheologica Acta*, Vol. 17, pp. 643-653, 1977.

[102]   Buchanan Jr. J, Kleinstreuer C, and Comer J, "Rheological effects on pulsatile hemodynamics in a stenosed tube," *Computers & Fluids*, Vol. 29, pp. 695-724, 2000.

[103]   Neofytou P and Tsangaris S, "Effects of Blood Models on Flows through a Stenosis," *International Journal of Numerical Methods in Fluids*, Vol. 43, pp. 597–635, 2003.

[104]   Jung H, Choi JW, and Park CG, "Asymmetric Flows of Non-Newtonian Fluids in Symmetric Stenosed Artery," *Korea-Australia Rheology Journal*, Vol. 16, pp. 101-108, 2004.

[105]   Merill EW, "The Rheology of Blood," *Physiology Review*, Vol. 26, pp. 863-888, 1969.

[106]   Goldberg DE, *Genetic Algorithms in Search, Optimization, and Machine Learning*, Addison-Wesley Professional, Boston, MA, 1989.

[107]   Haupt RL, and Haupt SE, *Practical Genetic Algorithms*, 2nd ed., John Wiley, Hoboken, N.J., 2004.

[108]   Divo E, and Kassab AJ, "An Efficient Singular Superposition Technique for Cavity Detection and Shape Optimization," *Numerical Heat Transfer*, Part B: Fundamentals, Vol. 45, pp. 1-30, 2004.

[109]   Coello Coello CA, "Recent Trends in Evolutionary Multiobjective Optimization," *Evolutionary Multiobjective Optimization*, Abraham A, Jain L, and Goldberg R (eds.), Springer, pp. 7-32, 2004.

[110]   Gerace SA, Divo EA, and Kassab AJ, "An Automated Approach to Multiobjective Shape Optimization for Engineering Design Problems," in *Inverse Problems, Design and Optimization Symposium (IPDO-2007)*, Miami, Florida, USA, 2007.

[111]   Hilbert, R., Janiga, G., Baron, R., The´venin, D., "Multi-objective Shape Optimization of a Heat Exchanger Using Parallel Genetic Algorithms," *International Journal of Heat and Mass Transfer,* Vol. 49, pp. 2567–2577, 2006.

[112] Marco N, Elsie J, and Lanteri S, "Multi-Objective Optimization in CFD by Genetic Algorithms," Rapport de Recherche N° 3686, Institut National de Recherche en Informatique et en Automatic, Sophia Antipolis Cedex (France), April, 1999.

[113] Divo E, Kassab AJ, and Ingber MS, "Shape Optimization of Acoustic Scattering Bodies," *Engineering Analysis with Boundary Elements*, Vol. 27, pp. 695-704, 2003.

[114] Annicchaiarico W and Cerrolaza M, "An Evolutionary Approach for the Shape Optimization of General Boundary Elements Models," *Electronic Journal of Boundary Elements*, Vol. BETEQ 2001, No. 2, pp. 251-266, 2002.

[115] Hamalainen JP, Makinen RAE, Tarvainen P, and Toivanen J, "Evolutionary Shape Optimization in CFD with Industrial Applications," in *European Congress on Computational Methods in Applied Sciences and Engineering (ECCOMAS 2000)*, Barcelona, Spain, 2000.

[116] Díaz Casás V, Lopez Peña F, and Duro RJ, "Automatic Design and Optimization of Wind Turbine Blades," in *International Conference on Computational Intelligence for Modelling Control and Automation,and International Conference on Intelligent Agents,Web Technologies and Internet Commerce (CIMCA-IAWTIC'06)*, Sydney, Australia, 2006.

[117] Ballyk PD, Walsh C, Butany J, and Ojha M, "Compliance Mismatch May Promote Graft-Artery Intimal Hyperplasia by Altering Suture-Line Stresses," *Journal of Biomechanics*, Vol. 31, pp. 229-237, 1998.

[118] Qiao A and Liu Y, "Influence of graft-host diameter ratio on the hemodynamics of CABG," *Bio-Medical Materials and Engineering,* Vol. 16, pp. 189-201, 2006.

[119] Abbott WM, Green RM, Matsumato T, Wheeler JR, Miller N, Veith FJ et al., "Prosthetic above-knee femoropopliteal bypass grafting: results of a multi-center randomized prospective trial," *Journal of Vascular Surgery*, Vol. 25, 19–28, 1997.